Theoretical and Experimental Study of Microstrip Discontinuities in Millimeter Wave Integrated Circuits

Final Report

Submitted to National Science Foundation

by

Linda P.B. Katehi

Radiation Laboratory
The University of Michigan
Ann Arbor, MI 48109

July 1990

engn

UMR0386

Contents

1 FINAL REPORT

1. **NSF Proposal Number:** ECS-8602530

2. **Period Covered by the Report:** August 1, 1988 - July 31, 1990

3. **Title of Proposal:**
   Theoretical and Experimental Study of Microstrip Discontinuities in Millimeter Wave Integrated Circuits.

4. **Contract Number:** ECS-8602530

5. **Name of Institution:** The University of Michigan

6. **Authors of the Report:** Linda P.B. Katehi

7. **List of Interim Reports and Manuscripts Submitted or Published Under Full or Partial NSF Sponsorship During this Reporting Period:**

   - T.G. Livernois and P.B. Katehi, "A Generalized Method for Deriving the Space-Domain Green's Function in a Shielded, Multilayer Substrate Structure with Applications to MIS Slow-Wave Transmission Lines," *IEEE Transactions on Microwave Theory and Techniques*, vol.37, Nov. 1989, pp. 1761-1767.
   - W.P. Harokopus and P.B. Katehi, "Characterization of Microstrip Discontinuities on Multilayer Dielectric Substrates Including Radiation Losses," *IEEE Transactions on Microwave Theory and Techniques*, vol.37, Dec. 1989, pp. 2058-2066.
   - W.P. Harokopus, P.B. Katehi, W. Ali-Ahmad and G.M. Rebeiz, "Surface Wave Excitation from Open Microstrip Discontinuities," submitted for publication to *IEEE Transactions on Microwave Theory and Techniques.*
   - W.P. Harokopus and P.B. Katehi, "Radiation Losses in Microstrip Antenna Feed Networks Printed on Multilayer Substrates," submitted for publication in the *International Journal of Numerical Modelling.*
   - T.G. Livernois and P.B. Katehi, "Characteristic Impedance and EM Field Distribution in MIS Microstrip", in press, *IEEE Transactions on Microwave Theory and Techniques.*

- T.G. Livernois and P.B. Katehi, "A Simple Method for Characterizing Planar Transmission Line Discontinuities on Dissipative Substrates", submitted for publication in the *IEEE Transactions on Microwave Theory and Techniques.*
- W. P. Harokopus and P. B. Katehi, "An Accurate Characterization of Open Microstrip Discontinuities Including Radiation Losses ". *Proceedings of the International IEEE MTT-S* meeting in Long Beach, CA, June 1989.
- W. P. Harokopus and P. B. Katehi, "Radiation Properties of Open Microstrip Discontinuities". *Proceedings of the International IEEE AP-S* meeting in San Jose, CA, June 1989, pp.1703-1706.
- T. G. Livernois and P. B. Katehi, "Analysis and Design of Slow-Wave Structures Using an Integral Equation Approach ". *Proceedings of the International IEEE MTT-S* meeting in Long Beach, CA, 1989.

8. Scientific Personnel Supported by this Project:

- *Faculty:* Linda P.B. Katehi
- *Graduate Students:* W.P. Harokopus T.G. Livernois

2 RESEARCH TASKS

Title	Personnel Involved with the Research
Theoretical Characterization of Open Microstrip Discontinuities	Linda P.B. Katehi William P. Harokopus
Surface Wave Radiation from Open Microstrip Discontinuities	Linda P.B. Katehi William P. Harokopus
Characterization of MIS Lines	Linda P.B. Katehi Thomas P. Livernois

3 BRIEF DESCRIPTION OF EACH TASK

3.1 Theoretical Characterization of Open Microstrip Discontinuities

Faculty Supervisor: Linda P.B. Katehi

Graduate Student Participant: William P. Harokopus

Work Performed:

During the reported period, the problem of accurate characterization of microstrip discontinuities on multilayer substrates was addressed and the effects of the dielectric structure on the circuit performance were studied. Various types of planar discontinuities were analyzed by using a full-wave method which was based on the solution of the integral equation for the unknown current density on the conductors. The dyadic Green's function for the grounded multi-dielectric substrate was employed to develop an algorithm capable of analyzing structures with an arbitrary number of layers. Included in the solution were both transverse and longitudinal current components, allowing the treatment of a wide class of irregular microstrip elements including steps of width, corners, meander lines, and T-junctions. The unknown current distribution on the microstrip conductors was expended by using rooftop basis functions. In this manner, the current distribution was evaluated and transmission line theory was employed to determine the network parameters.

Numerical results from this technique have demonstrated excellent agreement with measurements and the spectral-domain technique in the case of single dielectric layers. The implemented method fully accounts for coupling, space, and surface wave radiation an d for all dispersive effects.

Details of this work are presented in the publications listed below.

Publications:

1. W.P. Harokopus and P.B. Katehi, "Characterization of Microstrip Discontinuities on Multilayer Dielectric Substrates Including Radiation Losses," *IEEE Transactions on Microwave Theory and Techniques*, vol.37, Dec. 1989, pp. 2058-2066, **Appendix B.**

2. W.P. Harokopus and P.B. Katehi, "Radiation Losses in Microstrip Antenna Feed Networks Printed on Multilayer Substrates," submitted for publication

in the *International Journal of Numerical Modelling*, **Appendix D.**

3. W. P. Harokopus and P. B. Katehi, "An Accurate Characterization of Open Microstrip Discontinuities Including Radiation Losses ". *Proceedings of the International IEEE MTT-S* meeting in Long Beach, CA, June 1989, **Appendix G.**

3.2 Surface Wave Radiation from Open Microstrip Discontinuities

Faculty Supervisor: Linda P.B. Katehi

Graduate Student Participant: William P. Harokopus

Work Performed:

In the previous task, open microstrip discontinuities were analyzed with the method of moments. Circuit elements were characterized by their network parameters which included total radiation loss. No effort was made to separate this loss into the individual contributions of space and surface waves. Space waves refer to the modes radiated into the semi-infinite region above the dielectric, and surface waves are modes bound in the substrate, which forms a grounded dielectric waveguide.

Under this task, a more extensive study of the types and quantity of radiation has been performed. The derived results provide guidelines for the development of low-loss microstrip elements. For example, it is well known that the shape of discontinuities can be altered to improve circuit performance (mitered bend and radial stub). However, finding the influence of these and other similar modifications on the radiation loss is also important. The analysis we have performed has provided the necessary quantitative results for determining when and why a specific circuit modification decreases radiation loss.

The analysis presented in the publications listed below, quantifies the radiation occuring from various mechanisms, and shows the directions of propagation of surface wave radiation. These far-field patterns are useful for determining where coupling through surface wave excitation may be strong. In addition, derived results have demonstrated the strong influence that substrate composition has on radiation properties.

In this task, the far-field patterns were obtained by the complex transformation of the space domain Green's function to the steepest descent plane, where a saddle point integration was performed. The contribution from the saddle point represented the far-field spherical wave power in the half-space above the dielectric. In addition, the residues from the poles captured in the contour deformation represented cylindrical surface waves guided in the dielectric. Theoretical and experimental results were derived for microstrip stubs and bends that revealed the

effect of radiation on circuit performance, quantified the types of radiation and showed the direction and intensity of surface wave propagation in the substrate.

Publications:

1. W.P. Harokopus, P.B. Katehi, W. Ali-Ahmad and G.M. Rebeiz, "Surface Wave Excitation from Open Microstrip Discontinuities," submitted for publication to *IEEE Transactions on Microwave Theory and Techniques*, **Appendix C.**
2. W. P. Harokopus and P. B. Katehi, "Radiation Properties of Open Microstrip Discontinuities". *Proceedings of the International IEEE AP-S* meeting in San Jose, CA, June 1989, pp.1703-1706, **Appendix H.**

3.3 Characterization of MIS Lines

Faculty Supervisor: Linda P.B. Katehi

Graduate Student Participant: Thomas P. Livernois

Work Performed:

MIS slow-wave structures have been studied by several researchers and have been used widely in related MIC's. The slowing effect can be applied to many devices, among them delay lines, phased shifters, and tunable filters. Both single and coupled line geometries have been analyzed using full-wave techniques. The two rigorous methods which have been applied to these structures in the past, namely spectral-domain analysis and finite element method, are cumbersome to work with. The spectral approach requires the use of current basis functions which have well behaved Fourier transforms, and the finite element method sometimes yields spurious modes results which are difficult ot interpret.

Under this task, we have developed a technique which suffers from neither of the above drawbacks. The Green's function for an inhomogeneously filled rectangular waveguide derived using this theory, was used to find dispersion characteristics for various slow wave transmission lines. Furthermore, the characteristic impedance for the MIS microstrip was calculated and the transverse field distributions for various structural parameters were derived to illustrate the three distinct modes of operation for MIS transmission Lines.

Finally, an open-end discontinuity on a highly doped GaAs substrate was characterize in order to understand the effect of the doping density of the circuits performance.

Publications:

1. T.G. Livernois and P.B. Katehi, "A Generalized Method for Deriving the Space-Domain Green's Function in a Shielded, Multilayer Substrate Structure with Applications to MIS Slow-Wave Transmission Lines," *IEEE Transactions on Microwave Theory and Techniques*, vol.37, Nov. 1989, pp. 1761-1767, **Appendix A**.

2. T.G. Livernois and P.B. Katehi, "Characteristic Impedance and EM Field Distribution in MIS Microstrip", in press, *IEEE Transactions on Microwave Theory and Techniques*, **Appendix E.**

3. T.G. Livernois and P.B. Katehi, "A Simple Method for Characterizing Planar Transmission Line Discontinuities on Dissipative Substrates", submitted for publication in the *IEEE Transactions on Microwave Theory and Techniques*, **Appendix F.**

4. T. G. Livernois and P. B. Katehi, "Analysis and Design of Slow-Wave Structures Using an Integral Equation Approach". *Proceedings of the International IEEE MTT-S* meeting in Long Beach, CA, 1989, **Appendix I.**

4 LIST OF APPENDINCES

- **Appendix A**
  A Generalized Method for Deriving the Space-Domain Green's Function in a Shielded, Multilayer Substrate Structure with Applications to MIS Slow-Wave Transmission Lines
  T.G. Livernois and P.B. Katehi

- **Appendix B**
  Characterization of Microstrip Discontinuities on Multilayer Dielectric Substrates Including Radiation Losses
  W.P. Harokopus and P.B. Katehi

- **Appendix C**
  Surface Wave Excitation from Open Microstrip Discontinuities
  W.P. Harokopus, P.B. Katehi, W. Ali-Ahmad and G.M. Rebeiz

- **Appendix D**
  Radiation Losses in Microstrip Antenna Feed Networks Printed on Multilayer Substrates
  W.P. Harokopus and P.B. Katehi

- **Appendix E**
  Characteristic Impedance and EM Field Distribution in MIS Microstrip
  T.G. Livernois and P.B. Katehi.

- **Appendix F**
  A Simple Method for Characterizing Planar Transmission Line Discontinuities on Dissipative Substrates
  T.G. Livernois and P.B. Katehi

- **Appendix G**
  An Accurate Characterization of Open Microstrip Discontinuities Including Radiation Losses
  W. P. Harokopus and P. B. Katehi

- **Appendix H**

Radiation Properties of Open Microstrip Discontinuities
W. P. Harokopus and P. B. Katehi

- **Appendix I**
  Analysis and Design of Slow-Wave Structures Using an Integral Equation Approach
  T. G. Livernois and P. B. Katehi

APPENDIX A

A Generalized Method for Deriving the Space-Domain Green's Function in a Shielded, Multilayer Substrate Structure with Applications to MIS Slow-Wave Transmission Lines

T.G. Livernois and P.B. Katehi

A Generalized Method for Deriving the Space-Domain Green's Function in a Shielded, Multilayer Substrate Structure with Applications to MIS Slow-Wave Transmission Lines

THOMAS G. LIVERNOIS AND PISTI B. KATEHI, MEMBER, IEEE

Abstract—**An efficient technique for deriving the space-domain Green's function due to an arbitrarily oriented current in shielded, multilayer substrate structures is presented. The derived Green's function is then used to find the dispersion characteristics of single and symmetric coupled line MIS slow-wave structures. These results are compared to published theoretical and experimental data to verify the theory presented.**

I. INTRODUCTION

THERE HAS been considerable effort devoted to the design and realization of monolithic microwave integrated circuits (MMIC's) for use in the $f > 20$ GHz region [1]. Once fabricated, monolithic circuits are very difficult to tune for optimum performance and this is a major drawback [1], [2]. Accurate theoretical models of MMIC components are required so that device performance can be predicted confidently, thus avoiding a time-consuming and costly production cycle. Such characterization requires a mathematically rigorous solution for the fields in a particular structure. The use of a Green's function is, therefore, appropriate. Generalized techniques for deriving the spectral-domain or space-domain Green's function for multilayer substrates have been given, but only current densities which are parallel to the layer interfaces are allowed in these approaches [3]–[5]. These techniques find useful application in the analysis of planar integrated circuits and antennas embedded in layered regions. In [6], the Green's function for a rectangular waveguide filled with two dielectrics is given. The inhomogeneous system of equations encountered in [6] increases substantially with the number of layers, thus making the required algebra difficult and time consuming. It is the purpose of this paper to outline a method for deriving the space-domain Green's function for an arbitrarily oriented current in a rectangular waveguide inhomogeneously filled with an arbitrary number of lossy, isotropic dielectric slabs. The approach given here is based on the principle of scattering superposition combined with appropriately chosen magnetic and electric vector potentials. The major advantages of this work are (i) the developed method for evaluating the Green's function can be applied to a current of any orientation and (ii) the solution for unknown-amplitude coefficients always reduces to having to solve 2×2 inhomogeneous sets of equations, regardless of the number of dielectric layers. The scattering parameters of planar stripline discontinuities occurring in shielded, multilayer substrate circuitry may be numerically characterized by following the procedure given in [7] combined with the Green's function obtained here. Research in this direction is proceeding and much remains to be done [7]–[10].

MIS slow-wave structures have been studied by several researchers and are used widely in related MIC's. The slowing effect can be applied to many devices, among them delay lines, phase shifters, and tunable filters. Both single and coupled line geometries have been analyzed using full-wave techniques [11]–[15]. The two rigorous methods which have been applied to these structures in the past, namely spectral-domain analysis and finite element method, can be somewhat cumbersome to work with. The spectral approach requires the use of current basis functions which have well-behaved Fourier transforms, and the finite element method sometimes yields spurious mode results which are difficult to interpret. The present technique, which will be discussed in more detail later, suffers from neither of these drawbacks. The Green's function for an inhomogeneously filled rectangular waveguide derived using the present theory is used to find dispersion characteristics for various slow-wave transmission lines. These results are compared to published theoretical and experi-

Manuscript received February 16, 1989; revised June 26, 1989. This work was supported by the National Science Foundation under Grant ECS-8602530.

The authors are with the Radiation Laboratory, Department of Electrical Engineering and Computer Science, University of Michigan, Ann Arbor, MI 48109-2122.

IEEE Log Number 8930662.

0018-9480/89/1100-1761$01.00 ©1989 IEEE

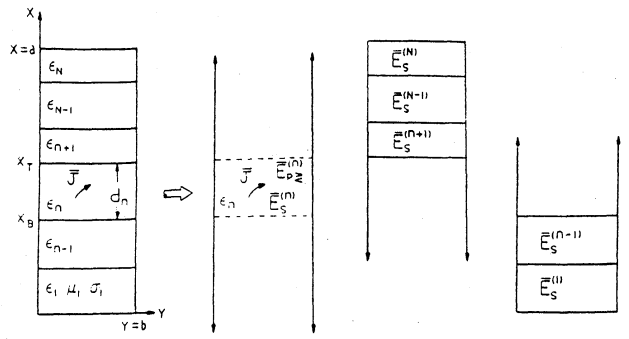

Fig. 1. Representation of inhomogeneously loaded rectangular waveguide as the superposition of parallel-plate structures.

ment results [16] to establish the validity and usefulness of the analytical method given in this paper.

II. Theory

The principle of scattering superposition was first discussed by Tai [17] and recently was used to present the space-domain Green's function for an inhomogeneously filled waveguide [6]. In addition to being a somewhat tedious approach, the vector potentials used in [6] to generate the electromagnetic fields are the M, N, and L functions described in [17]. The magnetic and electric vector potentials, A and F, respectively, [18] are used in the present work and the electromagnetic fields are obtained as

$$E = \frac{1}{\epsilon}\nabla \times F - j\omega A + \frac{1}{j\omega\mu\epsilon}\nabla\nabla\cdot A \tag{1a}$$

$$H = \frac{1}{\mu}\nabla \times A + j\omega F - \frac{1}{j\omega\mu\epsilon}\nabla\nabla\cdot F. \tag{1b}$$

Fig. 1 shows an infinitesimal current source located within a rectangular waveguide that is inhomogeneously loaded with N isotropic, lossy dielectric layers. This waveguide is represented as the superposition of three parallel-plate structures. We begin by considering the total field maintained by J as a superposition of primary and scattered fields.

Primary electromagnetic fields are generated from the primary vector potentials A_p and F_p, and must satisfy only the boundary conditions imposed by the equivalent parallel-plate waveguide containing J. In general, J will have one component normal to layer interfaces, $\hat{a}_n J_n$, and one component tangential to them, $\hat{a}_t J_t$. For an arbitrarily oriented electric current in the nth layer, the relevant primary field boundary conditions at the source are

$$\hat{a}_n \times (E_{p>} - E_{p<}) = 0 \tag{2a}$$

$$\hat{a}_n \times (H_{p>} - H_{p<}) = \hat{a}_t J_t \tag{2b}$$

$$\nabla^2 A_p + k^2 A_p = -\mu \hat{a}_n J_n \tag{2c}$$

where the ($\gtrless$) represents ($x \gtrless x'$). Separate application of equations (2) for each component of J yields the desired primary field terms. Scattered fields in the nth layer are derived from $A_s^{(n)}$ and $F_s^{(n)}$ where

$$\nabla^2 A_s^{(n)} + k^2 A_s^{(n)} = 0 \tag{3a}$$

$$\nabla^2 F_s^{(n)} + k^2 F_s^{(n)} = 0, \qquad n = 1,2,\cdots,N. \tag{3b}$$

$A_s^{(n)}$ and $F_s^{(n)}$ must satisfy the boundary conditions imposed by the shorted, dielectric-filled parallel-plate structures. Primary fields result directly from J and exist only in the layer where J is nonzero. The scattered fields result when the dielectric layers and conducting walls are added to the primary structure.

The total field in any layer maintained by J must satisfy the usual source and interface boundary conditions. Both primary and scattered potentials are chosen to be x-directed so that the resulting LSM and LSE fields decouple [3]. The proper eigenfunction expansions for these fields may now be deduced. The primary potentials are

$$A_{x_p} = \frac{1}{2\pi}\int_{-\infty}^{\infty} dk_z \sum_m \tilde{a}_{x_m}(k_z|x, y|x', y')\, e^{-jk_z(z-z')} \tag{4a}$$

$$F_{x_p} = \frac{1}{2\pi}\int_{-\infty}^{\infty} dk_z \sum_m \tilde{f}_{x_m}(k_z|x, y|x', y')\, e^{-jk_z(z-z')}. \tag{4b}$$

The scattered potentials are written as

$$A_{x_s}^{(i)} = \frac{1}{2\pi}\int_{-\infty}^{\infty} dk_z \sum_m A_m^{(l)} \tilde{a}_{x_m}^{(i)}(k_z|x, y|x', y')\, e^{-jk_z(z-z')} \tag{5a}$$

$$F_{x_s}^{(i)} = \frac{1}{2\pi}\int_{-\infty}^{\infty} dk_z \sum_m F_m^{(l)} \tilde{f}_{x_m}^{(i)}(k_z|x, y|x', y')\, e^{-jk_z(z-z')} \tag{5b}$$

where i denotes the layer and

$$\begin{aligned} &l = N, && i = n+1,\cdots,N \\ &l = n, && \text{when } i = n \\ &l = 1, && i = 1,\cdots,n-1. \end{aligned}$$

J is assumed to be in the nth layer and $A_m^{(l)}$ and $F_m^{(l)}$ are the unknown scattered vector potential amplitude coefficients in the lth layer, where $l = 1, n, N$. All boundary conditions in the rectangular waveguide are satisfied except those at $x = x_T$ and $x = x_B$. These boundary conditions are written as

$$E_{y_p}^{(n)}{}_{\gtrless} + E_{y_s}^{(n)} = E_{y_s}^{(n\pm1)} \tag{6a}$$

$$E_{z_p}^{(n)}{}_{\gtrless} + E_{z_s}^{(n)} = E_{z_s}^{(n\pm1)} \tag{6b}$$

$$H_{y_p}^{(n)}{}_{\gtrless} + H_{y_s}^{(n)} = H_{y_s}^{(n\pm1)} \tag{6c}$$

$$H_{z_p}^{(n)}{}_{\gtrless} + H_{z_s}^{(n)} = H_{z_s}^{(n\pm1)} \tag{6d}$$

where the ($\gtrless$) and ($\pm$) are for $\begin{pmatrix} x = x_T \\ x = x_B \end{pmatrix}$. The primary fields are obtained from (1) with $A = \hat{a}_x A_{x_p}$ and $F = \hat{a}_x F_{x_p}$. The scattered fields are obtained similarly with $A = \hat{a}_x A_{x_s}^{(i)}$ and $F = \hat{a}_x F_{x_s}^{(i)}$, $i = 1,2\cdots,N$. Since LSM and LSE fields are orthogonal [18], the inhomogeneous 8×8 set of equations resulting from (6) decouples into four inhomogeneous 2×2 sets of equations. Solving for $A_m^{(N)}$, $F_m^{(N)}$, $A_m^{(n)}$, $F_m^{(n)}$, $A_m^{(1)}$, and $F_m^{(1)}$ and combining with (1a), (4), and (5) yields the integral representation of the electric field any-

where in the waveguide:

$$\boldsymbol{E}(x, y, z|x', y', z') = \frac{1}{2\pi}\int_{-\infty}^{\infty} dk_z \sum_m \hat{a}_e \tilde{e}_m \cdot (k_z|x, y|x', y') e^{-jk_z(z-z')} \quad (7)$$

where $\hat{a}_e$ is a unit vector along the direction of the electric field.

The remaining task is to complete the inverse Fourier transform of (7). This integral may be evaluated via the calculus of residues since no branch points exist in the integrand. In general, $\tilde{e}_m$ is made up of LSM and LSE contributions. For both LSM and LSE modes, the inversion contour in the k_z plane is closed in the lower half for $z < z'$ and in the upper half for $z > z'$. The distribution of poles in he k_z plane is symmetric about the origin. Completing the inverse transform of (7) for each component of the electric field yields the dyadic Green's function:

$$\bar{\bar{G}}_E(x|x', y|y', z|z') = \sum_n \sum_m \bar{\bar{G}}_{nm}^{\mathrm{LSM}} + \sum_p \sum_m \bar{\bar{G}}_{pm}^{\mathrm{LSE}} \quad (8a)$$

where the electric field due to an arbitrary electric current is now given by

$$\boldsymbol{E}(x, y, z) = \iiint \bar{\bar{G}}_E(x, y, z|x', y', z') \cdot \boldsymbol{J}(x', y', z')\, dx'\, dy'\, dz'. \quad (8b)$$

Equations (8a) and (8b) give the space-domain Green's function, which is useful for three-dimensional problems. For the analysis of two-dimensional problems, fields described in the form of (7) are appropriate. The method presented here may also be applied to structures containing an arbitrary number of electric and magnetic sources.

III. Dispersion Analysis

The shielded microstrip structures illustrated in Fig. 2 are characterized by their respective coupled integral equations:

$$\begin{bmatrix} G_{yy} & G_{yz} \\ G_{zy} & G_{zz} \end{bmatrix} * \begin{bmatrix} J_y \\ J_z \end{bmatrix} = \begin{bmatrix} E_y \\ E_z \end{bmatrix} \quad (9)$$

The components of the Green's matrices are derived in integral form for a three-layer waveguide, as in (7), with the infinitesimal source located in region (2). The expansions for J_y and J_z are chosen to satisfy their respective edge conditions [19]. The convolution integrals resulting from (9) are evaluated in closed form. Using one expansion term for J_y and J_z and applying the Galerkin's procedure to (9) shows

$$\begin{bmatrix} \sum_{\substack{m=1 \\ \text{odd}}}^{M} P_{1m} & \sum_{\substack{m=1 \\ \text{odd}}}^{M} Q_{1m} \\ \sum_{\substack{m=1 \\ \text{odd}}}^{M} S_{1m} & \sum_{\substack{m=1 \\ \text{odd}}}^{M} U_{1m} \end{bmatrix} \begin{bmatrix} c_1 \\ d_1 \end{bmatrix} = \begin{bmatrix} 0 \\ 0 \end{bmatrix} \quad (10)$$

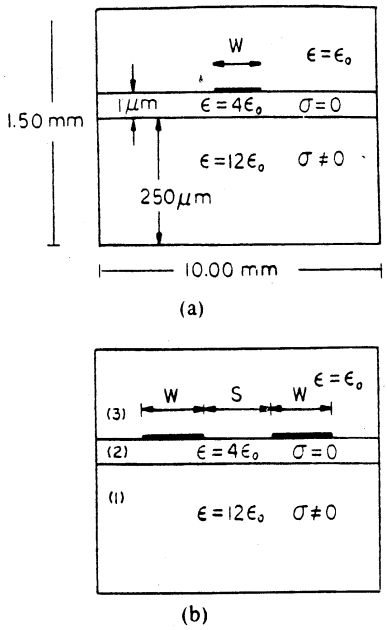

Fig. 2. Geometry of single and coupled microstrip slow-wave structures.

where c_1 is the unknown amplitude coefficient for the first expansion term of J_y, and d_1 similarly results from J_z.

For both single and coupled line structures the expressions for P_{1m}, Q_{1m}, S_{1m}, and U_{1m} are relatively simple combinations of Bessel and trigonometric functions. These are given in the Appendix. Setting the determinant of the current amplitude matrix to zero and solving for its roots yields the complex microstrip propagation constant $k_z = \beta - j\alpha$ for the respective structures.

IV. Numerical Results

The dispersion characteristics given in this section are for the single and coupled strip MIS structures illustrated in Fig. 2. The pertinent dimensions are also given there. Region 1 is the conducting Si substrate with $\epsilon_{r1} = 12$ and region 2 is the SiO_2 insulating region with $\epsilon_{r2} = 4$. The effect of the induced conduction current is incorporated into a complex permittivity in region 1. The normalized wavelength and the attenuation constant for different cases are plotted in Figs. 3–10. Good convergence was obtained using one expansion term for the microstrip current components and $M = 501$ in the four truncated series in (10). Roots of the matrix were found using Mueller's method with deflation.

Figs. 3 and 4 show a comparison of phase and attenuation constants between this theory, spectral analysis, finite element method, and experimental results for a narrow single MIS line with $w = 160$ μm. Dispersion characteristics for a wide single MIS line with $w = 600$ μm are compared with other full-wave methods, parallel-plate model results, and experimental results in Figs. 5 and 6. Good agreement between this theory, experiment, and other full-wave methods for λ/λ_0 and α is found in all cases studied for the single MIS line with $w = 160$ μm. Results for the wider strip, $w = 600$ μm, show discrepancies between his theory and the spectral-domain approach

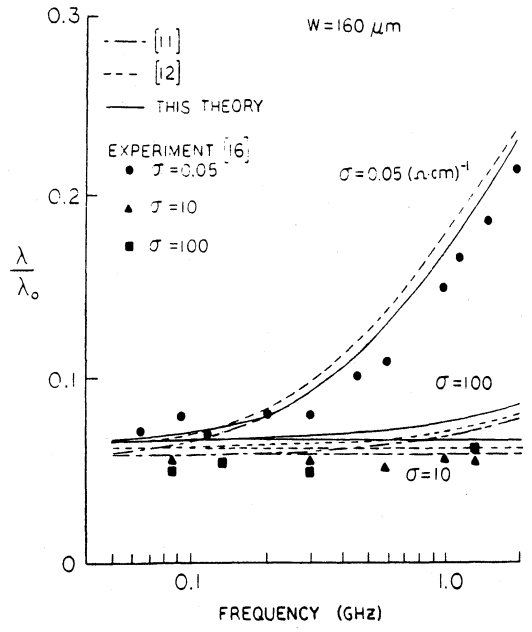

Fig. 3. Comparison of normalized wavelength for single microstrip ($w = 160$ μm) with spectral-domain analysis [11], finite element method [12], and experimental results [16].

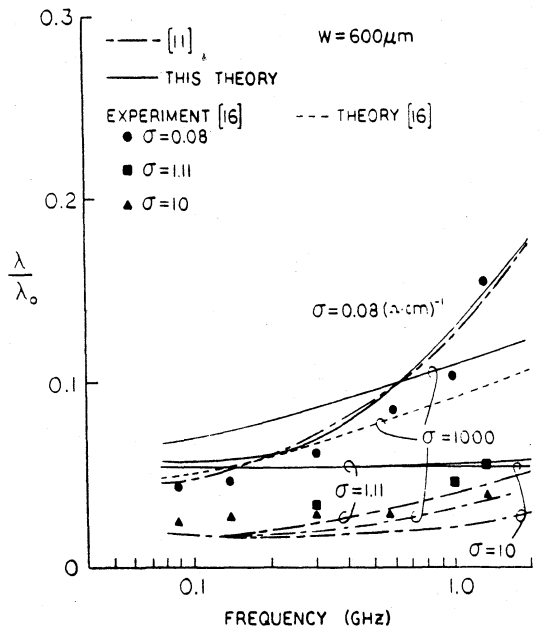

Fig. 5. Comparison of normalized wavelength for single microstrip ($w = 600$ μm) with spectral-domain analysis [11], experimental results [16], and parallel-plate model [16].

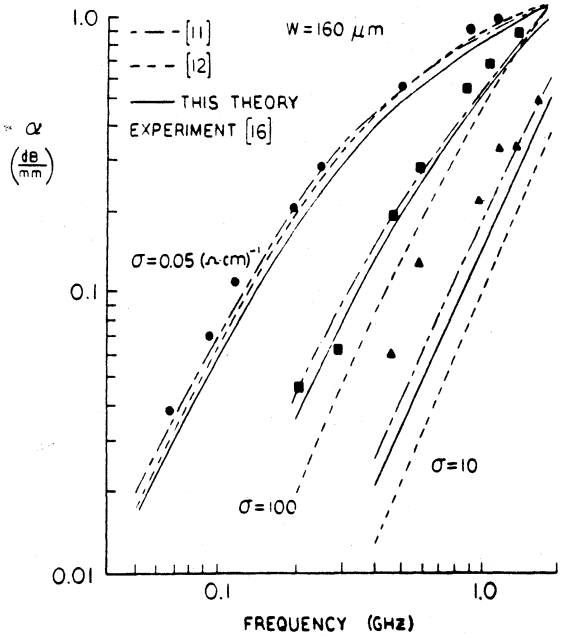

Fig. 4. Comparison of attenuation constant for single microstrip ($w = 160$ μm) with spectral-domain analysis [11], finite element method [12], and experimental results [16].

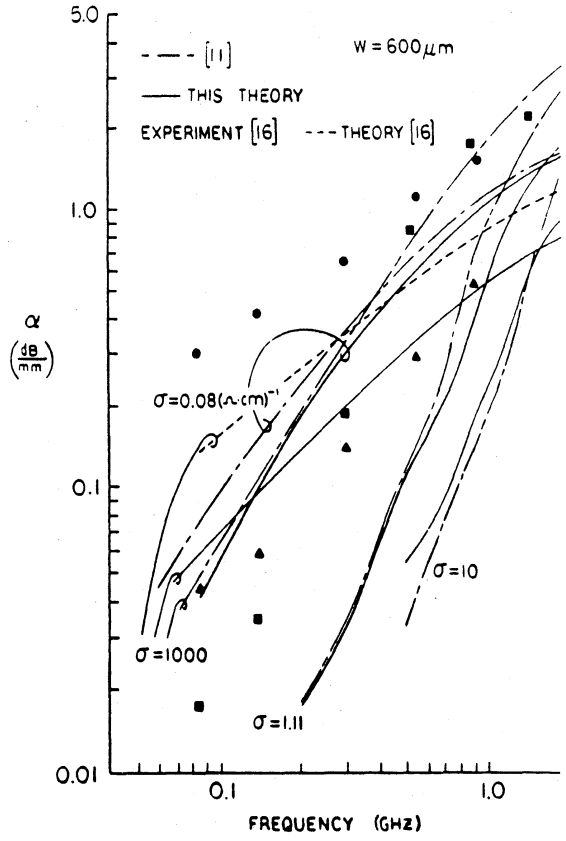

Fig. 6. Comparison of attenuation constant for single microstrip ($w = 600$ μm) with spectral-domain analysis [11], experimental results [16], and parallel-plate model [16].

for larger substrate conductivities. For the case $\sigma = 1000$ and $f = 1$ GHz, the spectral analysis finds a very low normalized wavelength of about 0.04. This value is unacceptable considering that the Si substrate is five skin depths thick. As a result, the electromagnetic fields are virtually shielded from the semiconducting layer. This drives the line into the skin effect and not the slow-wave mode. Results derived by the method presented in this paper indicate such a tendency. Curves generated from the parallel-plate analysis (applicable to wide microstrips) [16] are also plotted in Figs. 5 and 6 and are in agreement with our theoretical data.

Discrepancies between this theory and experimental results are also evident for the wide-strip case. Consequently, to verify the accuracy of this approach when applied to wide strips, a comparison of normalized dominant mode phase constant for the $w/h = 2$ structure analyzed in [20] was made. Virtual exact agreement was found for the

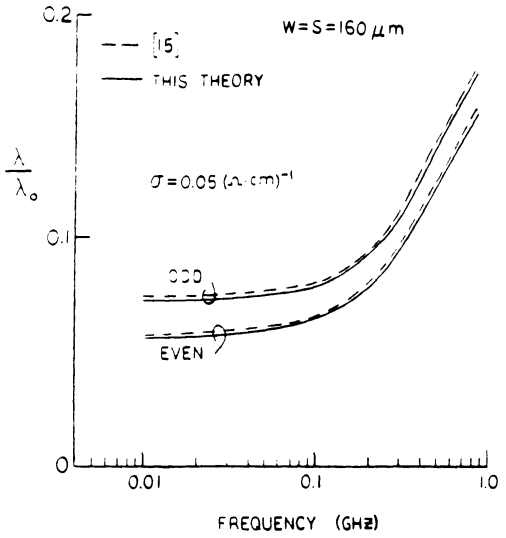

Fig. 7. Comparison of normalized wavelength for even- and odd-mode excitation of coupled microstrip lines with spectral-domain analysis [15].

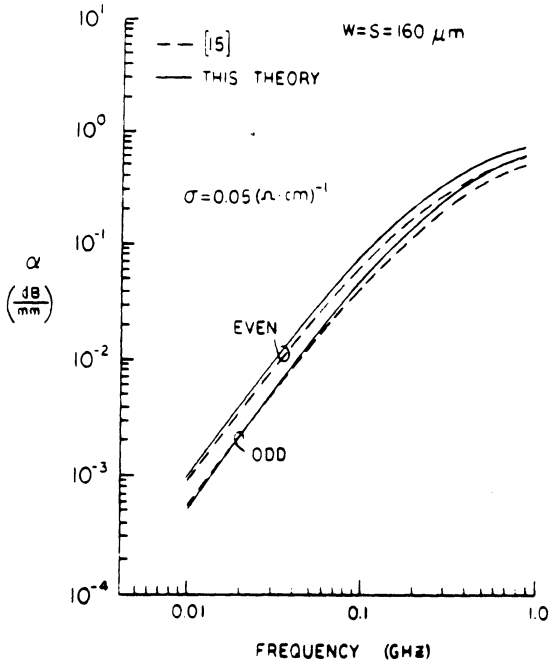

Fig. 8. Comparison of attenuation constant for even- and odd-mode excitation of coupled microstrip lines with spectral-domain analysis [15].

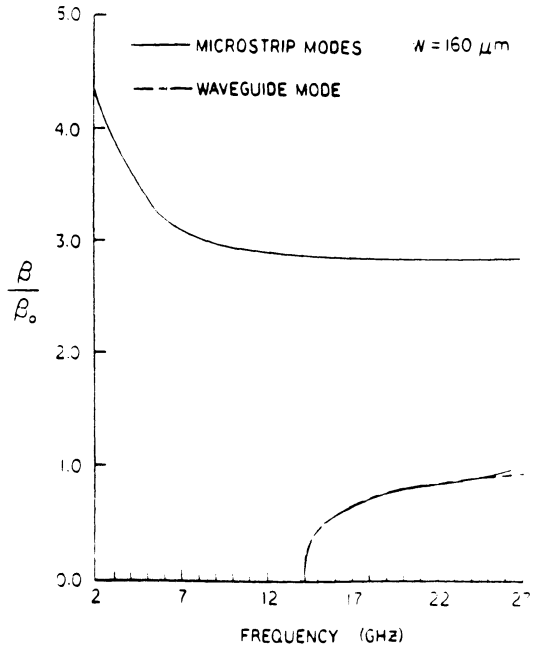

Fig. 9. Frequency-phase constant characteristics or first two modes of single microstrip and dominant mode of inhomogeneously filled waveguide.

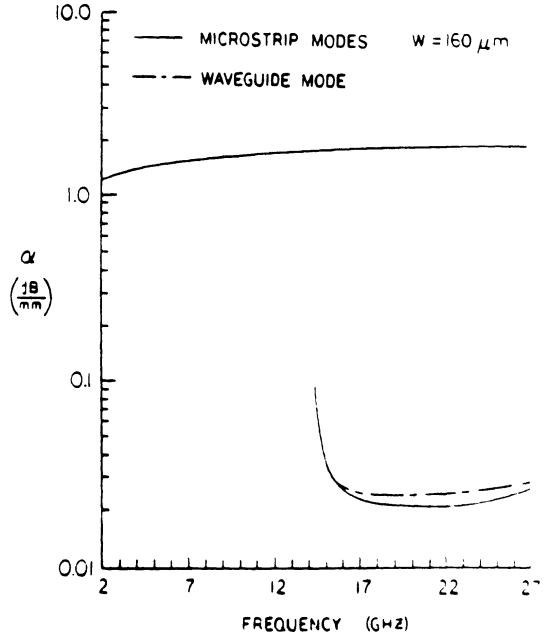

Fig. 10. Frequency-attenuation constant characteristics for first two modes of single microstrip and dominant mode of inhomogeneously filled waveguide.

entire frequency range studied (1–100 GHz). Phase and attenuation constants for the coupled line MIS structure are shown in Figs. 7 and 8. The propagation characteristics found using this theory compare very well with the spectral analysis results. Fig. 7 shows λ/λ_0 for even- and odd-mode excitation and Fig. 8 shows the comparison of α for even- and odd-mode excitation.

The last two sets of data, Figs. 9 and 10, show the frequency dependence of phase and attenuation constants for the first two modes of the single MIS line with $w = 160$ μm and the dominant mode of the rectangular waveguide (no strip). These results show a clear correlation between the second microstrip mode and dominant waveguide mode dispersion characteristics over the entire frequency range studied. This phenomenon was also reported in [20] for a lossless dielectric substrate.

The amount of time required to find a solution to the determinantal equation (10) ranged from 55 seconds for small values of the loss tangent in region (1) (i.e., $\sigma = 0.05$, $f = 1$ GHz) to 285 seconds for larger values (i.e., $\sigma = 1000$, $f = 0.5$ GHz). These calculations were done on a personal computer.

V. Conclusion

This paper has presented a simple, efficient technique for deriving a physically appealing space-domain Green's function in a shielded layered region containing an arbitrary number of magnetic and/or electric sources. Obtain-

ing unknown amplitude coefficients reduces to the solution of 2×2 inhomogeneous sets of equations, depending on the number of different layers containing sources. The Green's function for an inhomogeneously filled waveguide was derived and used to find dispersion characteristics for various MIS slow-wave structures. The corresponding characteristic equations are given in an appendix. The accuracy of the results was verified by a comparison with other published data, thus establishing the validity of the theory presented.

Appendix
Expressions for P_{1m}, Q_{1m}, S_{1m}, and U_{1m} for Single and Coupled Lines

A. Single MIS Line

$$P_{1m} = -C_1C_3^2K_1$$

$$U_{1m} = C_1C_2^2K_2$$

$$Q_{1m} = S_{1m} = C_1C_2C_3K_3.$$

B. Coupled MIS Lines

Even mode:

$$P_{1m} = -C_1C_3^2C_4^2K_1$$

$$U_{1m} = C_1C_2^2C_4^2K_2$$

$$Q_{1m} = S_{1m} = C_1C_2C_3C_4^2K_3.$$

Odd mode:

$$P_{1m} = -C_1C_3^2C_5^2K_1$$

$$U_{1m} = C_1C_2^2C_5^2K_2$$

$$Q_{1m} = S_{1m} = C_1C_2C_3C_5^2K_3$$

where

$$C_1 = \frac{j2\omega\mu_0}{b\left[\left(\frac{m\pi}{b}\right)^2 + k_z^2\right]}$$

$$C_2 = J_0\left(\frac{m\pi w}{2b}\right)$$

$$C_3 = \frac{\sin\left(\frac{m\pi w}{2b}\right)}{\left[\left(\frac{m\pi w}{2b}\right)^2 - \pi^2\right]}$$

$$C_4 = \cos\left[\frac{m\pi}{2b}(s+w)\right]$$

$$C_5 = \sin\left[\frac{m\pi}{2b}(s+w)\right]$$

and

$$K_1 = \left[\left(\frac{k_x^{(2)}k_x^{(3)}\left(\frac{m\pi}{b}\right)^2}{k_0^2}\right)T_{\mathrm{LSM}} - k_z^2T_{\mathrm{LSE}}\right]$$

$$K_2 = \left[\left(\frac{k_x^{(2)}k_x^{(3)}k_z^2}{k_0^2}\right)T_{\mathrm{LSM}} - \left(\frac{m\pi}{b}\right)^2T_{\mathrm{LSE}}\right]$$

$$K_3 = \left(\frac{m\pi}{b}\right)k_z\left[\left(\frac{k_x^{(2)}k_x^{(3)}}{k_0^2}\right)T_{\mathrm{LSM}} + T_{\mathrm{LSE}}\right]$$

$$T_{\mathrm{LSM}} = \frac{N_{\mathrm{LSM}}}{D_{\mathrm{LSM}}}$$

$$T_{\mathrm{LSE}} = \frac{N_{\mathrm{LSE}}}{D_{\mathrm{LSE}}}$$

$$N_{\mathrm{LSM}} = \tan\left(k_x^{(3)}d_3\right)\left[\epsilon_{r_1}k_x^{(2)}\tan\left(k_x^{(2)}d_2\right) + \epsilon_{r_2}k_x^{(1)}\tan\left(k_x^{(1)}d_1\right)\right]$$

$$N_{\mathrm{LSE}} = \tan\left(k_x^{(3)}d_3\right)\left[k_x^{(2)}\tan\left(k_x^{(1)}d_1\right) + k_x^{(1)}\tan\left(k_x^{(2)}d_2\right)\right]$$

$$D_{\mathrm{LSM}} = \epsilon_{r_2}k_x^{(3)}\tan\left(k_x^{(3)}d_3\right)\left[\epsilon_{r_2}k_x^{(1)}\tan\left(k_x^{(1)}d_1\right)\tan\left(k_x^{(2)}d_2\right) - \epsilon_{r_1}k_x^{(2)}\right] - k_x^{(2)}\left[\epsilon_{r_1}k_x^{(2)}\tan\left(k_x^{(2)}d_2\right) + \epsilon_{r_2}k_x^{(1)}\tan\left(k_x^{(1)}d_1\right)\right]$$

$$D_{\mathrm{LSE}} = k_x^{(3)}\left[k_x^{(2)}\tan\left(k_x^{(1)}d_1\right) + k_x^{(1)}\tan\left(k_x^{(2)}d_2\right)\right] + k_x^{(2)}\cdot\tan\left(k_x^{(3)}d_3\right)\left[k_x^{(1)} - k_x^{(2)}\tan\left(k_x^{(1)}d_1\right)\tan\left(k_x^{(2)}d_2\right)\right]$$

and

$$k_x^{(i)} = \sqrt{\omega^2\mu_0\epsilon_i - \left(\frac{m\pi}{b}\right)^2 - k_z^2}, \qquad i = 1,2,3.$$

References

[1] R. A. Pucel, "Design considerations for monolithic microwave circuits," *IEEE Trans. Microwave Theory Tech.*, vol. MTT-29, pp. 513–534, June 1981.

[2] R. S. Pengelly, "Hybrid vs. monolithic microwave circuits—A matter of cost," *Microwave Syst. News*, pp. 77–114, Jan. 1983.

[3] N. K. Das and D. M. Pozar, "A generalized spectral-domain Green's function for multilayer dielectric substrates with application to multilayer transmission lines," *IEEE Trans. Microwave Theory Tech.*, vol. MTT-35, pp. 326–335, Mar. 1987.

[4] L. Beyne and D. De Zutter, "Green's function for layered lossy media with special application to microstrip antennas," *IEEE Trans. Microwave Theory Tech.*, vol. 36, pp. 875–881, May 1988.

[5] T. Sphicopoulos, V. Theodoris, and F. Gardiol, "Dyadic Green's function for the electromagnetic field in multilayered isotropic media: An operator approach," *Proc. Inst. Elec. Eng.*, vol. 132, pt. H, no. 5, pp. 329–334, Aug. 1985.

[6] C. T. Tai, "Dyadic Green's function for a rectangular waveguide filled with two dielectrics," *J. Electromagnetic Waves and Appl.*, vol. 2, no. 3/4, pp. 245–253, 1988.

[7] L. P. Dunleavy and P. B. Katehi, "A generalized method for analyzing shielded thin microstrip discontinuities," *IEEE Trans. Microwave Theory Tech.*, vol. 36, pp. 1758–1766, Dec. 1988.

[8] L: Dunleavy and P. Katehi, "Shielding effects in microstrip discontinuities," *IEEE Trans. Microwave Theory Tech.*, vol. 36, pp. 1767–1774, Dec. 1988.

[9] P. B. Katehi and N. G. Alexopoulos, "Frequency-dependent characteristics of microstrip discontinuities in millimeter-wave integrated circuits," *IEEE Trans. Microwave Theory Tech.*, vol. MTT-33, pp. 1029–1035, Oct. 1985.

[10] R. W. Jackson and D. M. Pozar, "Full-wave analysis of microstrip open-end and gap discontinuities," *IEEE Trans. Microwave Theory Tech.*, vol. MTT-33, pp. 1036–1042, Oct. 1985.

11] P. Kennis and L. Faucon, "Rigorous analysis of planar MIS transmission lines," *Electron. Lett.*, vol. 17, no. 13, pp. 454–456, June 1981.
12] M. Aubourg, J. Villotte, F. Godon and Y. Garault, "Finite element analysis of lossy waveguides—Applications to microstrip lines on semiconductor substrate," *IEEE Trans. Microwave Theory Tech.*, vol. MTT-31, pp. 326–330, Apr. 1983.
13] C. Krowne, "Slow-wave propagation in generalized cylindrical waveguides loaded with a semiconductor," *Int. J. Electron.*, vol. 58, no. 2, pp. 249–269, 1985.
14] C. Tzuang and T. Itoh, "Finite-element analysis of slow-wave Schottky contact printed lines," *IEEE Trans. Microwave Theory Tech.*, vol. MTT-34, pp. 1483–1489, Dec. 1986.
15] T. Mu and T. Itoh, "Characteristics of multiconductor, asymmetric, slow-wave microstrip transmission lines," *IEEE Trans. Microwave Theory Tech.*, vol. MTT-34, pp. 1471–1477, Dec. 1986.
16] H. Hesegawa, M. Furukawa, and H. Yanai, "Properties of microstrip line on Si–SiO_2 system," *IEEE Trans. Microwave Theory Tech.*, vol. MTT-19, pp. 869–881, Nov. 1971.
17] C. T. Tai, *Dyadic Green's Functions in Electromagnetic Theory*. Scranton, PA: Intext, 1971.
18] R. Harrington, *Time Harmonic Electromagnetic Fields*. New York: McGraw-Hill, 1961.
19] K. Gupta, R. Garg, and I. Bahl, *Microstrip Lines and Slotlines*. Norwood, MA: Artech House, 1979.
20] E. Yamashita and K. Atsuki, "Analysis of microstrip-like transmission lines by nonuniform discretization of integral equations," *IEEE Trans. Microwave Theory Tech.*, vol. MTT-24, pp. 195–200, Apr. 1976.

✠

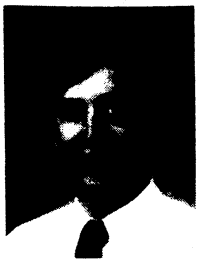

Thomas G. Livernois was born in Grosse Pointe, MI, on July 2, 1962. He received the B.S.E.E. degree (with honor) in 1984 from Michigan Technological University and the M.S.E.E. degree in 1986 from Michigan State University. Since September 1987, he has been working toward the Ph.D. degree in electrical engineering at the University of Michigan, Ann Arbor. His research interests are in the areas of integrated microwave circuits and dielectric waveguides.

From February 1987 to May 1989 he was an Instructor in electrical engineering at Lawrence Technological University, Southfield, MI.

Mr. Livernois is a member of the Engineering Society of Detroit, Lambda Chi Alpha, and an associate member of Sigma Xi.

✠

Pisti B. Katehi (S'81–M'84) received the B.S.E.E. degree from the National Technical University of Athens, Greece, in 1977 and the M.S.E.E. and Ph.D. degrees from the University of California, Los Angeles, in 1981 and 1984 respectively.

In September 1984 she joined the faculty of the EECS Department of the University of Michigan, Ann Arbor, as an Assistant Professor. Since then, she has been involved in the modeling and computer-aided design of millimeter-wave and near-millimeter-wave monolithic circuits and antennas.

In 1984 Dr. Katehi received the W. P. King Award and in 1985 the S. A. Schelkunoff Award from the Antennas and Propagation Society. In 1987 she received an NSF Presidential Young Investigator Award and a Young Scientist Fellowship awarded from URSI. Dr. Katehi is a member of IEEE AP-S, MTT-S and Sigma Xi.

APPENDIX B

Characterization of Microstrip Discontinuities on Multilayer Dielectric Substrates Including Radiation Losses

W.P. Harokopus and P.B. Katehi

Characterization of Microstrip Discontinuities on Multilayer Dielectric Substrates Including Radiation Losses

WILLIAM P. HAROKOPUS, JR., MEMBER, IEEE, AND PISTI B. KATEHI, SENIOR MEMBER, IEEE

Abstract—A two-dimensional space-domain method of moments treatment of open microstrip discontinuities on multi-dielectric-layer substrates is presented. The full-wave analysis accounts for electromagnetic coupling, radiation, and all substrate effects. The technique has been utilized to characterize commonly used discontinuities on one and two dielectric layers, and numerical results for step, corner, and T-junction discontinuities are included.

I. Introduction

MONOLITHIC circuit applications continue to extend farther into the millimeter-wave range, approaching terahertz frequencies. At these frequencies, planar transmission line structures are required for passive component design. In particular, microstrip components are frequently utilized in MMIC circuit applications. Unfortunately, available microstrip CAD discontinuity and circuit element models fail to account for electromagnetic effects, which become significant with increasing frequency. Without reliable CAD, microwave design engineers will face unacceptably lengthy development cycles.

The preponderance of the available microstrip CAD is based on quasi-static methods [1]–[6], equivalent waveguide models [7]–[10], and semiempirical models [11]. These models require little computational effort, but fail to adequately account for electromagnetic coupling, radiation, and surface wave excitation. Quasi-static methods provide accurate characterization only at lower frequencies, while planar waveguide models contain limited information on dispersion.

Consequently, an analysis accounting for electromagnetic coupling, space wave, and surface wave radiation is required for the characterization of microstrip discontinuities, couplers, and matching elements at higher frequencies. Increasingly powerful computers and innovative techniques make full electromagnetic analysis a realistic alternative in the design of high-frequency microstrip circuits. Full-wave analysis has already demonstrated accuracy in modeling simple microstrip discontinuities on single dielectric layers.

Often, microstrip discontinuities and elements are enclosed in a package or a cavity. Jansen has performed an analysis of irregular covered microstrip elements with a spectral-domain technique [12]. Shielded microstrip discontinuities such as open ends, gaps, stubs [13], and coupled line filters [14] have been studied by the method of moments.

Nonetheless, microstrip is often used in the design of feeding networks for monolithic antenna arrays. Unlike shielded microstrip, open microstrip discontinuities are free to radiate. Also, the microstrip substrate supports surface wave modes. High-frequency microstrip design requires a thorough understanding of these effects. Full electromagnetic solutions have been performed on open microstrip elements which are electrically thin, such as open ends, gaps, and coupled lines [17]–[19]. These solutions are based on the thin strip approximation, and utilize one-dimensional method of moments. Under this assumption, the transverse current component gives a second-order effect and may be neglected. In addition, an analysis of open-end and gap discontinuities in a substrate–superstrate configuration has been performed [20]. More recently, spectral-domain solution was applied to irregular step and stub elements on a single layer [21]. However, the characterization of these microstrip elements is far from complete. The fact that these elements are parts of antenna feeding networks necessitates a serious consideration of the coupling and radiation losses and their effect on the performance of the antenna. In addition, in monolithic arrays, multiple dielectric layers offer many advantages in designing feeding networks: they allow alternative solutions to circuit layouts or can provide protection in the form of superstrates. Furthermore, the appropriate combination of dielectric and semiconducting materials can create circuits with desirable properties such as slow-wave structures. This paper addresses, for the first time, the problem of accurate characterization of microstrip discontinuities on multilayer substrates and carefully studies the effects of this dielectric structure on circuit performance.

The presented full-wave analysis is based on the application of two-dimensional method of moments in the space

Manuscript received March 31, 1989; revised July 24, 1989. This work was supported by the National Science Foundation under Grant ECS-8602536 and by the Army Research Office under Contract DAALO3-k-0088 (23836-EL).

The authors are with the Radiation Laboratory, Electrical Engineering and Computer Science Department, 1301 Beal Ave., University of Michigan, Ann Arbor, MI 48109.

IEEE Log Number 8931087.

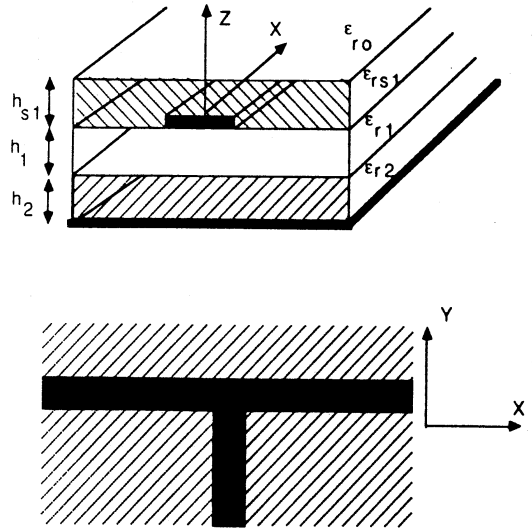

Fig. 1. Multilayer open microstrip geometry.

domain. The dyadic Green's function for a grounded multi-dielectric-layer configuration is employed to develop an algorithm capable of analyzing structures with an arbitrary number of layers. Included in the solution are both transverse and longitudinal current components, allowing the treatment of a wide class of irregular microstrip elements including steps of width, corners, and T junctions. On the microstrip conductors, both current components are expanded by rooftop basis functions. Once the current distribution is evaluated, transmission line theory is employed to determine the network parameters.

Numerical results from this technique have demonstrated excellent agreement with measurement and the spectral-domain technique in the case of single dielectric layers. Scattering parameters will be presented for corner and for T-junction discontinuities on one layer and on more complicated dielectric structures. In addition, on a single layer the more complex geometry of a meander line containing four coupled bends will be presented. The implemented method fully accounts for coupling, space, and surface wave radiation and for all dispersive effects.

II. Analysis

Much of the published work on full-wave analysis of open microstrip discontinuities has been limited to structures with strip widths much smaller than the microstrip wavelength ($w \ll \lambda_g$). Under this approximation, the transverse current component can be considered a second-order effect and neglected [16]. Therefore, analysis was restricted to thin-strip discontinuities such as open ends, gaps, and coupled line filters. Obviously, the transverse current component is critical for the analysis of irregular structures such as steps in width, corners, and T junctions, and is therefore included in this analysis.

The general multilayer open microstrip geometry is shown in Fig. 1. The dielectric layers are considered lossless, but the development is not limited by this assumption. The conductors have infinite conductivity, with the strip conductor being of finite thickness ($t \ll \lambda_g$). Maxwell's equations and the application of Green's identities yield Pocklington's integral equation for the electric field:

$$\vec{E}(\vec{r}) = \int\int_{S'} \bar{\bar{G}}(\vec{r}, \vec{r}') \cdot \vec{J}(x', y')\, dx'\, dy' \tag{1}$$

where $\vec{E}(\vec{r})$ is the total electric field at the point $\vec{r} = (x, y, z)$, $\vec{J}(x', y')$ is the unknown current on the microstrip conducting strip, and $\bar{\bar{G}}(\vec{r}, \vec{r}')$ is the dyadic Green's function for x- and y-directed Hertzian dipoles above a grounded multilayer slab.

To provide for the most general solution possible, strip conductors may be located on any interface. A general, numerically efficient Green's function for an arbitrary number of layers may be derived by decomposing the fields into LSE and LSM modes with respect to $\hat{z}$ [23]. Cylindrical symmetry may also be exploited by using a Hankel transform in the transverse direction. This results in the one-dimensional boundary value problem, which may be simplified to a two-layer structure by using equivalent impedance boundaries as illustrated in Fig. 2(a). In Fig. 2(b), the equivalent transmission line model for this structure is shown, from which the impedance boundaries can be determined.

After application of the inverse Hankel transform, the solution to the resulting boundary value problem is a compact, computationally efficient space-domain Green's function. For a multilayer geometry with the strip conductor located on the top layer (at the dielectric–air interface) the components of the Green's function are given by

$$G_{xx} = G_{yy} = \frac{\omega\mu_0}{2\pi}\int_0^\infty \lambda J_0(\lambda\rho)\frac{e^{-ju_0 z}}{f_1(\lambda, \epsilon_{r_1}, h_1, \epsilon r_2, h_2, \cdots)}\, d\lambda$$
$$- \frac{1}{2\pi}\frac{d^2}{dx^2}\int_0^\infty \frac{J_0(\lambda\rho)}{\lambda} e^{-ju_0 z}$$
$$\cdot\left[\frac{u_0 u_1}{\omega\epsilon_0}\frac{1}{f_2(\lambda, \epsilon_{r_1}, h_1, \epsilon_{r_2}, h_2, \cdots)}\right.$$
$$\left. - \frac{\omega\mu_0}{f_1(\lambda, \epsilon_{r_1}, h_1, \epsilon_{r_2}, h_2, \cdots)}\right] d\lambda \tag{2}$$

$$G_{xy} = G_{yx} = -\frac{1}{2\pi}\frac{d^2}{dx\,dy}\int_0^\infty \frac{J_0(\lambda_\rho)}{\lambda} e^{-ju_0 z}$$
$$\cdot\left[\frac{u_0 u_1}{\omega\epsilon_0}\frac{1}{f_2(\lambda, \epsilon_{r_1}, h_1, \epsilon_{r_2}, h_2, \cdots)}\right.$$
$$\left. - \frac{\omega\mu_0}{f_1(\lambda, \epsilon_{r_1}, h_1, \epsilon_{r_2}, h_2, \cdots)}\right] d\lambda \tag{3}$$

with $\rho = \sqrt{(x-x')^2 + (y-y')^2}$. In (2) and (3) the semi-infinite integration is over the spectrum of spatial frequencies $\lambda(\lambda^2 = k_x^2 + k_y^2)$, and the parameters $u_n (n = 0, 1, \cdots)$

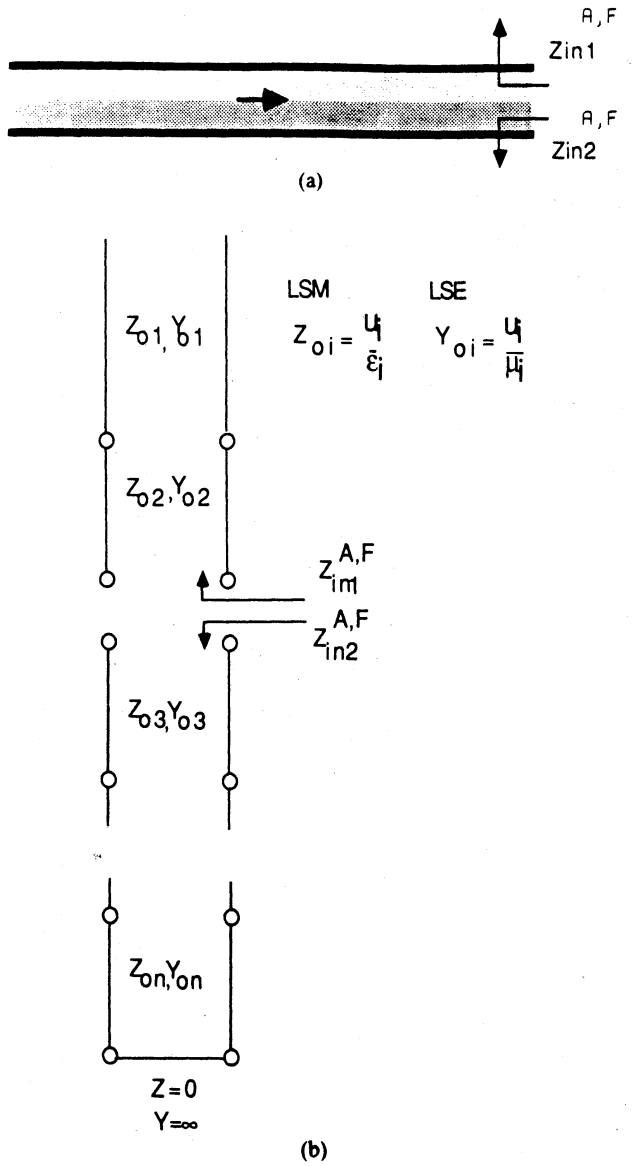

Fig. 2. Derivation of general multilayer Green's function (a) Equivalent impedance boundaries. (b) Transmission line analogue.

are given in terms of λ by the following relation:

$$u_n = \sqrt{k_n^2 - \lambda^2} \tag{4}$$

where k_n is the wavenumber in the nth layer. In addition, in (2) and (3) the functions $f_1(\lambda, \epsilon_{r1}, h_1, \cdots)$ and $f_2(\lambda, \epsilon_{r1}, h1, \cdots)$ are the characteristic equations for the TE and TM surface wave modes, respectively, and have the form

$$f_1(\lambda, \epsilon_{r1}, h_1, \cdots) = u_0 + u_1 \frac{(1 - \Gamma_{f2})}{1 + \Gamma_{f2}} \tag{5}$$

$$f_2(\lambda, \epsilon_{r1}, h1, \cdots) = u_1 + \epsilon_{r1} u_0 \frac{(1 + \Gamma_{a2})}{(1 - \Gamma_{a2})} \tag{6}$$

where Γ_{a2} and Γ_{f2} are the reflection coefficients looking into the substrate, as shown in Fig. 2(b). The surface wave characteristic equations contain all of the information for the dielectric layers not adjacent to the current source within the parameters $\Gamma_{a,f}$. For the case of a single layer, the solution simplifies to the space-domain Sommerfeld Green's function [24], [25]:

$$G_{xx} = G_{yy} = \frac{\omega\mu_0}{2\pi} \int_0^\infty \lambda J_0(\lambda\rho) \frac{e^{-ju_0 z}}{f_1(\lambda, \epsilon_{r1}, h_1)} - \frac{1}{2\pi} \int_0^\infty \frac{d^2}{dx^2} e^{-ju_0 z} \frac{J_0(\lambda\rho)}{\lambda} \cdot \left[\frac{u_0 u_1}{\omega\epsilon_0} \frac{1}{f_2(\lambda, \epsilon_{r1}, h_1)} - \frac{\omega\mu_0}{f_1(\lambda, \epsilon_{r1}, h_1)} \right] d\lambda \tag{7}$$

$$G_{xy} = G_{yx} = -\frac{1}{2\pi} \int_0^\infty \frac{d^2}{dx\,dy} e^{-ju_0 z} \frac{J_0(\lambda\rho)}{\lambda} \cdot \left[\frac{u_0 u_1}{\omega\epsilon_0} \frac{1}{f_2(\lambda, \epsilon_{r_1}, h_1)} - \frac{\omega\mu_0}{f_1(\lambda, \epsilon_{r_1}, h_1)} \right] d\lambda \tag{8}$$

where

$$f_1(\lambda, \epsilon_{r1}, h_1) = u_0 + u_1 \coth ju_1 h_1 \tag{9}$$

$$f_2(\lambda, \epsilon_{r1}, h_1) = \epsilon_r u_0 + u_1 \tanh ju_1 h_1. \tag{10}$$

In the above, ϵ_{r1} is the relative dielectric constant, and h_1 is the thickness of the substrate.

The method of moments [26] is applied to transform Pocklington's integral equation to a system of linear equations. The microstrip discontinuity is subdivided into overlapping squares. The transverse and longitudinal current components on the microstrip are expanded over these squares by finite series

$$J_x = \sum_{n=1}^{N+1} \sum_{m=1}^{M+1} I_{nm}^x j_{nm}^x(x', y') \tag{11}$$

$$J_y = \sum_{n=1}^{N+1} \sum_{m=1}^{M+1} I_{nm}^y j_{nm}^y(x', y') \tag{12}$$

where

$$j_{n,m}^x(x', y') = [f_n(x') g_m(y')] \tag{13}$$

$$j_{n,m}^y(x', y') = [g_n(x') f_m(y')]. \tag{14}$$

In (11) and (12), I_{nm} is the unknown current amplitude at the (n, m)th position of the subdivided element. The functions f_n and g_m are subdomain shaping or basis functions and are consistent with the current boundary conditions. The subdomain basis functions have piecewise-sinusoidal variation in the longitudinal direction and constant variation in the transverse direction according to

$$f_n(x') = \begin{cases} \dfrac{\sin k(x_{n+1} - x')}{\sin kl_x}, & x_n \leqslant x' \leqslant x_{n+1} \\ \dfrac{\sin k(x' - x_{n-1})}{\sin kl_x}, & x_{n-1} \leqslant x' \leqslant x_n \\ 0, & \text{else} \end{cases} \tag{15}$$

and

$$g_m(y') = \begin{cases} 1, & y_{m-1} \leqslant y' \leqslant y_{m+1} \\ 0 & \text{else} \end{cases} \tag{16}$$

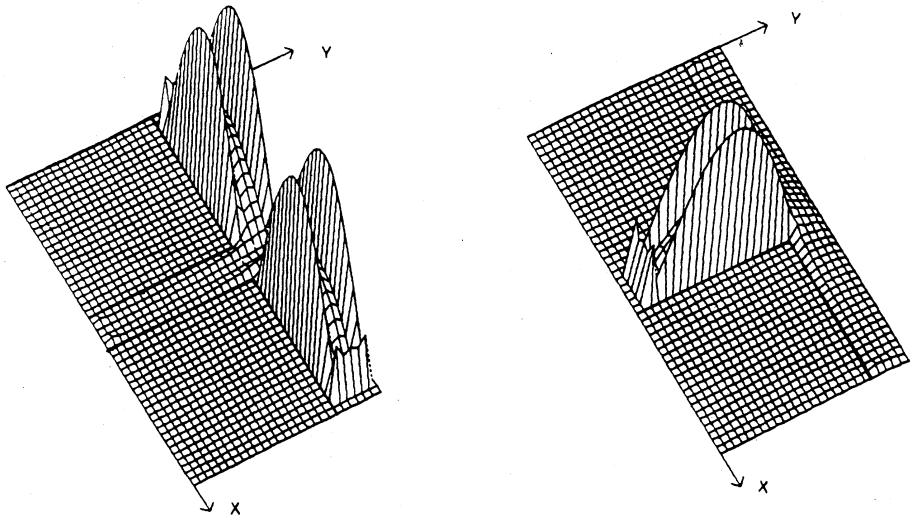

Fig. 3. Current on T junction excited by gap generators ($\epsilon_r = 4$, $h = 0.4$ mm, $W = 0.2$ mm). (a) Current component $J_x(x, y)$. (b) Current component $J_y(x, y)$.

In the above, $l_x = x_{n+1} - x_n$, and k is a scaling parameter chosen to vary between k_0 (free-space wavenumber) and k (wavenumber in the dielectric). The numerical solution has shown that best stability occurs when the scaling constant is chosen close to the guide wavelength. Substitution of the above into Pocklington's integral equation (1) yields a system of linear equations in the form

$$E_x + \Delta E_x = \sum_{n=1}^{N+1} \sum_{m=1}^{M+1} Z_{xx}^{nm} I_x^{nm} + Z_{xy}^{nm} I_y^{nm} \tag{17}$$

$$E_y + \Delta E_y = \sum_{n=1}^{N+1} \sum_{m=1}^{M+1} Z_{yx}^{nm} I_x^{nm} + Z_{yy}^{nm} I_y^{nm} \tag{18}$$

where $Z_{ij}^{nm}(i, j = x, y)$ constitutes the contribution of the jth component of current to the ith component of the electric field from the current element on the (nm)th subdivision. The terms ΔE_x and ΔE_y represent the errors in the electric field due to the approximations made in the current.

During the derivation of the Green's function, all applicable boundary conditions for the grounded multidielectric geometry were applied, with the exception of the condition on the microstrip conductors. This condition, which states that the tangential electric field has to go to zero on the surface of the conducting strips, will be enforced through the method of moments procedure. In addition, it has been shown that Galerkin's procedure represents a strong condition on the minimization of the errors ΔE_x and ΔE_y. For this procedure, the following inner products are defined:

$$V_{\nu\mu}^x = \langle j_{\nu\mu}(\vec{r}), E_x \rangle = \int_{x_{n-1}}^{x_{n+1}} \int_{y_{m-1}}^{y_{m+1}} (E_x + \Delta E_x) f_\nu(x) g_\mu(y)\, dx\, dy \tag{19}$$

$$V_{\nu\mu}^y = \langle j_{\nu\mu}(\vec{r}), E_y \rangle = \int_{x_{n-1}}^{x_{n+1}} \int_{y_{m-1}}^{y_{m+1}} (E_y + \Delta E_y) f_\nu(y) g_\mu(x)\, dx\, dy \tag{20}$$

where $f_\nu(x)$ and $g_\mu(y)$ are testing functions identical to the basis functions and $\nu = 1, \cdots, N+1$, and $\mu = 1, \cdots, M+1$. In view of (19) and (20), equations (17) and (18) result in the following matrix equation:

$$\begin{bmatrix} ZXX_{nm}^{\nu\mu} & ZXY_{nm}^{\nu\mu} \\ ZYX_{nm}^{\nu\mu} & ZYY_{nm}^{\nu\mu} \end{bmatrix} \begin{bmatrix} I_x^{nm} \\ I_y^{nm} \end{bmatrix} = \begin{bmatrix} V_{\nu\mu}^x \\ V_{\nu\mu}^y \end{bmatrix}$$

where $ZIJ_{nm}^{\nu\mu}(I, J = X, Y)$ represent blocks of the impedance matrix, I_i is the vector of unknown x and y current amplitudes, and V_j is the excitation vector which is identically zero everywhere except at the position of the source. Once the matrix inversion is performed, the current amplitudes on the feeding lines are known.

In order to extract the scattering parameters, the discontinuity is excited systematically at all ports by delta gap generators. Assuming a unimodal field excited on the microstrip feeding line, beyond a reference plane the current forms TEM-like standing waves. Transmission line theory can then be used to extract the scattering parameters for a network from the standing wave patterns on the feeding lines. The presence of the gap is reflected in the excitation vector, where

$$V_x^{\nu\mu} = \begin{cases} 1 & \text{if } x_\nu = x_g \\ 0 & \text{else} \end{cases} \tag{21}$$

and

$$V_y^{\nu\mu} = \begin{cases} 1 & \text{if } y_\mu = y_g \\ 0 & \text{else} \end{cases}. \tag{22}$$

In the above, x_g and y_g are positions of an x-oriented and a y-oriented gap generator respectively.

In Fig. 3, the three-dimensional plot depicts the current on a T junction excited at all three of its ports by gap generators. As illustrated, the current assumes a uniform standing wave pattern along the feeding lines of the discontinuity. With a length of feed line longer than that shown, the current SWR and the positions of minima can be determined. The considered minima are away from the discontinuity, far enough for higher order modes to have

vanished. The reflection coefficient at a reference plane $X = L$ looking in any port is

$$\Gamma(L) = \frac{SWR - 1}{SWR + 1} e^{j - 4\pi(L - X_{\min})/\lambda_g} \tag{23}$$

where SWR is the current standing wave ratio, and $X_{\min}$ is the position of a current minimum. The microstrip guide wavelength λ_g has been previously determined from a long open-ended line.

From the reflection coefficient, the normalized input impedance may be determined according to

$$Z_{in} = \frac{1 + \Gamma(L)}{1 - \Gamma(L)}. \tag{24}$$

To evaluate the network parameters, an N-port discontinuiy must be excited by N independent excitations. In the case of a symmetrical two-port, even and odd excitations may be employed. For the even case the gap generators are of equal magnitude and phase, and for the odd case they have equal magnitude and are out of phase by 180°. The even and odd input impedances, obtained from (23) and (24), may be combined to give the elements for the Z matrix, which for the case of a symmetric network take the form

$$Z_{11} = \frac{Z_{in}^{1e} + Z_{in}^{1o}}{2} \tag{25}$$

$$Z_{22} = Z_{11} \tag{26}$$

$$Z_{12} = \frac{Z_{in}^{1o} - Z_{in}^{1e}}{2} \tag{27}$$

$$Z_{12} = Z_{21}. \tag{28}$$

In the above, $Z_{in}^{1e(o)}$ refers to port 1 under an even (odd) excitation. For nonsymmetric networks and multiport networks similar expressions may be obtained. The scattering parameters are obtained from the Z matrix by a simple transformation.

Finally, the total radiation losses may be determined from the known relation

$$\frac{P_{rad}}{P_{in}} = 1 - |S_{11}|^2 - |S_{12}|^2. \tag{29}$$

III. Evaluation of Impedance Matrix Elements

The numerical evaluation of the Sommerfield integrations involved in the Green's function is quite involved. A detailed discussion of the evaluation of the Sommerfeld integrations has been included in a previous work [29] by one of the authors and will not be discussed further here.

In the matrix equation of Section II, the terms $ZXX_{nm}^{\nu\mu}$ and $ZYY_{nm}^{\nu\mu}$ represent the interactions between the x or y components located in the (n, m)th and (ν, μ)th cells. The terms $ZXY_{nm}^{\nu\mu}$ and $ZYX_{nm}^{\nu\mu}$ represent the interaction between the x and y components located in the (n, m)th and (ν, μ)th cells. The computation of all of the 2 $(NM)^2$ interactions would be extremely time consuming. Yet, the number of computations can be greatly reduced noting the following points. For the directly coupled blocks, due to the symmetry and the even valueness of the Green's function with respect to the x and y separations, all interactions between subsections depend only on the magnitudes $|x - x'|$ and $|y - y'|$. For the cross-coupled blocks, the symmetry and the odd valueness of the Green's functions may lead to similar conclusions. Thus, vectors of impedance matrix elements may be precomputed and catalogued according to separations for various substrates and subsection sizes. These libraries can then be used repeatedly for discontinuity analysis.

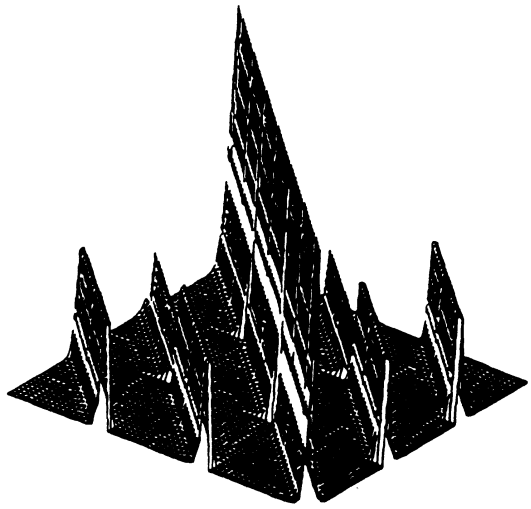

Fig. 4. Toplitz impedance matrix.

A typical impedance matrix is plotted in Fig. 4. As illustrated, the matrix is Toplitz, with the diagonal elements being the largest by an order of magnitude. Although not done in the following results, it appears evident from the figure that interactions of subsections electrically distant may be ignored. This could result in further savings in computer time.

IV. Numerical Results

A. Single-Layer Discontinuities

The presented technique has been applied to characterize the discontinuity shown in Fig. 5(a). This matching section is printed on a 10 mil substrate of relative permittivity 9.9. Over the frequency range of interest, the microstrip section and the substrate thickness are electrically small ($< \frac{1}{10}\lambda_g$). As expected, our moment method algorithm has found radiation losses insignificant for this example. Fig. 5(a) and (b) shows the magnitude and phase of the scattering parameters as compared to measurement. As illustrated, the agreement with measurements for magnitude and phase is excellent. In particular, the agreement of the phase is within 2.5° across this frequency range. The measurements were performed by TI using a cascade prober and an 8510 automatic network analyzer.

1) Radiation Losses: Radiation losses for open microstrip elements can be significant at millimeter-wave frequencies. To illustrate the ability of the analysis presented here to account for space and surface wave losses, a

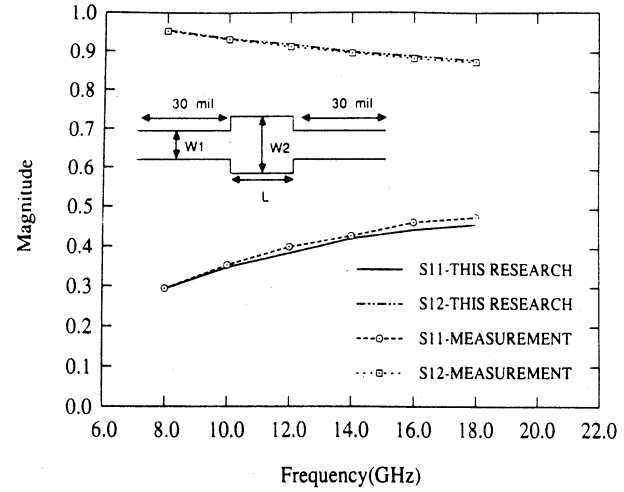

(a)

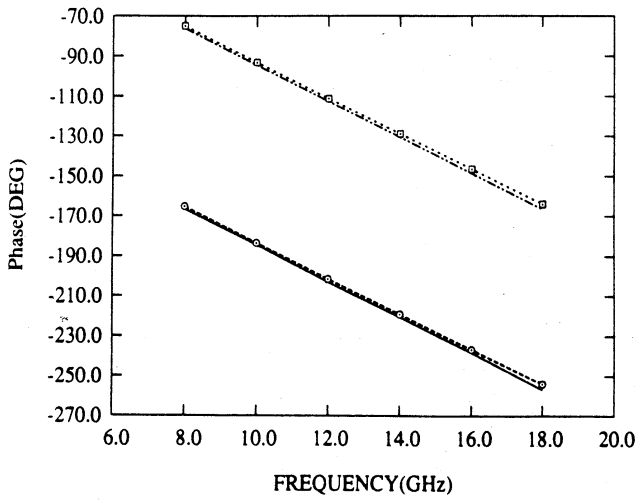

(b)

Fig. 5. Scattering parameters of matching section. Numerical (experimental) dimensions: $W1 = 9.2$ (9.2) mm, $W2 = 23$ (23.1) mm, $L = 50.6$ (50.0), $\epsilon_r = 9.9$, $h = 10$ mil. (a) Magnitude. (b) Phase.

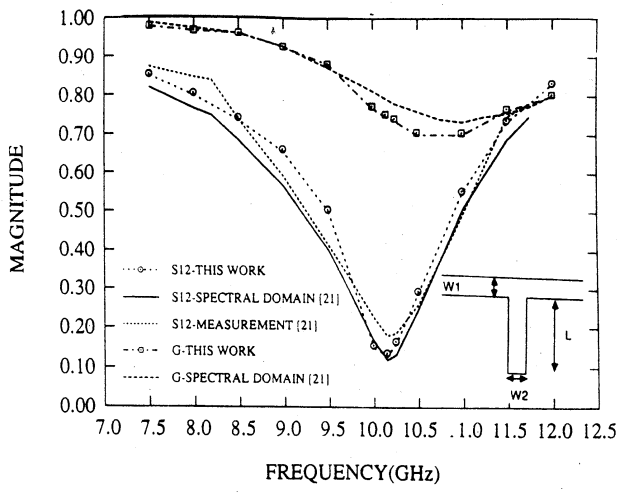

Fig. 6. Scattering Parameters for Microstrip Stub. Space (spectral) dimensions: $W1 = 1.44$ (1.40), $W2 = 1.44$ (1.40), $L = 2.16$ (2.16), $\epsilon_r = 10.65$, $h = 1.27$ mm.

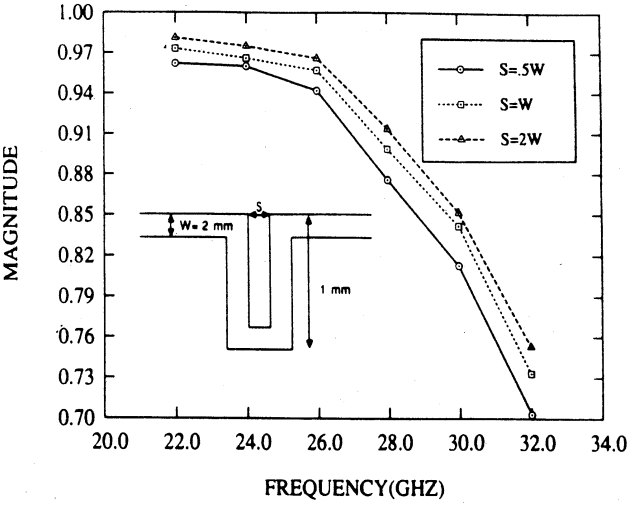

Fig. 7. Design curve for meander line ($\epsilon_r = 9.9$, $h = 10$ mil).

microstrip stub on a single microstrip layer was compared to previously published data obtained with the spectral-domain technique [21]. The microstrip stub contains a T-junction discontinuity and an open end and is printed on a 1.27 mm substrate of dielectric constant 10.65. As illustrated in Fig. 6, the agreement between our space-domain technique and the spectral-domain technique is very good. The quantity denoted G in the graph corresponds to $|S_{11}|^2 + |S_{12}|^2$, which may be subtracted from 1 to determine the total radiated power. The quarter-wave resonance occurs just beyond 10 GHz. Also included in the plot are measurements obtained by Jackson [21].

2) Single-Loop Meander Line: Multiloop meander lines are frequently used in such MMIC's as traveling wave amplifiers for their slow-wave properties. The formulation presented in this paper has been applied to simulate a single-loop meander line in order to illustrate the versatility of the method in modeling irregular microstrip discontinuities. Furthermore, the consideration of a single-loop instead of a multiloop line speeds up the computation and reveals very explicitly the effect of distributed discontinuities and electromagnetic coupling on the slow-wave properties of the structure.

The line is printed on a 10 mil alumina substrate ($\epsilon_r = 9.9$). The magnitude of S_{21} is shown in Fig. 7 as a function of frequency for three values of the width-to-spacing ratio (w/s). In addition, Fig. 8 shows the normalized phase velocity around the loop (v'/v) as a function of frequency, where v is the phase velocity on a microstrip line of length equal to the mean path length of the loop. These results indicate, in this frequency range, that the parasitics in the loop increase the phase velocity v', which in turn tends to reduce the overall slow-wave effect of the meander line.

B. Multilayer Microstrip Discontinuities

A powerful advantage of the presented formulation is its ability to model multilayer substrates by replacing the single-layer Green's function with the multilayer function. The full-wave procedure was applied to a microstrip corner discontinuity on a substrate having two dielectric layers. The magnitudes of the scattering parameters are shown in Fig. 9. The multilayer corner has been analyzed on four different substates: A) a 40 mil layer of alumina

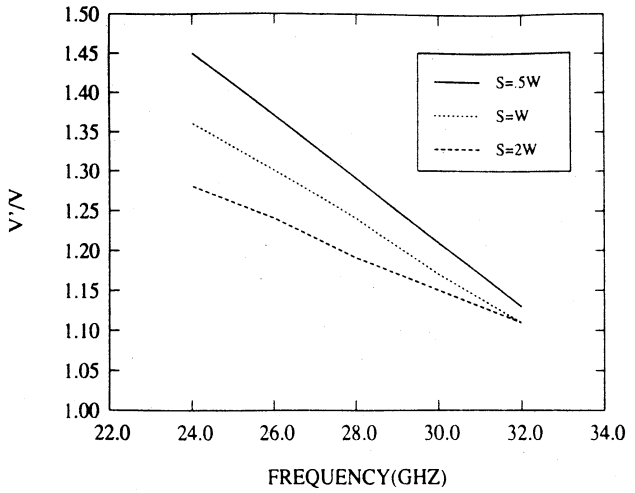

Fig. 8. Phase velocity in meander line.

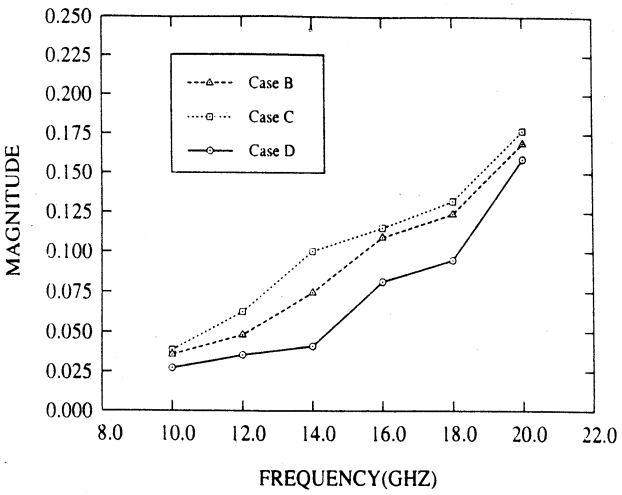

Fig. 10. Radiation from multilayer microstrip corner. $W1 = W2 = 20$ mil.

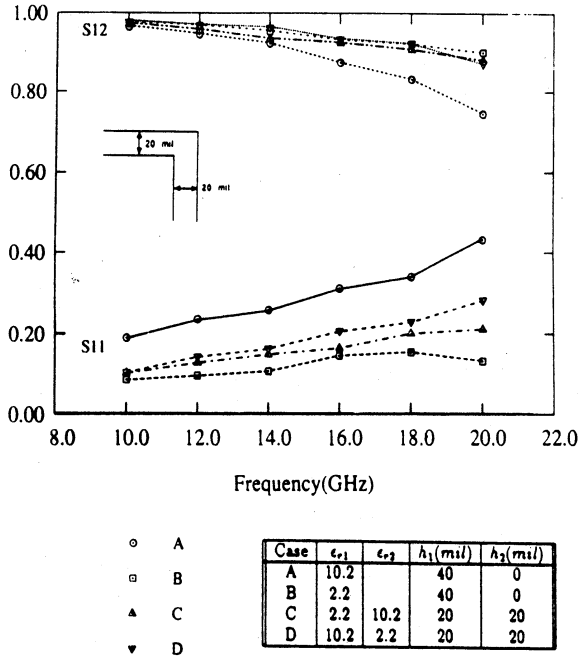

Case	ϵ_{r1}	ϵ_{r2}	$h_1(mil)$	$h_2(mil)$
A	10.2		40	0
B	2.2		40	0
C	2.2	10.2	20	20
D	10.2	2.2	20	20

Fig. 9. Scattering parameters for multilayer microstrip corner. $W1 = W2 = 20$ mil.

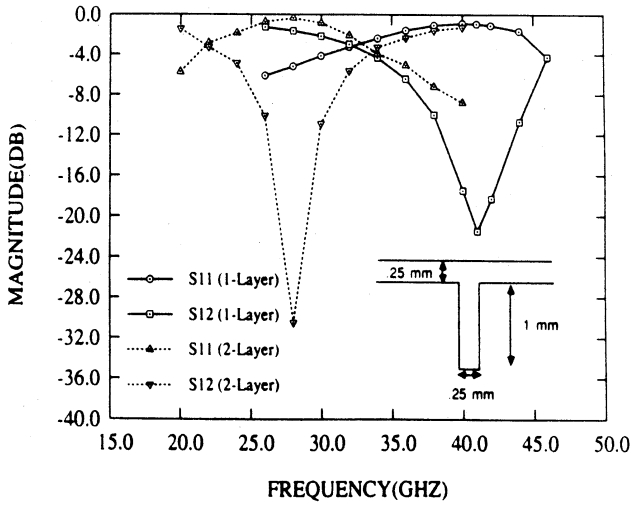

Fig. 11. Scattering parameters for multilayer microstrip stub. $W1 = W2 = 0.2$ mm, $L = 0.6$ mm.

($\epsilon_r = 10.2$); B) a 40 mil layer of Duroid ($\epsilon_r = 2.2$); C) a 20 mil layer of Duroid on a 20 mil layer of alumina; and D) a 20 mil layer of alumina on a 20 mil layer of Duroid.

There is significant difference in radiation between the two multilayer cases. The radiation from the structure having Duroid over alumina is considerably greater than the structure having alumina over Duroid, as illustrated in Fig. 10. It is believed that for this structure the loss is due primarily to surface wave radiation. Therefore, case D couples less power into surface waves than case C. This phenomenon is believed to be related to the suppression of surface wave excitation reported by Jackson [27] in his study of antenna elements.

A two-layer microstrip stub was also analyzed. Shown in Fig. 11 are the magnitudes of the scattering parameters for a stub on substrate having a layer of GaAs ($\epsilon_r = 12.2$) on quartz ($\epsilon_r = 4.0$). Both layers are 0.2 mm thick. Also included are the scattering parameters for a stub having the same dimensions on a single layer of quartz. The single-layer example has a resonant frequency at 41 GHz. The higher effective dielectric constant for the two-layer case creates a stub having a smaller resonant length, and results in a downward shift in frequency for the null of $|S12|$. The radiation losses for both stubs are included in Fig. 12. As illustrated, the multilayer stub shows a tendency to radiate less. This indicates that multilayer substrates may be utilized to reduce radiation losses.

V. Conclusion

A versatile analysis of microstrip discontinuities has been presented. The two dimensional method of moments technique has demonstrated excellent agreement with measurements and other theoretical data derived for a single layer. A powerful extension of the method allows the treatment of discontinuities on more complicated dielectric structures. This is accomplished by employing the Green's function for a conductor-backed multidielectric layer, resulting in the ability to model with full electromagnetic

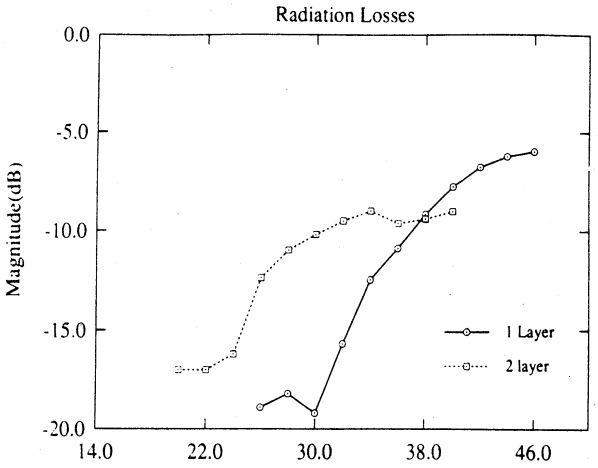

Fig. 12. Radiation from multilayer microstrip stub. $W1 = W2 = 0.2$ mm, $L = 0.6$ mm.

analysis a wide variety of nonuniform microstrip configurations.

Numerical results for corner and T-junction discontinuities have been presented on two dielectric layers. Additionally, the ability of the formulation to model larger elements composed of these building blocks has been demonstrated by the inclusion of a design curve for a meander line.

The full-wave technique accurately accounts for coupling, space wave, and surface wave radiation. Curves of radiation losses are presented for the corner and stub elements.

ACKNOWLEDGMENT

The authors wish to express their gratitude to Dr. S. R. Nelson and A. Crane of Texas Instruments for their contributions to this work.

REFERENCES

[1] M. Maeda, "Analysis of gap in microstrip transmission lines," *IEEE Trans. Microwave Theory Tech.*, vol. MTT-20, pp. 390–396, June 1972.

[2] P. Benedek and P. Silvester, "Equivalent capacitance of microstrip gaps and steps," *IEEE Trans. Microwave Theory Tech.*, vol. MTT-20, pp. 729–733, Nov. 1972.

[3] P. Silvester and P. Benedek, "Equivalent capacitance of microstrip open circuits," *IEEE Trans. Microwave Theory Tech.*, vol. MTT-20, pp. 511–516, Aug. 1972.

[4] P. Silvester and P. Benedek, "Equivalent discontinuities capacitances for right-angle bends, T-junctions, and crossings," *IEEE Trans. Microwave Theory Tech.*, vol. MTT-21, pp. 341–346, May 1973.

[5] R. Horton, "The electrical characterization of right-angle bends in microstrip line," *IEEED Trans. Microwave Theory Tech.*, vol. MTT-21, pp. 427–429, June 1973.

[6] C. Gupta, and A. Gopinath, "Equivalent circuit capacitance for microstrip change in width," *IEEE Trans. Microwave Theory Tech.*, vol. MTT-25, pp. 819–821, Oct. 1977.

[7] T. Itoh, "Analysis of microstrip resonators," *IEEE Trans. Microwave Theory Tech.*, vol. MTT-22, pp. 946–952, Nov. 1974.

[8] I. Wolf, G. Kompa, and R. Mehran, "Calculation method for microstrip discontinuities and T-junctions," *Electron. Lett.*, vol. 8, 1972.

[9] G. Kompa and R. Mehran, "Planar waveguide model for calculating microstrip components," *Electron. Lett.*, vol. 11, 1975.

[10] W. Menzel and I. Wolf, "A method for calculating the frequency dependent properties of microstrip discontinuities," *IEEE Trans. Microwave Theory Tech.*, vol. MTT-25, pp. 107–112, Feb. 1977.

[11] M. Kirschning, R. H. Jansen, and H. L. Koster, "Measurement and computer-aided modeling of microstrip discontinuities by an improved resonator method," in *IEEE MTT-S Int. Microwave Symp. Dig.*, May 1983.

[12] R. H. Jansen, "The spectral domain approach for microwave integrated circuits," *IEEE Trans. Microwave Theory Tech.*, vol. MTT-33, pp. 1043–1056, Oct. 1985.

[13] J. C. Rautio and R. F. Harrington, "An electromagnetic timeharmonic analysis of shielded microstrip circuits," *IEEE Trans. Microwave Theory Tech.*, vol. MTT-35, pp. 726–730, Aug. 1987.

[14] L. P. Dunleavy and P. B. Katehi, "A generalized method for analyzing shielded thin microstrip discontinuities," *IEEE Trans. Microwave Theory Tech.*, vol. 36, pp. 1758–1766, Dec. 1988.

[15] L. P. Dunleavy and P. B. Katehi, "Shielding effects in microstrip discontinuities," *IEEE Trans. Microwave Theory Tech.*, vol. 36, pp. 1767–1774, Dec. 1988.

[16] P. B. Katehi and N. G. Alexopoulos, "On the effect of substrate thickness and permittivity and permittivity on printed circuit dipole performance," *IEEE Trans. Antennas Propagat.*, vol. AP-31, pp. 34–38, Jan. 1983.

[17] N. G. Alexopoulos, P. B. Katehi, and D. Rutledge, "Substrate optimization for integrated circuit applications," *IEEE Trans. Microwave Theory Tech.*, vol. MTT-31, pp. 550–557, July, 1983.

[18] P. B. Katehi and N. G. Alexopoulos, "Frequency-dependent characteristics of microstrip discontinuities in millimeter-wave integrated circuits," *IEEE Trans. Microwave Theory Tech.*, vol. MTT-33, pp. 1029–1035, Oct. 1985.

[19] R. W. Jackson and D. M. Pozar, "Full-wave analysis of microstrip open-end and gap discontinuities," *IEEE Trans. Microwave Theory Tech.*, vol. MTT-33, pp. 1036–1042, Oct. 1985.

[20] H. Yang, N. G. Alexopoulos, and D. R. Jackson, "Analysis of microstrip open-end and gap discontinuities in a substrate-superstrate configuration," *IEEE MTT-S Int. Microwave Symp. Dig.*, June 1988, pp. 705–708.

[21] R. Jackson, "Full-wave finite element analysis of irregular microstrip discontinuities," *IEEE Trans. Microwave Theory Tech.*, vol. 37, pp. 81–89, Jan. 1989.

[22] W. P. Harokopus, Jr., and P. B. Katehi, "An accurate characterization of open microstrip discontinuities including radiation losses," in *IEEE MTT-S Int. Microwave Symp. Dig.*, June 1989, pp. 231–234.

[23] N. K. Das and D. M. Pozar, "A generalized spectral-domain Green's function for multilayer dielectric substrates with application to multilayer transmission lines," *IEEE Trans. Microwave Theory Tech.*, vol. MTT-35, pp. 326–335, Mar. 1987.

[24] A. Sommerfeld, *Partial Differential Equations in Physics*. New York: Academic Press, 1949.

[25] R. S. Elliott, "The Green's function for electric dipoles parallel to and above or within a grounded dielectric slab," Hughes Technical Correspondence, 1978.

[26] R. F. Harrington, *Field Computation By Moment Methods*. New York: Macmillan, 1968.

[27] N. G. Alexopoulos and D. R. Jackson, "Fundamental superstrate (cover) effects on printed circuit antennas," *IEEE Trans. Antennas Propagat.*, vol. AP-32, pp. 807–814, Aug. 1984.

[28] W. Wertgen and R.H. Jansen, "Spectral iterative techniques for the full-wave 3-D analysis of (M)MIC structure," in *IEEE MTT-S Int. Microwave Symp. Dig.*, June 1988, pp. 709–712.

[29] P. B. Katehi and N. G. Alexopoulos, "Real axis integration of Sommerfeld integrals with applications to printed circuit antennas," *J. Math. Phys.*, vol. 24, no. 3, Mar. 1983.

William P. Harokopus, Jr. (S'87–M'87) was born in Detroit, MI, on February 10, 1963. He received the B.S. (1985) and M.S. (1986) degrees in electrical engineering from the University of Michigan, Ann Arbor. He is currently pursuing the Ph.D. degree at Michigan, where he works in the Radiation Lab as a graduate research assistant. His dissertation will be on the high-frequency characterization of microstrip discontinuities.

Pisti B. Katehi (S'81–M'84–SM'89) received the B.S.E.E. degree from the National Technical University of Athens, Greece, in 1977 and the M.S.E.E. and Ph.D. degrees from the University of California, Los Angeles, in 1981 and 1984 respectively.

In September 1984 she joined the faculty of the EECS Department of the University of Michigan, Ann Arbor, as an Assistant Professor. Since then, she has been involved in the modeling and computer-aided design of millimeter-wave and near-millimeter-wave monolithic circuits and antennas.

In 1984 Dr. Katehi received the W. P. King Award and in 1985 the S. A. Schelkunoff Award from the Antennas and Propagation Society. In 1987 she received an NSF Presidential Young Investigator Award and a Young Scientist Fellowship awarded from URSI. Dr. Katehi is a member of IEEE AP-S, MTT-S and Sigma Xi.

APPENDIX C

Surface Wave Excitation from Open Microstrip Discontinuities

W.P. Harokopus, P.B. Katehi, W. Ali-Ahmad and G.M. Rebeiz

Surface Wave Excitation from Open Microstrip Discontinuities

Submitted to IEEE Transactions on Microwave Theory and Techniques

W. P. Harokopus, Jr. and P. B. Katehi[1]
W. Ali-Ahmad and G. M. Rebeiz [2]
The Radiation Laboratory
Electrical Engineering and Computer Science Department
1301 Beal Ave.
University of Michigan, Ann Arbor MI., 48109
(313) 747-1796

Abstract-Radiation properties of open microstrip discontinuities are investigated using a fullwave integral equation technique. The total radiation loss of bends and stubs has been separated into the individual contributions of space and surface wave excitation. With the inclusion of radiation loss, the analysis is well-suited for the study of elements frequently utilized in monolithic arrays. Patterns depicting the power propagating in the substrate have been computed and verified experimentally.

[1]W. P. Harokopus and P. B. Katehi performed the theoretical analysis
[2]W. Ali-Ahmad and G. M. Rebeiz performed the experimental analysis

List of Figures

of low-loss microstrip elements. For example, it is well known that the shape of discontinuities can be altered to improve circuit performance (eg. mitered bend, radial stub). However, finding the influence of these and similar modifications on the radiation loss is also important. This analysis will provide the necessary quantitative results for determining when and why a specific circuit modification decreases radiation loss.

The analysis presented quantifies the radiation occuring from each mechanism, and shows the directions of propagation of surface wave radiation. These far-field patterns are useful for determining where coupling through surface wave excitation may be strong. In addition, results will be shown demonstrating the strong influence that substrate composition has on radiation properties.

The far-field patterns are obtained in this paper by the complex transformation of the space domain Green's function to the steepest descent plane, where a saddle point integration is performed. The contribution from the saddle point represents far-field spherical wave power in the half-space above the dielectric. In addition, the residues corresponding to poles captured in the contour deformation represent cylindrical surface waves guided in the dielectric. Theoretical and experimental results are presented for microstrip stubs and bends that detail the effect of radiation on circuit performance, quantify the types of radiation which are occuring, and show the direction and intensity of surface wave propagation in the substrate.

2 Theory

2.1 Computation of Current Distribution

A cross-section of the microstrip structure is shown in Figure 1. The conductors are lossless and their thickness is much smaller than a wavelength. The substrate is of thickness h and is assumed lossless. The electric field may be written in terms of the space domain integral equation

$$\bar{E}(x,y,z) = \int\int_{S'} [k_i^2 \bar{\bar{I}} + \bar{\nabla}\bar{\nabla}] \cdot \bar{\bar{G}}(x,y,z/x',y',z') \cdot \bar{J}(s')ds' \qquad i = 0,1 \quad (1)$$

with k_0 and k_1 being the wave numbers in free-space and dielectric regions respectively, and where

$$\bar{J}(s') = J_x(x',y')\hat{x} + J_y(x',y')\hat{y} \quad (2)$$

is the current on the conducting strips. The components of the dyadic Green's function [29]]

$$\bar{\bar{G}}(x,y,z/x',y',z') = G_{xx}\hat{x}\hat{x} + G_{zx}\hat{z}\hat{x} + G_{yy}\hat{y}\hat{y} + G_{zy}\hat{z}\hat{y} \quad (3)$$

are represented by Sommerfeld integrals, given in Appendix A.

The microstrip discontinuity is subdivided into rectangles, and the method of moments is applied with roof-top basis functions. These basis functions are consistent with the current boundary conditions; having piecewise sinusoidal variation in the longitudinal direction and constant variation in the transverse direction.

With the application of Galerkin's method, the integral equation is reduced into a matrix equation

$$\left[Z \right] \left[I \right] = \left[V \right]$$

where Z represents the impedance matrix, I is the vector of unknown x and y current amplitudes, and V is the excitation vector which reflects the position of the source. The matrix inversion is performed providing the current amplitudes on the discontinuity and the feeding lines. The microstrip structure is excited by infinitesimal gap generators. More details on the excitation and application of the method of moments may be obtained in [21].

2.2 Far-Field Radiation

The electromagnetic fields generated by the microstrip element may be computed from the integral equation once the microstrip current is known. As shown in figure 2(a), the original path of integration was along the positive real axis. Along this path, a finite number of singularities corresponding to excited surface waves are encountered between the free space (k_0) and the dielectric (k) wavenumbers. In the method of moments procedure, this integration was performed exactly by a combination of numerical and analytical techniques [34]. To obtain the radiated far-fields, the integral is transformed to the steepest descent plane by the complex mapping

$$\lambda = k_0 \sin \alpha. \tag{4}$$

Figure 2(b) shows the new path of integration in the α-plane. The quantaties shown in the parenthesis correspond to the points mapped from the λ-plane to the α-plane. The poles now lie along the line defined by $\mathrm{Re}(\alpha) = \pi/2$, between the points $\mathrm{Im}(\alpha) = 0$ and $\mathrm{Im}(\alpha) = \nu_k$. ν_k is mapped from the point k in the λ-plane

according to

$$k = k_0 \sin(\pi/2 + j\nu_k) \tag{5}$$

$$\nu_k = \cosh^{-1}(\epsilon_r). \tag{6}$$

Asymptotic approximations are made for the Hankel functions as shown in appendix B. The contour of integration (Figure 2(b)) is then deformed into the steepest descent path[31]. A saddle point integration is performed, with the saddle point equal to the spherical observation angle ($\alpha = \theta$). During the contour deformation, a finite number of surface wave simple pole singularities are captured as shown. These will be discussed in the following section.

To obtain the fields for a microstrip discontinuity, one returns to the electric field integral equation. In the far-field, the electric field can be written in spherical coordinates as

$$E_\theta = k_0^2[\pi_\theta^x + \pi_\theta^y] \tag{7}$$

$$E_\phi = k_0^2[\pi_\phi^x + \pi_\phi^y] \tag{8}$$

with

$$\begin{aligned}
\pi_\theta^x &= \int\int_{S'}[G_{xx}\cos(\theta)\cos(\phi) - G_{zx}\sin(\theta)]J_x(x',y')dx'dy' \\
\pi_\theta^y &= \int\int_{S'}[G_{yy}\cos(\theta)\sin(\phi) - G_{zy}\sin(\theta)]J_y(x',y')dx'dy' \\
\pi_\phi^x &= \int\int_{S'}[-G_{xx}\sin(\phi)]J_x(x',y')dx'dy' \\
\pi_\phi^y &= \int\int_{S'}[G_{yy}\cos(\phi)]J_y(x',y')dx'dy'
\end{aligned} \tag{9}$$

Inserting the results of the saddle point analysis (Appendix B) and the values of the microstrip current obtained from the method of moments, the electric field

can be written in the form

$$E_\theta = \frac{j\omega\mu_o}{2\pi}k_0^2\frac{e^{(-jk_0R)}}{k_0R}[\frac{F(\theta)}{f_1(\theta,h)}\cos(\theta) - \frac{jG(\theta)(1-\epsilon_r)}{f_1(\theta,h)f_2(\theta,h)}\sin(\theta)]$$
$$[A_{rx}(\theta,\phi)\cos(\phi) + A_{ry}(\theta,\phi)\sin(\phi)]$$
$$E_\phi = -\frac{j\omega\mu_o}{2\pi}k_0^2\frac{e^{(-jk_0R)}}{k_0R}\frac{F(\theta)}{f_1(\theta,h)}[A_{rx}(\theta,\phi)\sin(\phi) - A_{ry}(\theta,\phi)\cos(\phi)]$$

where the terms $A_{rx}(\theta,\phi)$ and $A_{ry}(\theta,\phi)$ contain the spatial integrations of the basis functions with the Green's function phase terms. These integrations are performed analytically and result in the expressions given below

$$A_{rx}(\theta,\phi) = 4e^{(jK_0\frac{l}{2}\sin(\theta)\sin(\phi))}[\sum_{n=1}^{N+1}\sum_{m=1}^{M+1}I_{nm}^x e^{(jy_mK_0\sin(\theta)\sin(\phi))}e^{(jx_nK_0\sin(\theta)\cos(\phi))}]$$
$$\frac{\sin(K_0\frac{l}{2}\sin(\theta)\sin(\phi))}{K_0\sin(\theta)\sin(\phi)}\frac{\cos(lK_0\sin(\theta)\cos(\phi)) - \cos(k_sl)}{K_s\sin(K_sl)[1-\frac{K_0}{k_s}^2\sin(\theta)^2\cos(\phi)^2]} \quad (10)$$

$$A_{ry}(\theta,\phi) = 4e^{(jK_0\frac{l}{2}\sin(\theta)\cos(\phi))}[\sum_{n=1}^{N+1}\sum_{m=1}^{M+1}I_{nm}^y e^{(jy_mK_0\sin(\theta)\sin(\phi))}e^{(jx_nK_0\sin(\theta)\sin(\phi))}]$$
$$\frac{\sin(K_0\frac{l}{2}\sin(\theta)\cos(\phi))}{K_0\sin(\theta)\cos(\phi)}\frac{\cos(lK_0\sin(\theta)\sin(\phi)) - \cos(k_sl)}{K_s\sin(K_sl)[1-\frac{K_0}{k_s}^2\sin(\theta)^2\sin(\phi)^2]} \quad (11)$$

where the quantaties l and k_s represent the subsection length and scaling constant for the basis functions, respectively. More detailed information on the rooftop basis functions is available in [21]. The fields depend, therefore, on two factors: A substrate contribution, resulting from the Green's function and containing all the information about the substrate; and a shaping contribution, resulting from the spatial dependence of the source and containing all the information about the shape and current distribution over the conducting strips. Consequently, these two factors may be handled independently to reduce loss.

The total far-field space wave power is obtained by integrating the poynting

vector over a hemisphere centered around the discontinuity.

$$P_r^{sp} = \frac{1}{2}\int_0^{2\pi}\int_0^{\frac{\pi}{2}}\left[\frac{E_\theta^2}{\eta_0} + \frac{E_\phi^2}{\eta_0}\right] r\sin(\theta)d\theta d\phi \tag{12}$$

2.3 Surface Waves

During the contour deformation of the previous section, a finite number of singularities were captured as shown in figure 2. These singularities correspond to excited surface wave modes that fall into two types: a) Tranverse Electric (TE_z), or b) Tranverse Magnetic (TM_z) to the dielectric-air interface. The poles are determined by the zeroes of two analytic functions present in the denominator of the Green's function given by

$$f_1(\alpha) = -\cos(\alpha)\sin(k_0 h\sqrt{\epsilon_r - \sin(\alpha)^2}) + j\sqrt{\epsilon_r - \sin(\alpha)^2}\cos(k_0 h\sqrt{\epsilon_r - \sin(\alpha)^2}) \tag{13}$$

for (TE_z) waves, and

$$f_2(\alpha) = -\sqrt{\epsilon_r - \sin(\alpha)^2}\sin(k_0 h\sqrt{\epsilon_r - \sin(\alpha)^2}) + j\epsilon_r\cos(\alpha)\cos(k_0 h\sqrt{\epsilon_r - \sin(\alpha)^2}) \tag{14}$$

for (TM_z) waves. It is now a simple matter to obtain field patterns in the dielectric ($\theta = \pi/2$) by the application of Cauchy's residue theorem. The total number of poles is determined by the operating frequency and the substrate parameters. The pole locations are given by

$$\alpha_{TM} = \frac{\pi}{2} + j\nu_n \quad n = 1, N_{TM} \tag{15}$$

$$\alpha_{TE} = \frac{\pi}{2} + j\nu_m \quad m = 1, N_{TE} \tag{16}$$

where N_{TM} and N_{TE} are the number of excited TM and TE modes, respectively. The far-fields are determined by computing the residues of the singularities and are given in Appendix C.

The power in a particular mode is found from the poynting vector. The surface wave power at the dielectric interface is given by

$$P_r^{TM}(\phi) = \sum_{n=0}^{NTM} \frac{k_0^2 \omega \mu_0}{4\pi} \frac{[\epsilon_r - cosh^2(\nu_n)]cosh^2(\nu_n)sinh^2(\nu_n)}{|f_2'(\alpha)|^2|_{\pi/2+j\nu_n}} (\sin(k_0 h\sqrt{\epsilon_r - \sin(\alpha)^2}))^2 \\ |\cos(\phi)A_{rx}(\phi) + \sin(\phi)A_{ry}(\phi)|^2 \quad (17)$$

for TM waves, and

$$P_r^{TE}(\phi) = \sum_{m=0}^{NTE} \frac{k_0^2 \omega \mu_0}{4\pi} \frac{cosh^2(\nu_m)sinh^2(\nu_m)}{|f_1'(\alpha)|^2|_{\pi/2+j\nu_m}} (\sin(k_0 h\sqrt{\epsilon_r - \sin(\alpha)^2}))^2 \\ |\sin(\phi)A_{rx}(\phi) + \cos(\phi)A_{ry}(\phi)|^2 \quad (18)$$

for TE waves. In equations (17) and (18) the terms $A_{rx}(\phi)$ and $A_{ry}(\phi)$ are given by equations (10) and (11), with the quantity $k_0 \cosh(\nu_n)$ replacing $k_0 \sin(\theta)$.

The total power in TM and TE modes may be found by integrating the poynting vector over a cylindrical surface centered at the discontinuity

$$P_r^{TM} = -\int_{-h}^{\infty}\int_0^{2\pi} \frac{E_z \cdot H_\phi^*}{2} \rho d\phi dz \quad (19)$$

$$P_r^{TE} = \int_{-h}^{\infty}\int_0^{2\pi} \frac{E_\phi \cdot H_z^*}{2} \rho d\phi dz. \quad (20)$$

3 Results

In the following sections, examples of total radiation loss and surface wave far-field patterns will be presented for microstrip open-end, radial stub, and bend discontinuities. As mentioned, these surface wave patterns are useful for determining directions of strong coupling between adjacent discontinuities. Space wave

far-field patterns have a null along the dielectric substrate, except under very rare circumstances (at the cutoff of higher order surface wave modes), which are not applicable to the presented results. Furthermore, surface wave radiation is in the form of cylindrical waves which decay less rapidly with distance than spherical space waves. It is therefore reasonable to conclude that surface waves play a major role in undesirable electromagnetic interference. In addition, the extraction of the exact amount of both types of radiation will help in the design of low-loss elements and extend the use of microstrip circuitry farther into the millimeter wave region. The first of the following sections will give examples of total surface and space wave losses; the second section includes examples which depict the direction of surface wave propagation.

3.1 Space and Surface Wave Radiation Losses

3.1.1 Stubs

In Figure 3, examples of open-ended and radial microstrip stubs are shown. These elements are frequently utilized in matching networks. The radial stub is generally utilized for its greater bandwidth. In Figure 4, the contributions of space and surface waves to total radiation loss is given for the open-ended stub. In the lower frequency range, the space wave contribution is slightly larger. However, the surface wave loss increases sharply with frequency, overtaking the space wave power at 20 GHz. Beyond 20 GHz, the total radiation loss increases sharply due to a corresponding increase in surface wave loss. The total radiation loss approaches half of the input power at 34 GHz. This is a significant amount of loss for an element on a substrate with practical electrical dimensions for (M)MIC

applications.

Radiation loss for the radial stub, shown in Figure 5, exhibits a similar behavior to the open-ended stub, except that the sharp increase in surface wave and total radiated power is shifted upward. This behavior results in less radiation loss in the 20-30 GHz range of operation, but greater loss above 30 GHz. The lowest order TE_0 mode activates between 35 and 36 GHz, therefore, only one surface wave mode is excited in this example. The loss is expected to continue to increase until the first higher order mode is excited, and then it will oscillate as reported in [32]. Although the shape of the metallization has a strong influence on the total loss, it does not appear to have a greater influence on either type at lower frequencies as shown in Figure 6. However, above 30 Ghz the radial stub radiates a higher percentage of power into the excited surface wave mode.

3.1.2 Mitered bend

Chamfering of microstrip bends is a common practice for the reduction of input VSWR. The example shown in Figure 7 clearly illustrates that mitering can result in lower radiation loss as well. The losses between the mitered and right-angle bend are effectively equal until 20 GHz ($h = .127\lambda_g$). Beyond this frequency, the right-angle bend clearly radiates more power. Figure 8 shows that, once again, the radiation is dominated by surface waves at high frequencies. However, the mitering produces a reduction in both space and surface wave power as illustrated in Figure 9, where both the mitered and unmitered cases exhibit identical percentages of surface wave loss. As shown in the inset to Figure 7, the reflected power is much smaller for the mitered case over the entire frequency range. This improvement

results from a decrease in both the excess reactance and the radiation resistance at the bend. Therefore, mitering effectively increases the useful range of operation of the bend element. A similar discontinuity printed on a lower permittivity substrate would exhibit lower, but still significant, surface wave losses.

3.2 Surface Wave Patterns

The preceeding analysis was utilized to obtain patterns in the substrate for the TM_0 surface wave mode. As previously mentioned, this mode is excited at any operating frequency. Accordingly, it is important to know the direction and amount of propagating power. Theoretical and experimental patterns were obtained at 10 GHz for microstrip stub and bend discontinuities printed on a 96 mil duroid ($\epsilon_r = 2.3$) substrate. The duroid substrates were machined into 5 inch diameter circular sections whose edges were gradually tapered as shown in Figure 10, to minimize the reflection of the surface wave at the edge of the substrate. The microstrip element, in this case a radial stub, was etched from the copper metallization on the top face of the substrate. The experimental setup is shown in Figure 11. The substrates were elevated onto a rotating pedestal and surrounded by absorber to minimize multiple reflections. Each element was fed at the edge of the substrate with a 10 GHz signal and a resonant dipole was positioned near the edge to measure the pattern. The pedestal was then rotated to alter the observation angle (ϕ). Absorber was placed over the microstrip launcher to minimize extraneous radiation.

3.2.1 Open-Ended Line

The experimental results for a 100 ohm (W=100 mil) open-ended line was compared to the theoretical results derived by the previously presented method. Initially, the theoretical model assumed that the discontinuity was fed by a semi-infinite line, to remove the radiation effects of the finite line length and isolate the radiation of the open-end. Figure 12 shows that the theoretical results agree well with the experimental results. The open-ended line radiates power in the TM_0 surface wave along the longitudinal axis of the line. The experimental results include the effect of finite line length as demonstrated by the side-lobes in the pattern. To verify the presence of these lobes, the theoretical results were re-computed considering the finite length of line as utilized in the experiment. The new theoretical results and experimental data were now in excellent agreement(Figure 14). Also note that the beamwidth of the surface wave pattern became narrower.

3.2.2 Radial Stub

The TM_0 surface wave pattern of the previously shown radial stub was measured. The 350 mil radial portion swept out an angle of 90 degrees and was fed by a 100 ohm microstrip line. Radial stubs are useful as broader band elements in (M)MIC design. Figure 14 shows the theoretical results for semi-infinite and finite length lines, as compared to experiment. The results are very similar to those obtained for the open-ended line, with the surface wave power excited along the longitudinal axis.

3.2.3 Bend Discontinuity

A two-port right-angle bend discontinuity, shown in Figure 15, was fabricated and measured. Experimentally, port 2 was left open-ended at a distance of two free space wavelengths from the bend discontinuity. The theoretical model assumed a semi-infinite feed line (shown as $\phi = 0$ direction in picture), and that the second port was left open-ended, but extended far from the discontinuity. This extension maintains the standing wave ratio on the line, but removes the effects of the open end and finite line lengths; thus, isolating the effect of the bend. Shown in Figure 16, the agreement between theory and experiment is good. The experimental results show the the combined effects of finite line length and the open-end. This results in the mild dis-agreement between the theory and experiment around 45 degrees. The side-lobe present at 90 degrees in both the theoretical and experimental results comes from the power reflected at the open-end which returns to the bend and radiates there. This lobe would be smaller if the second port were matched.

4 Conclusion

Simple formulas have been presented to characterize power loss from open microstrip discontinuities. The technique utilizes microstrip current distributions obtained with the method of moments. The formulas allow the separation of total loss into the individual contributions of space wave and surface wave radiation, and indicate which direction surface wave power is propagating within the substrate. Results presented show that on high density substrates, high frequency

radiation loss is dominated by the TM_0 surface wave. This mode is excited along the longitudinal axis of the stub and bend discontinuities shown, and may have a narrow beamwidth. An example of a mitered bend was shown to radiate less power than its right-angle counterpart. Such a minor topology change had a significant influence on total radiated power, without having a more significant impact on either of the two types. This is reflected in an equal percentage reduction in both space and surface wave radiation. It is known, from published work on microstrip antennas, that the substrate structure plays an important role in the surface wave radiation. Therefore, an element showing improved loss performance on a single layer, such as the mitered bend, will show further improvement when printed on a multiple layer substrate designed to have lower substrate losses.

Acknowledgements

This research was sponsered by the National Science Foundation (Contract No. ECS-8602536).

Appendix A

The components of the space domain green's function are given by

$$G_{xx} = G_{yy} = -\frac{j\omega\mu_0}{2\pi k_0^2}\int_0^\infty J_0(\lambda\rho)\frac{\sinh uh}{f_1(\lambda,h)}e^{-u_0 z}\lambda d\lambda \quad Z>0 \tag{21}$$

$$G_{zx} = \tan(\phi)G_{zy} = -\frac{j\omega\mu_0}{2\pi k_0^2}(1-\epsilon_r)\cos\phi\int_0^\infty J_1(\lambda\rho)e^{-u_0 z}\frac{\sinh uh\cosh uh}{f_1(\lambda,h)f_2(\lambda,h)}\lambda^2 d\lambda \quad Z>0$$

$$G_{xx} = G_{yy} = -\frac{j\omega\mu_0}{2\pi k^2}\int_0^\infty J_0(\lambda\rho)\frac{\sinh u(z+h)}{f_1(\lambda,h)}\lambda d\lambda \quad Z<0$$

$$G_{zx} = \tan(\phi)G_{zy} = -\frac{j\omega\mu_0}{2\pi k^2}(1-\epsilon_r)\cos\phi\int_0^\infty J_1(\lambda\rho)\frac{\sinh uh\cosh u(z+h)}{f_1(\lambda,h)f_2(\lambda,h)}\lambda^2 d\lambda \quad Z<0$$

with $\rho = \sqrt{(x-x')^2+(y-y')^2}$, $u_0 = \sqrt{\lambda^2-k_0^2}$, and $u_1 = \sqrt{\lambda^2-k_1^2}$. The equations $f_1(\lambda,h)$ and $f_2(\lambda,h)$ represent characterisic equations for surface wave modes given by

$$f_1(\lambda,h) = u_0\sinh uh + u\cosh uh \tag{22}$$

$$f_2(\lambda,h) = \epsilon_r u_0\cosh uh + u\sinh uh \tag{23}$$

where in the above, ϵ_{r1} is the relative dielectric constant, and h is the thickness of the substrate. These components of the Green's function may be tranformed from semi-infinite to infinite integrations through the relationships

$$J_0(\lambda\rho) = \frac{1}{2}[H_0^{(1)}(\lambda\rho) + H_0^{(2)}(\lambda\rho)] \tag{24}$$

$$J_1(\lambda\rho) = \frac{1}{2}[H_1^{(1)}(\lambda\rho) + H_1^{(2)}(\lambda\rho)] \tag{25}$$

$$H_0^{(2)}(\lambda\rho) = -H_0^{(1)}(-\lambda\rho) \tag{26}$$

$$H_1^{(2)}(\lambda\rho) = H_1^{(1)}(-\lambda\rho) \tag{27}$$

Resulting in the expressions in the free-space region ($z > 0$)

$$G_{xx} = G_{yy} = -\frac{j\omega\mu_o}{4\pi k_0^2}\int_{-\infty}^\infty H_0^{(1)}(\lambda\rho)e^{-u_0 z}\frac{\sinh uh}{f_1(\lambda,h)}\lambda d\lambda \tag{28}$$

$$G_{zx} = \tan\phi G_{zy} = -\frac{j\omega\mu_o}{4\pi k_0^2}(1-\epsilon_r)\cos\phi\int_{-\infty}^\infty H_1^{(1)}(\lambda\rho)e^{-u_0 z}\frac{\sinh uh\cosh uh}{f_1(\lambda,h)f_2(\lambda,h)}\lambda^2 d\lambda \tag{29}$$

Appendix B

To find the far-field patterns above the dielectric, the components of the of the Green's function are more appropriately given in spherical coordinates according to

$$\rho = r\sin\theta \tag{30}$$

$$z = r\cos\theta \tag{31}$$

After substitution of (30) and (31) into (28) and (29), the form of the Green's function becomes

$$\begin{aligned} G_{xx} = G_{yy} &= -\frac{j\omega\mu_o}{4\pi k_0^2}\int_{-\infty}^{\infty} H_0^{(1)}(rk_0\sin(\theta)\sin(\alpha))e^{-jk_0r\cos(\theta)\cos(\alpha)} \\ &\quad \frac{j\sin(k_0h\sqrt{\epsilon_r-\sin(\alpha)^2})}{f_1(\alpha)}k_0^2\cos(\alpha)\sin(\alpha)d\alpha \\ G_{zx} = \tan\phi G_{zy} &= -\frac{j\omega\mu_o}{4\pi k_0^2}(1-\epsilon_r)\cos(\phi)\int_{-\infty}^{\infty} H_1^{(1)}(rk_0\sin(\theta)\sin(\alpha))e^{-jk_0r\cos(\theta)\cos(\alpha)} \\ &\quad \frac{j\sin(k_0h\sqrt{\epsilon_r-\sin(\alpha)^2})\cos(k_0h\sqrt{\epsilon_r-\sin(\alpha)^2})}{f_1(\alpha)f_2(\alpha)}k_0^3\cos(\alpha)\sin(\alpha)^2d\alpha \end{aligned} \tag{32}$$

Where the surface wave characteristic equations become

$$f_1(\alpha) = -k_0\cos(\alpha)\sin(k_0h\sqrt{\epsilon_r-\sin(\alpha)^2}) + jk_0\sqrt{\epsilon_r-\sin(\alpha)^2}\cos(k_0h\sqrt{\epsilon_r-\sin(\alpha)^2}) \tag{33}$$

for TE surface waves and

$$f_2(\alpha) = -k_0\sqrt{\epsilon_r-\sin(\alpha)^2}\sin(k_0h\sqrt{\epsilon_r-\sin(\alpha)^2}) + jk_0\epsilon_r\cos(\alpha)\cos(k_0h\sqrt{\epsilon_r-\sin(\alpha)^2}) \tag{34}$$

for TM surface waves. Far-field patterns($rk_0 >> 1$) are desired. Under this condition, the Hankel functions may be replaced by their respective large argument approximations

$$H_0^{(1)}(rk_0\sin(\theta)\sin(\alpha)) = \sqrt{\frac{2j}{\pi rk_0}}\frac{e^{-jrk_0\sin(\theta)\sin(\alpha)}}{\sqrt{\sin(\theta)\sin(\alpha)}} \tag{35}$$

$$H_1^{(1)}(rk_0\sin(\theta)\sin(\alpha)) = \sqrt{\frac{2j}{\pi rk_0}}\frac{je^{-jrk_0\sin(\theta)\sin(\alpha)}}{\sqrt{\sin(\theta)\sin(\alpha)}} \tag{36}$$

resulting in the final expressions

$$G_{xx} = G_{yy} = -\frac{j\omega\mu_o}{4\pi}\sqrt{\frac{2j}{\pi rk_0}}\int_{-\infty}^{\infty}\frac{jF(\alpha)}{f_1(\alpha)}e^{-jk_0r\cos(\theta-\alpha)}d\alpha \tag{37}$$

$$G_{zx} = \tan\phi G_{zy} = -\frac{j\omega\mu_o}{4\pi}\sqrt{\frac{2j}{\pi r k_0}}(1-\epsilon_r)\cos(\phi)\int_{-\infty}^{\infty}\frac{G(\alpha)e^{-jk_0 r\cos(\theta-\alpha)}}{f_1(\alpha)f_2(\alpha)}d\alpha \tag{38}$$

with

$$F(\alpha) = \frac{\sin(\alpha)\cos(\alpha)}{\sqrt{\sin(\theta)\sin(\alpha)}}j\sin(k_0 h\sqrt{\epsilon_r - \sin(\alpha)^2}) \tag{39}$$

$$G(\alpha) = -\frac{\sin(\alpha)^2\cos(\alpha)}{\sqrt{\sin(\theta)\sin(\alpha)}}\sin(k_0 h\sqrt{\epsilon_r - \sin(\alpha)^2})\cos(k_0 h\sqrt{\epsilon_r - \sin(\alpha)^2}) \tag{40}$$

The saddle point is to the observation angle ($\alpha = \theta$). The saddle point integration is performed resulting in

$$G_{xx} = \frac{j\omega\mu_o}{2\pi}\frac{e^{(-jk_0R)}}{k_0R}\frac{F(\theta)}{f_1(\theta,h)}e^{(jk_0[x'\sin(\theta)\cos(\phi)+y'\sin(\theta)\sin(\phi)])} \tag{41}$$

$$G_{zx} = \frac{j\omega\mu_o}{2\pi}(1-\epsilon_r)\cos(\phi)\frac{e^{(-jk_0R)}}{k_0R}\frac{jG(\theta)}{f_1(\theta,h)f_2(\theta,h)} \tag{42}$$
$$e^{(jk_0[x'\sin(\theta)\cos(\phi)+y'\sin(\theta)\sin(\phi)])}$$

These expressions give the far-field patterns above the substrate (space wave patterns). They are spherical waves as seen by their spatial dependence $\frac{e^{(-jk_0R)}}{k_0R}$. In the phase terms of the above expressions $R = r + (x'\sin(\theta)\cos(\phi) + y'\sin(\theta)\sin(\phi))$, and the amplitude terms $\frac{1}{r}$ have been replaced by $\frac{1}{R}$.

Appendix C

Surface wave fields resulting from application of Cauchy's theroem.

$$E_z = \frac{k_0\omega\mu_0}{2}\sqrt{\frac{2j}{\pi\rho k_0}}\cos(\phi)\sum_{n=0}^{NTM}\frac{\sqrt{\epsilon_r - cosh^2(\nu_n)}}{\sqrt{\cosh\nu_n}}\frac{\cosh^2(\nu_n)\sinh(\nu_n)}{[f_2'(\alpha,h)]|_{\frac{\pi}{2}+j\nu_n}} \tag{43}$$
$$\sin[k_0\sqrt{\epsilon_r - cosh^2(\nu_n)}h]e^{-jk_0\rho\cosh(\nu_n)}e^{-k_0 z\sinh(\nu_n)} \qquad Z > 0$$

$$H_\phi = -\frac{k_0^2}{2}\sqrt{\frac{2j}{\pi\rho k_0}}\cos(\phi)\sum_{n=0}^{NTM}\frac{\sqrt{\epsilon_r - cosh^2(\nu_n)}}{\sqrt{\cosh\nu_n}}\frac{\cosh(\nu_n)\sinh(\nu_n)}{[f_2'(\alpha,h)]|_{\frac{\pi}{2}+j\nu_n}} \tag{44}$$

$$H_\phi = -\frac{k_0^2}{2}\sqrt{\frac{2j}{\pi\rho k_0}}\cos(\phi)\sum_{n=0}^{NTM}\frac{\sqrt{\epsilon_r - cosh^2(\nu_n)}}{\sqrt{\cosh\nu_n}}\frac{\cosh(\nu_n)\sinh(\nu_n)}{[f_2'(\alpha,h)]|_{\frac{\pi}{2}+j\nu_n}} \tag{44}$$
$$\sin[k_0\sqrt{\epsilon_r - cosh^2(\nu_n)}h]e^{-jk_0\rho\cosh(\nu_n)}e^{-k_0 z\sinh(\nu_n)} \qquad Z > 0$$

$$E_z = \frac{k_0\omega\mu_0}{2}\sqrt{\frac{2j}{\pi\rho k_0}}\cos(\phi)\sum_{n=0}^{NTM}\frac{\cosh^2(\nu_n)\sinh^2(\nu_n)}{\sqrt{\cosh\nu_n}}e^{-jk_0\rho\cosh(\nu_n)} \tag{45}$$
$$\frac{\cos[k_0\sqrt{\epsilon_r - cosh^2(\nu_n)}(z+h)]}{[f_2'(\alpha,h)]|_{\frac{\pi}{2}+j\nu_n}} \qquad Z < 0$$

$$H_\phi = -\frac{\epsilon_{r1}k_0^2}{2}\sqrt{\frac{2j}{\pi\rho k_0}}\cos(\phi)\sum_{n=0}^{NTM}\frac{\cosh(\nu_n)\sinh^2(\nu_n)}{\sqrt{\cosh\nu_n}}e^{-jk_0\rho\cosh(\nu_n)} \tag{46}$$
$$\frac{\cos[k_0\sqrt{\epsilon_r - cosh^2(\nu_n)}(z+h)]}{[f_2'(\alpha,h)]|_{\frac{\pi}{2}+j\nu_n}} \quad Z<0$$

and for the TE case

$$H_z = -\frac{k_0^2}{2}\sqrt{\frac{2j}{\pi\rho k_0}}\sin(\phi)\sum_{m=0}^{NTE}\frac{cosh^2(\nu_m)sinh(\nu_m)}{\sqrt{\cosh\nu_m}[f_1'(\alpha,h)]|_{\frac{\pi}{2}+j\nu_m}} \tag{47}$$
$$\sin[k_0\sqrt{\epsilon_r - cosh^2(\nu_n)}h]e^{-jk_0\rho\cosh(\nu_m)}e^{-k_0 z\sinh(\nu_m)} \quad Z>0$$

$$E_\phi = -\frac{k_0\omega\mu_0}{2}\sqrt{\frac{2j}{\pi\rho k_0}}\sin(\phi)\sum_{m=0}^{NTE}\frac{cosh(\nu_m)sinh(\nu_m)}{\sqrt{\cosh\nu_m}[f_1'(\alpha,h)]|_{\frac{\pi}{2}+j\nu_m}} \tag{48}$$
$$\sin[k_0\sqrt{\epsilon_r - cosh^2(\nu_n)}h]e^{-jk_0\rho\cosh(\nu_m)}e^{-k_0 z\sinh(\nu_m)}$$

$$H_z = -\frac{k_0^2}{2}\sqrt{\frac{2j}{\pi\rho k_0}}\sin(\phi)\sum_{m=0}^{NTE}\frac{cosh^2(\nu_m)sinh(\nu_m)}{\sqrt{\cosh\nu_m}[f_1'(\alpha,h)]|_{\frac{\pi}{2}+j\nu_m}} \tag{49}$$
$$e^{-jk_0\rho\cosh(\nu_m)}\sin[k_0\sqrt{\epsilon_r - cosh^2(\nu_n)}(z+h)] \quad Z<0$$

$$E_\phi = -\frac{k_0\omega\mu_0}{2}\sqrt{\frac{2j}{\pi\rho k_0}}\sin(\phi)\sum_{m=0}^{NTE}\frac{cosh(\nu_m)sinh(\nu_m)}{\sqrt{\cosh\nu_m}[f_1'(\alpha,h)]|_{\frac{\pi}{2}+j\nu_m}} \tag{50}$$
$$e^{-jk_0\rho\cosh(\nu_m)}\sin[k_0\sqrt{\epsilon_r - cosh^2(\nu_n)}(z+h)] \quad Z<0$$

References

[1] M. Maeda, "Analysis of Gap in Microstrip Transmission Lines", *IEEE Trans. Microwave Theory Tech.*, Vol. MTT-20, pp.390-396, Jun. 1972.

[2] P. Benedek and P. Silvester, "Equivalent Capacitance of Microstrip Gaps and Steps", *IEEE Trans. Microwave Theory Tech.*, Vol. MTT-20, pp.729-733, Nov. 1972.

[3] P. Silvester and P. Benedek, "Equivalent Capacitance of Microstrip Open Circuits," *IEEE Trans. Microwave Theory Tech.*, Vol. MTT-20, pp. 511-516, Aug. 1972.

[4] P. Silvester and P. Benedek, "Equivalent discontinuities capacitances for Right-Angle Bends, T-junctions, and Crossings," *IEEE Trans. Microwave Theory Tech.*, Vol. MTT-21, pp. 341-346, May 1973.

[5] R. Horton, "The Electrical Characterization of a Right-Angle Bends in Microstrip Line," *IEEE Trans. Microwave Theory Tech.*, Vol. MTT-21, pp.427-429, Jun. 1973.

[6] T. Itoh, "Analysis of Microstrip resonators", *IEEE Trans. Microwave Theory Tech.*, Vol. MTT-22, pp.946-952, Nov. 1974.

[7] I. Wolff, G. Kompa, and R. Mehran, "Calculation Method For Microstrip Discontinuities and T-Junctions," *Electron. Lett.*, Vol. 8, 1972.

[8] G. Kompa, and R. Mehran, "Planar Waveguide Model For Calculating Microstrip Components," *Electron. Lett.*, Vol. 11, 1975.

[9] W. Menzel and I. Wolff, "A Method For Calculating the frequency Dependent Properties

[9] W. Menzel and I. Wolff, "A Method For Calculating the frequency Dependent Properties

of Microstrip Discontinuities," *IEEE Trans. Microwave Theory Tech.*, Vol. MTT-25, pp. 107-112, Feb. 1977.

[10] A. Sommerfeld, Partial Differential Equations in Physics, New York, N.Y., Academic Press, 1949.

[11] M. Kirschning, R.H. Jansen, and H.L. Koster, "Measurement and Computer-Aided Modeling of Microstrip Discontinuities by an Improved Resonator Method, 1983 "IEEE MTT-S International Microwave Symposium Digest", May, 1983.

[12] P.B. Katehi and N. G. Alexopoulos, "On the Effect of Substrate Thickness and Permittivity and Permittivity On Printed Circuit Dipole performance," *IEEE Transactions on Antennas and Propagation*, Vol AP-31, pp. 34-38, Jan. 1983.

[13] N. G. Alexopoulos, P.B. Katehi, and D. Rutledge, "Substrate Optimization for Integrated Circuit Applications," *IEEE Trans. Microwave Theory Tech.*, Vol. MTT-31, pp. 550-557, July, 1983.

[14] P.B. Katehi and N. G. Alexopoulos, "Frequency-Dependent Characteristics of Microstrip Discontinuities in Millimeter-Wave Integrated Circuits",*IEEE Trans. Microwave Theory Tech.*, Vol. MTT-33, Oct. 85, pp. 1029-1035.

[15] J. R. Mosig, "Arbitrarily shaped microstrip structures and their analysis with a mixed potential integral equation, *IEEE Trans. Microwave Theory Tech.*, Vol. MTT-36, pp. 314-323, Feb. 1988.

[16] R. W. Jackson, and D. M. Pozar, "Full-Wave Analysis of Microstrip Open-End and Gap Discontinuities",*IEEE Trans. Microwave Theory Tech.*, Vol. MTT-33,Oct. 85, pp. 1036-1042.

[17] J. C. Rautio and R.F. Harrington, "An electromagnetic timeharmonic analysis of shielded microstrip circuits," *IEEE Trans. Microwave Theory Tech.*, Vol. MTT-35, pp. 726-730, Aug. 1987.

[18] R. H. Jansen, "The Spectral Domain Approach for Microwave Integrated Circuits," *IEEE Trans. Microwave Theory Tech.*, Vol. MTT-33, pp.1043-1056, Oct. 1985.

[19] R. Jackson, "Full-Wave Finite Element Analysis of Irregular Microstrip Discontinuities," *IEEE Trans. Microwave Theory Tech.*, Vol. MTT-37, pp. 81-89, Jan. 89.

[20] W. P. Harokopus, Jr. and P. B. Katehi, "An Accurate Characterization of Open Microstrip Discontinuities Including Radiation Losses", *IEEE Microwave Symposium Digest*, pp. 231-234, June 1989.

[21] W. P. Harokopus, Jr. and P. B. Katehi, "Characterization of Open Microstrip Discontinuities on Multilayer Substrates Including Radiation Losses", *IEEE Trans. Microwave Theory Tech.*, Vol. MTT-37, Dec. 89, pp. 1964-1972.

[22] L. P. Dunleavy and P.B. Katehi,"Shielding Effects in Microstrip Discontinuities," *IEEE Trans. Microwave Theory Tech.*, Vol. MTT-36, pp.1767-1774, Dec. 1988.

[23] "Full-wave Theory Based Development of mm-Wave Circuit Models for Microstrip Open End, Ga, Step, Bend, and Tee," *IEEE Microwave Symposium Digest*, pp. 779-782, June 1989.

[24] C.J. Railton and T. Rozzi, "Complex Modes in Boxed Microstrip," *IEEE Trans. Microwave Theory Tech.*, Vol. MTT-36, pp. 865-874, May 88.

[25] W. P. Harokopus, Jr. and P. B. Katehi, "Radiation properties of microstrip discontinuities," *IEEE Ap Digest*, June 1989.

[26] W. P. Harokopus, Jr. and P. B. Katehi, "Radiation properties of microstrip discontinuities," *1990 Radio Science Meeting Program and Abstracts*, page 337, May 1990.

[27] T. S. Horng, S. C. Wu, H. Y. Yang and N. G. Alexopoulos, "A Generalized Method for the Distinction of Radiation and Surface Wave Losses in Microstrip Discontinuities," *IEEE Microwave Symposium Digest*, pp. 1055-1058, May 1990.

[28] A. Sommerfeld, Partial Differential Equations in Physics, New York, N.Y., Academic Press, 1949.

[29] R.S. Elliott, "The Green's Function For Electric Dipoles Parallel To and Above or Within a Grounded Dielectric Slab", Hughes Technical Correspondence, 1978.

[30] R. F. Harrington, Field Computation By Moment Methods, Macmillan,N.Y. ,1968.

[31] L.B. Felsen and N. Marcuvitz, Radiation and Scattering of Waves,Prentice Hall, Englewood Cliffs, N.J. 1973.

[32] N. G. Alexopoulos, P.B. Katehi, and D. Rutledge, "Substrate Optimization for Integrated Circuit Applications," *IEEE Trans. Microwave Theory Tech.*, Vol. MTT-31, pp. 550-557, July, 1983.

[33] N.G. Alexopoulos, and D. R. Jackson, "Fundamental Superstrate (Cover) Effects on Printed Circuit Antennas," *IEEE Transactions on Antennas and Propagation*, Vol AP-32, No. 8, pp. 807-814, August 1984.

[34] P.B. Katehi and N. G. Alexopoulos, "Real Axis Integration of sommerfeld Integrals With Applications To Printed Circuit Antennas," *J. Math. Phys.*, vol. 24(3), Mar. 1983.

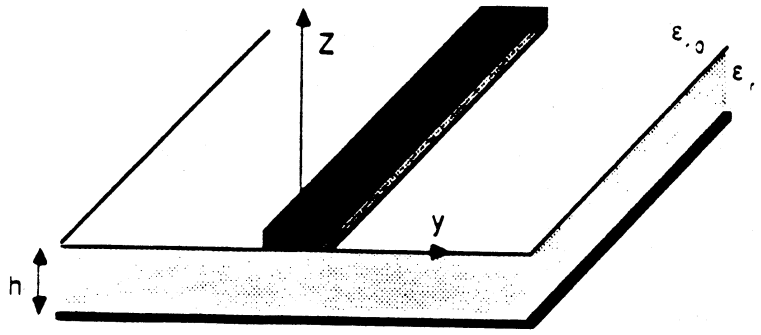

Figure 1: Open Microstrip Geometry

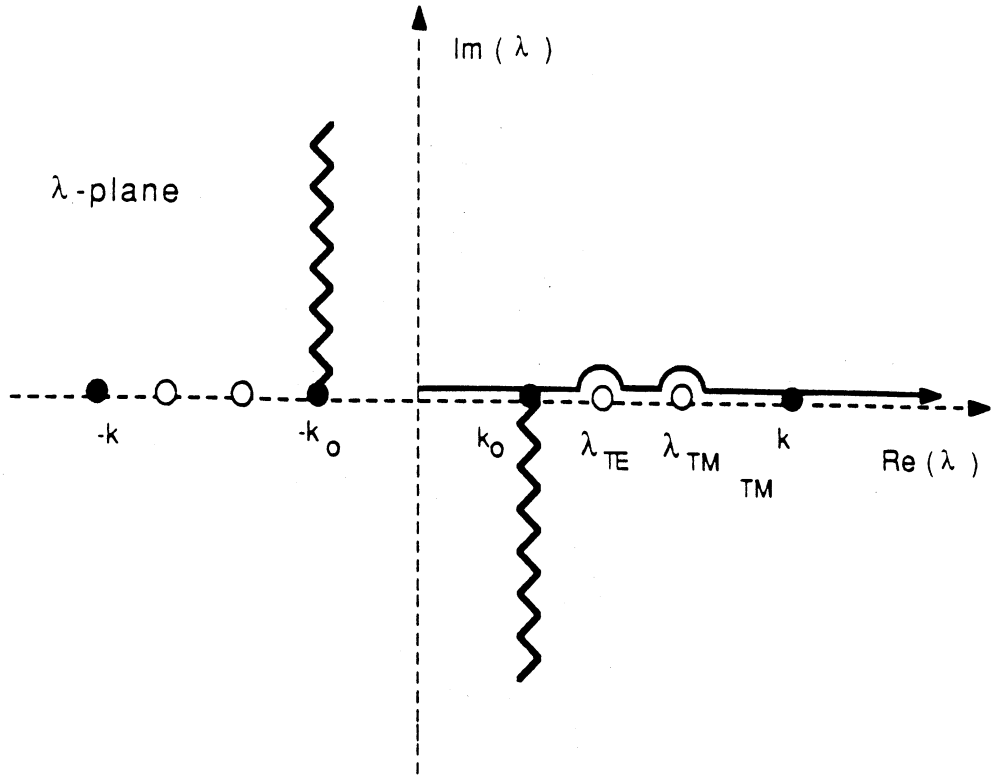

a. Integration along real axis in λ-plane

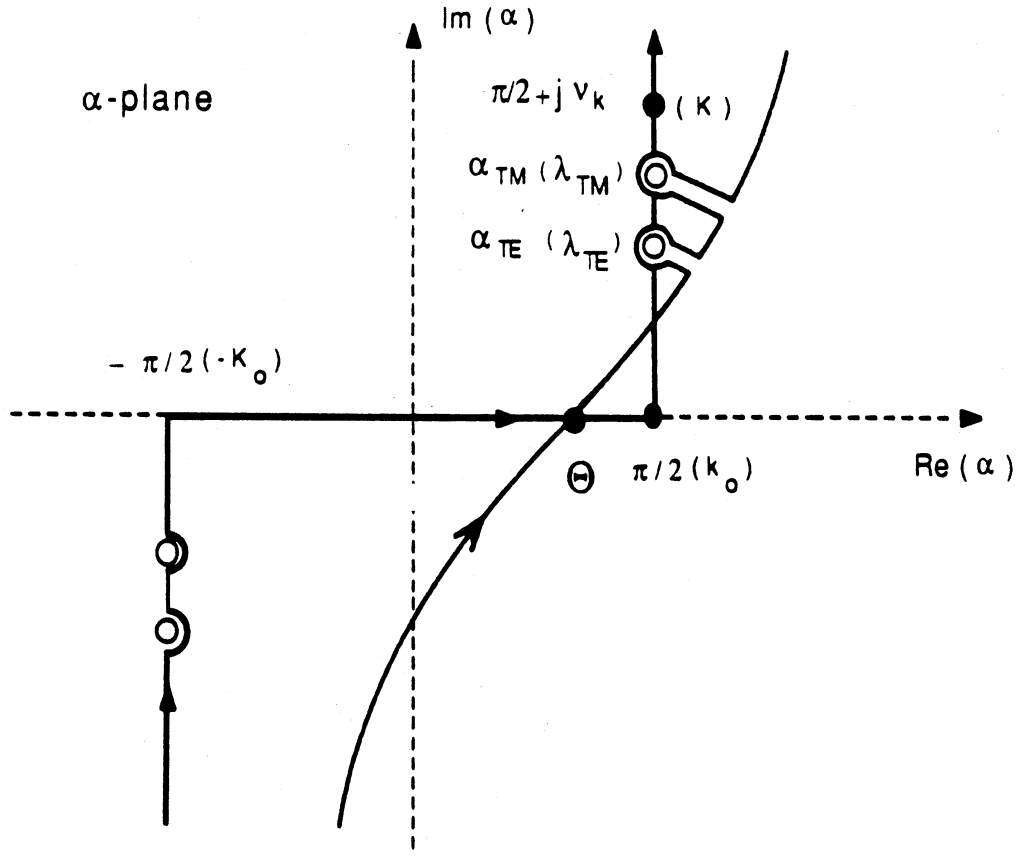

b. Contour of integration in α-plane

Figure 2: Integration Paths

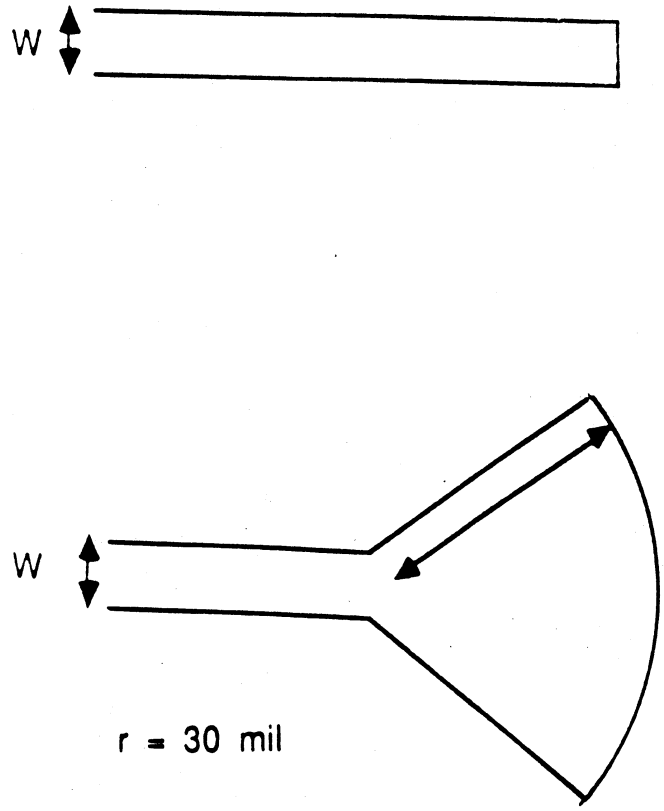

Figure 3: Microstrip Open-ended and Radial Stubs ($\epsilon_r = 12, h = 25mil, W = 10mil$)

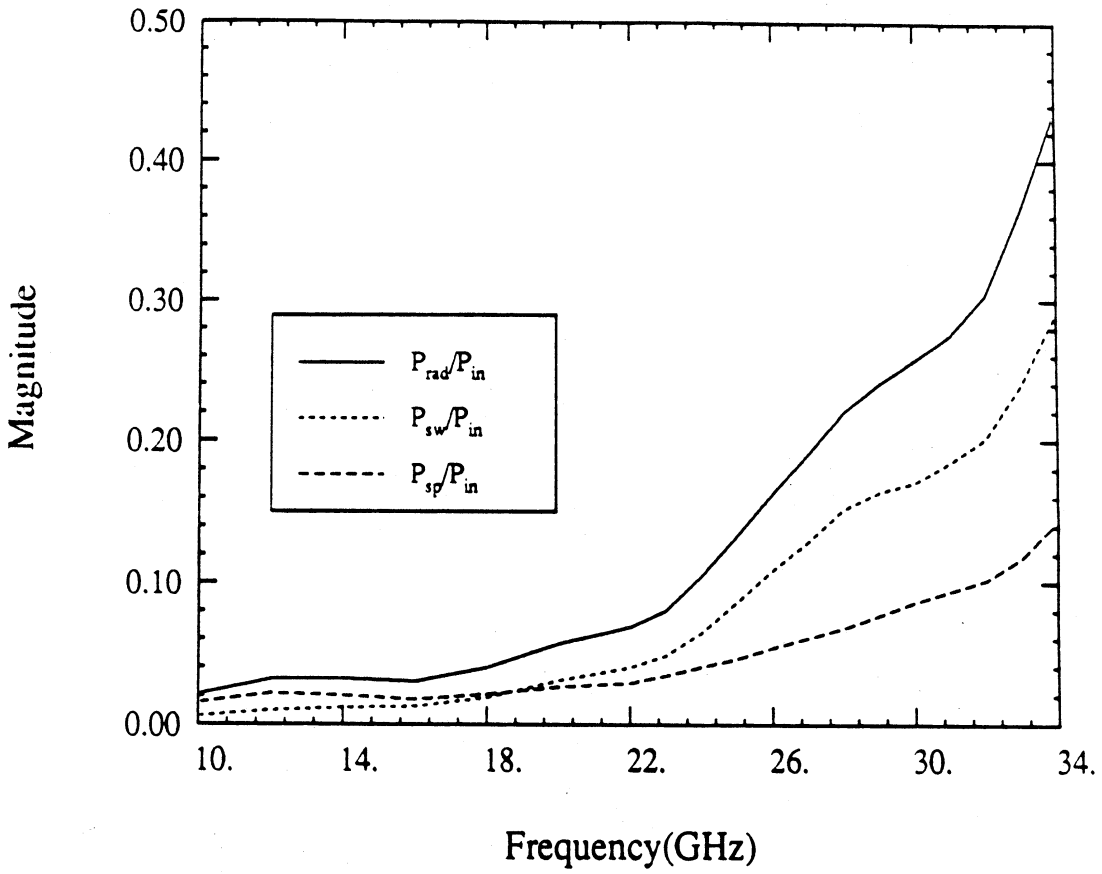

Figure 4: Radiation Loss of Open-ended Stub ($\epsilon_r = 12, h = 25mil, W = 10mil$)

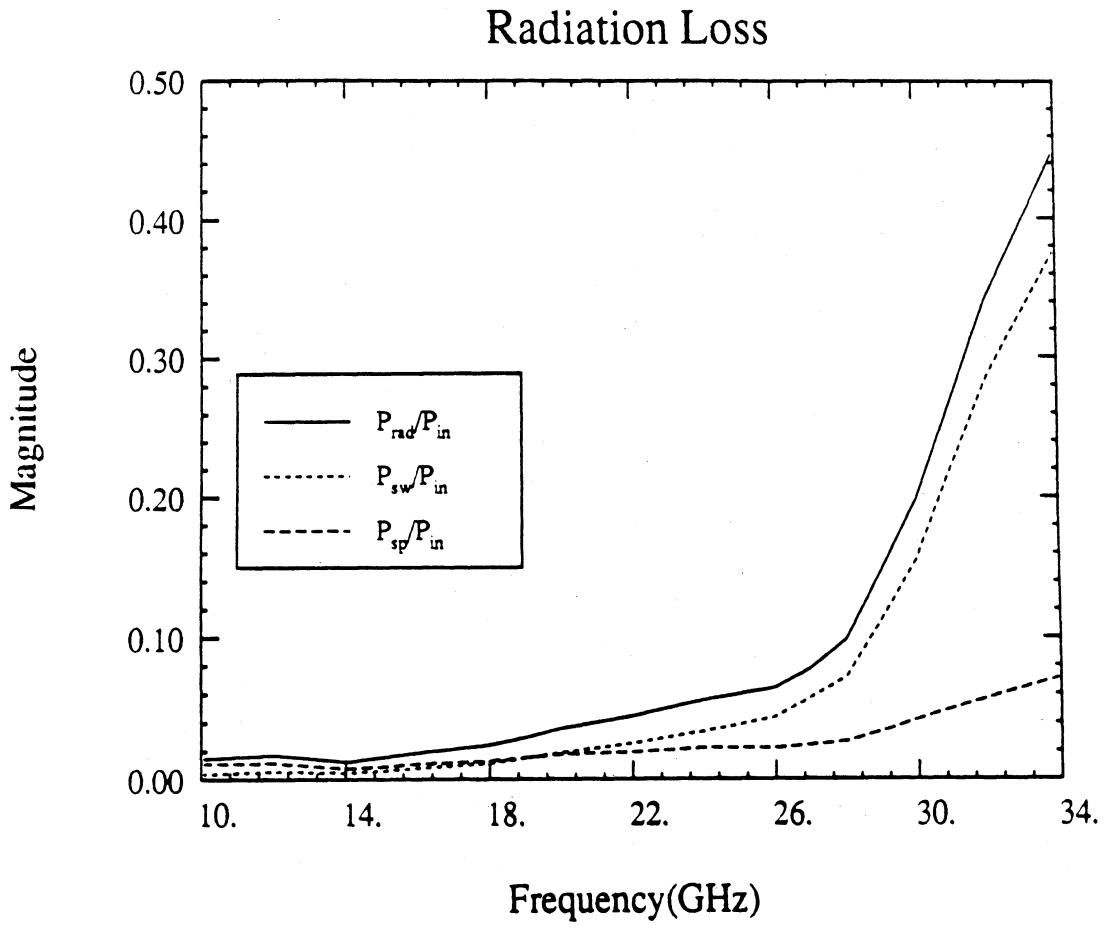

Figure 5: Radiation Loss of Radial Stub ($\epsilon_r = 12, h = 25mil, W = 10mil$)

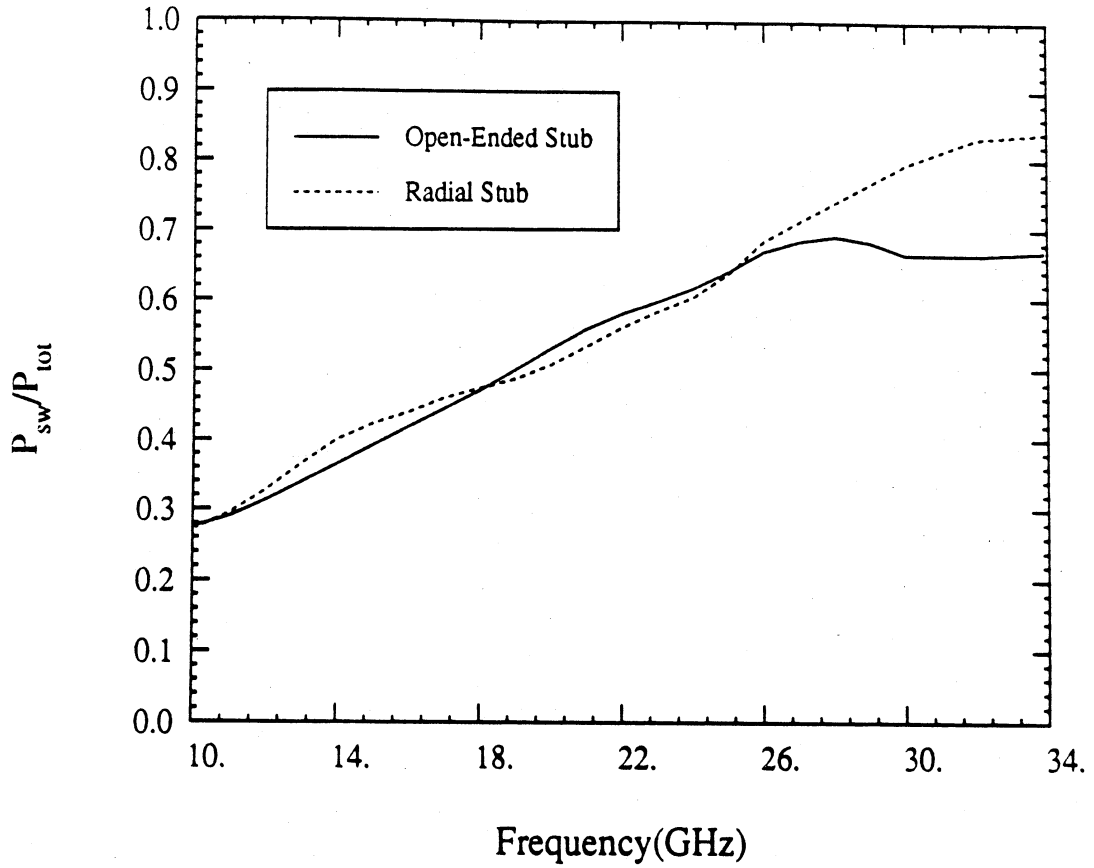

Figure 6: Percentage of Surface Wave Loss ($P_{tot} = P_{sw} + P_{sp}$) from open-ended and radial stubs ($\epsilon_r = 12, h = 25mil, W = 10mil$)

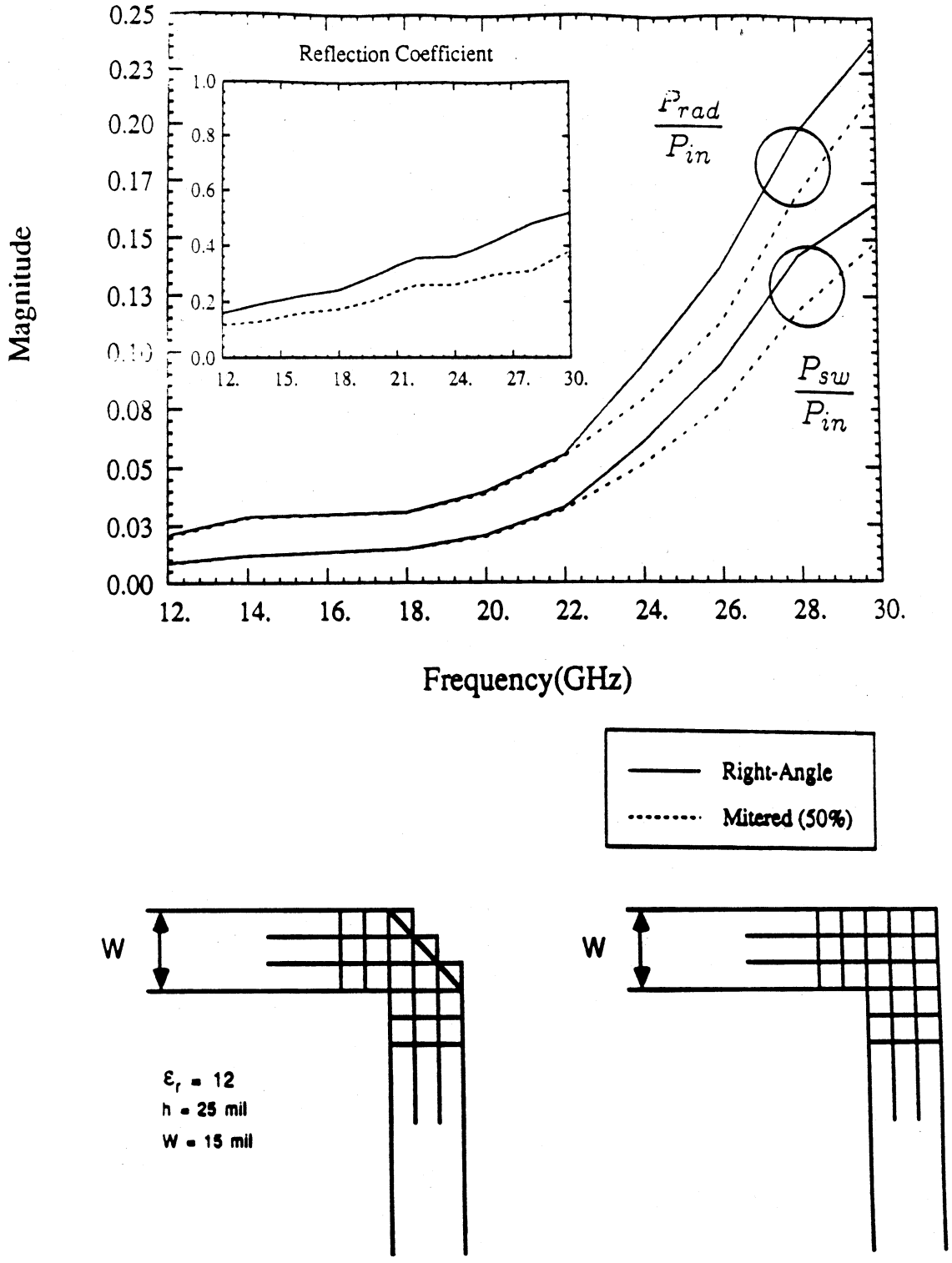

Figure 7: Total Radiation Loss of Mitered and Right-angle Bend ($\epsilon_r = 12, h = 25mil, W = 15mil$)

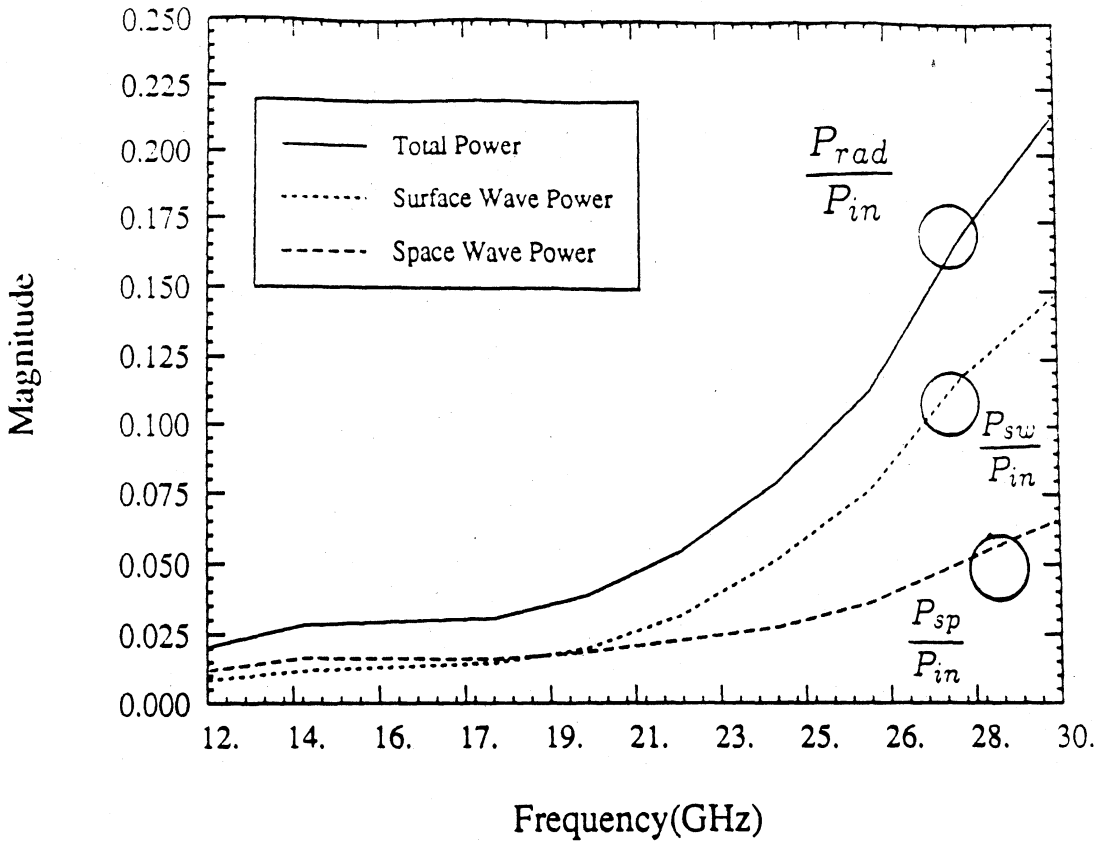

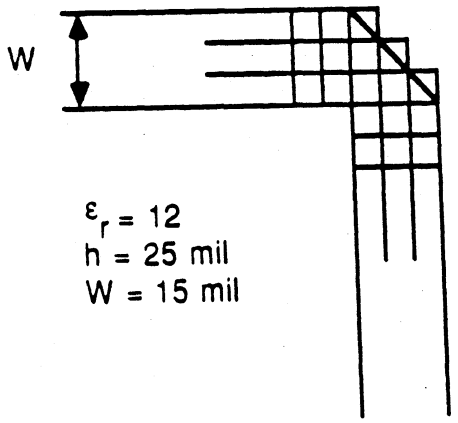

Figure 8: Radiation Loss of Mitered Bend ($\epsilon_r = 12, h = 25mil, W = 15mil$)

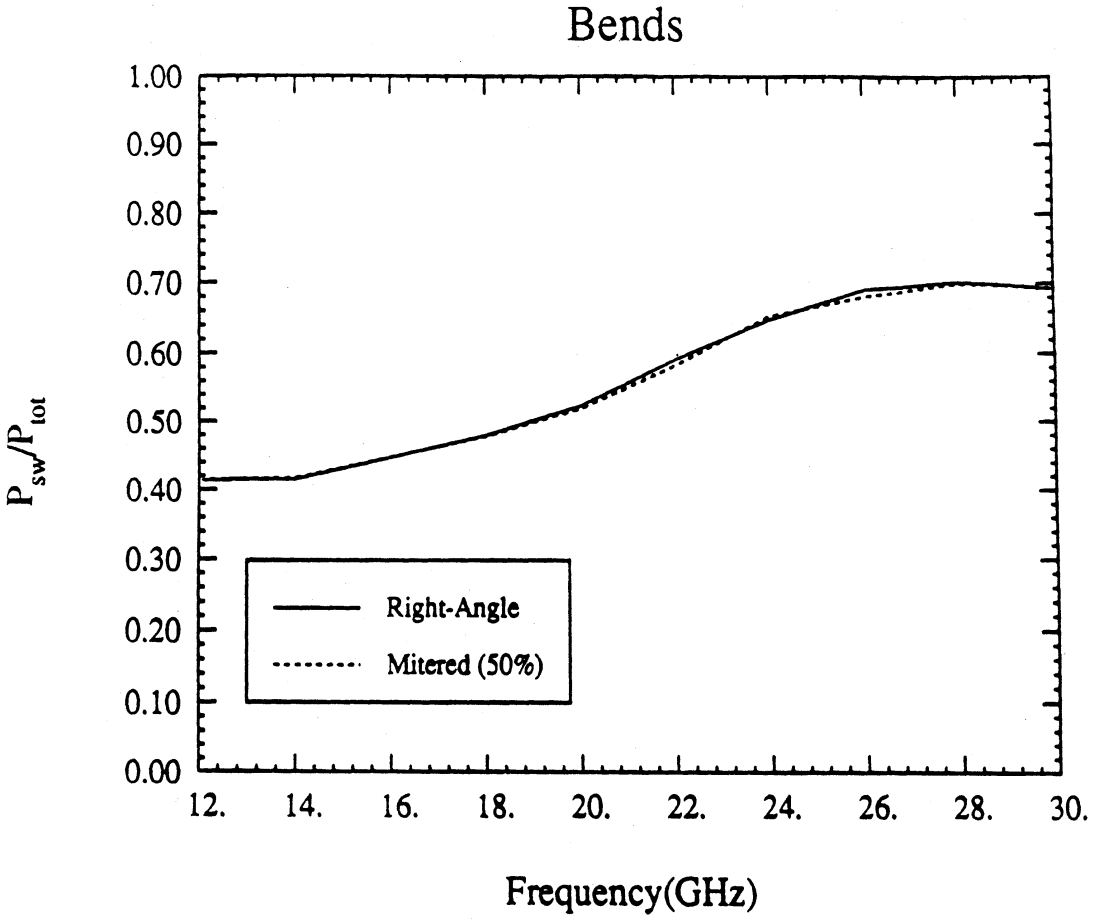

Figure 9: Percentage of Surface Wave Loss ($P_{tot} = P_{sw} + P_{sp}$) From Mitered and Right-angle Bends ($\epsilon_r = 12, h = 25mil, W = 15mil$)

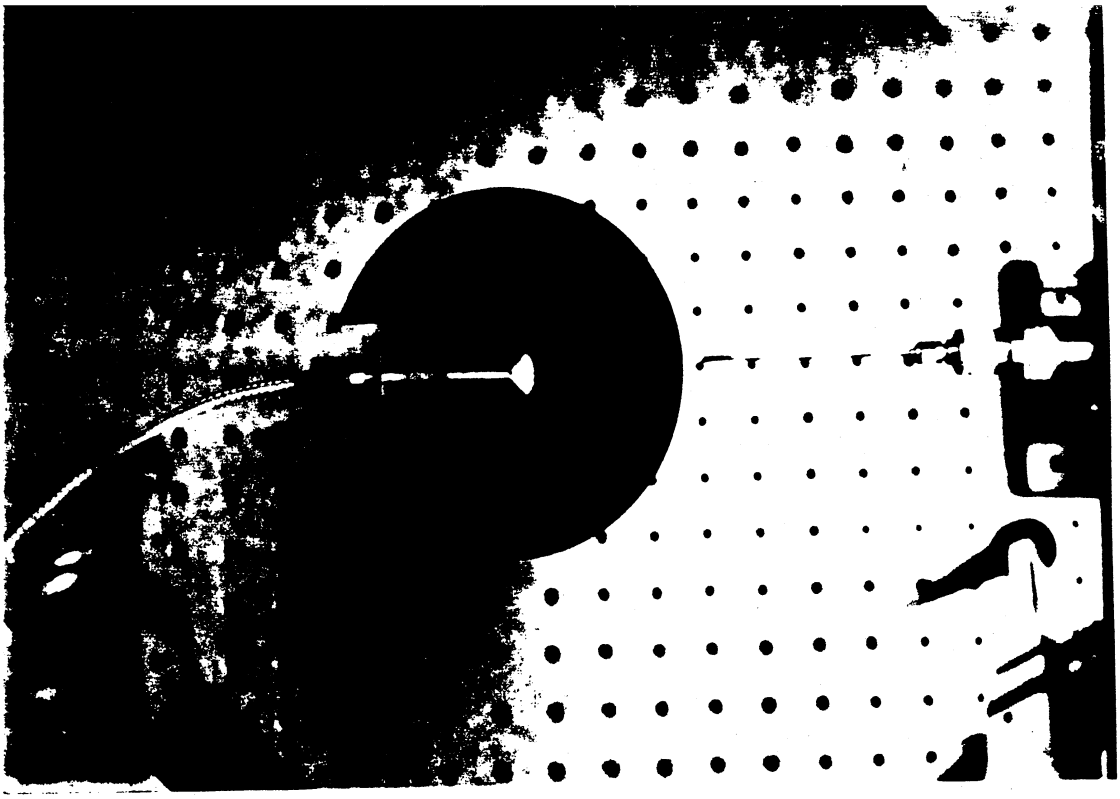

Figure 10: Microstrip Radial Stub on Printed Duroid Substarte ($\epsilon_r = 2.3, h = 95mil, W = 100mil$)

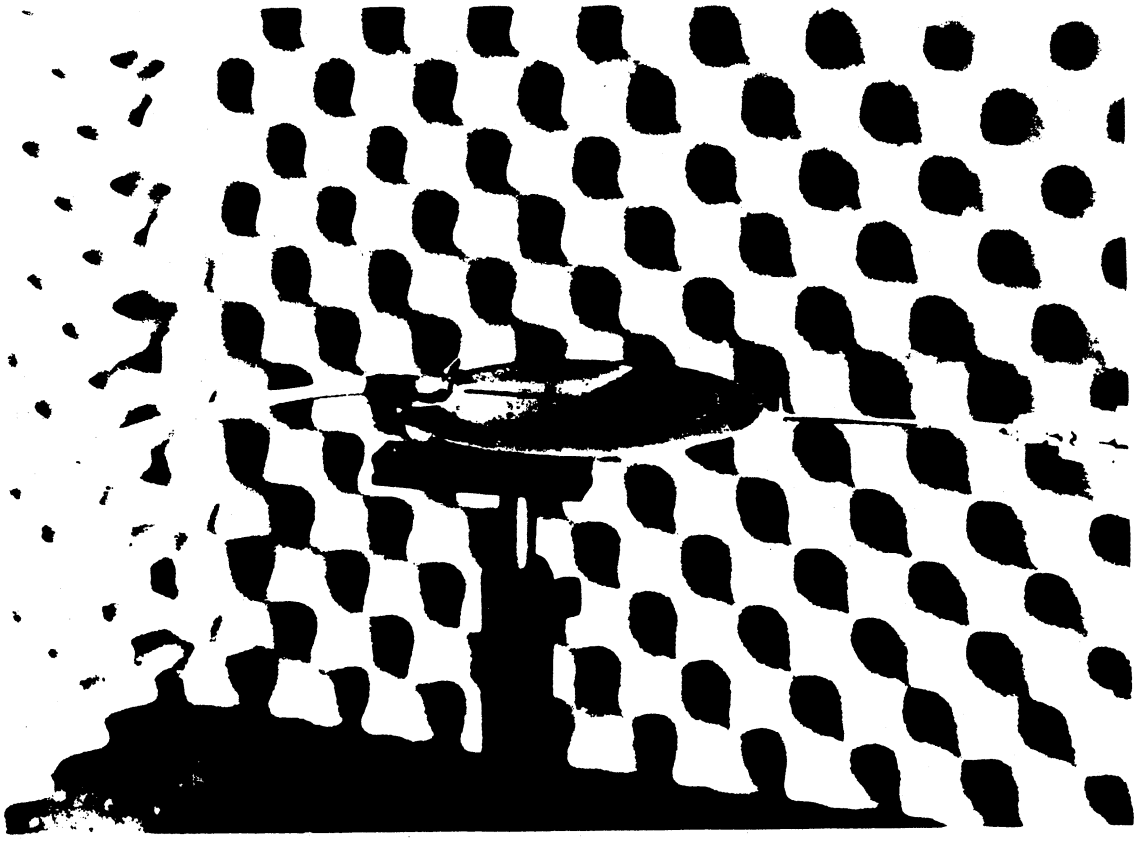

Figure 11: Experimental Setup for Surface Wave Pattern Measurements ($\epsilon_r = 2.3, h = 95mil, W = 100mil$)

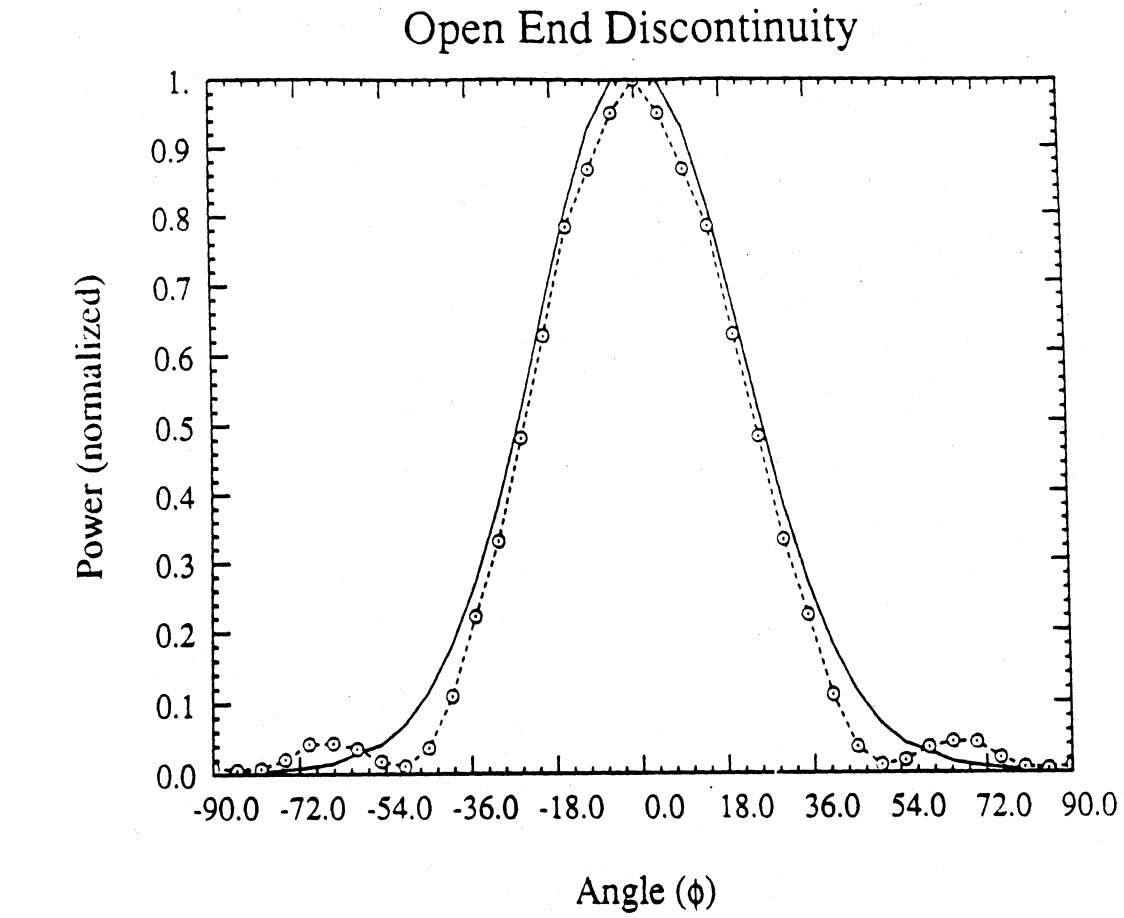

Figure 12: Surface Wave Pattern of Open-ended Line (semi-infinite feed) ($\epsilon_r = 2.3, h = 95mil, W = 100mil$)

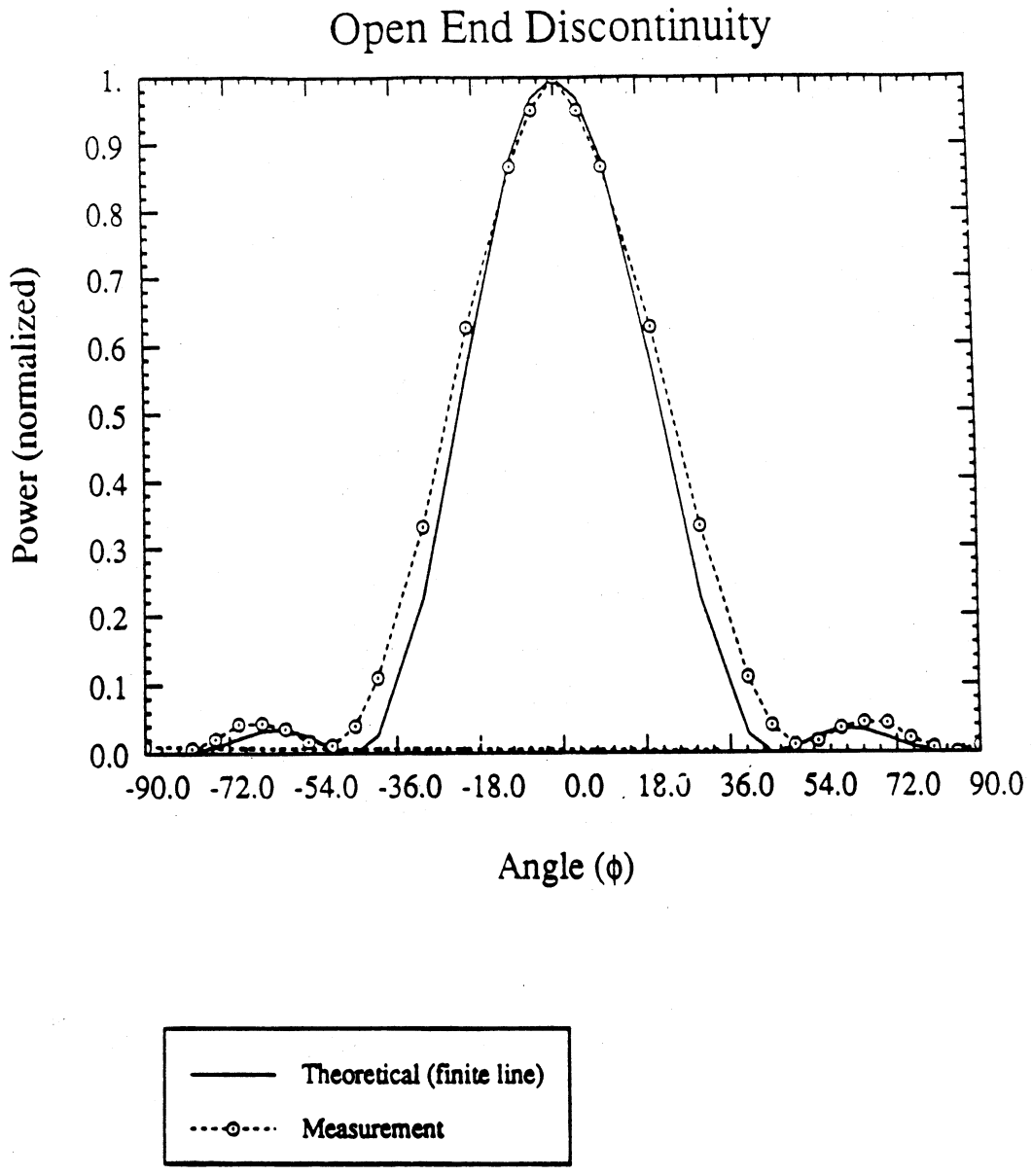

Figure 13: Surface Wave Pattern of Open-ended Line (finite feed) ($\epsilon_r = 2.3, h = 95mil, W = 100mil$)

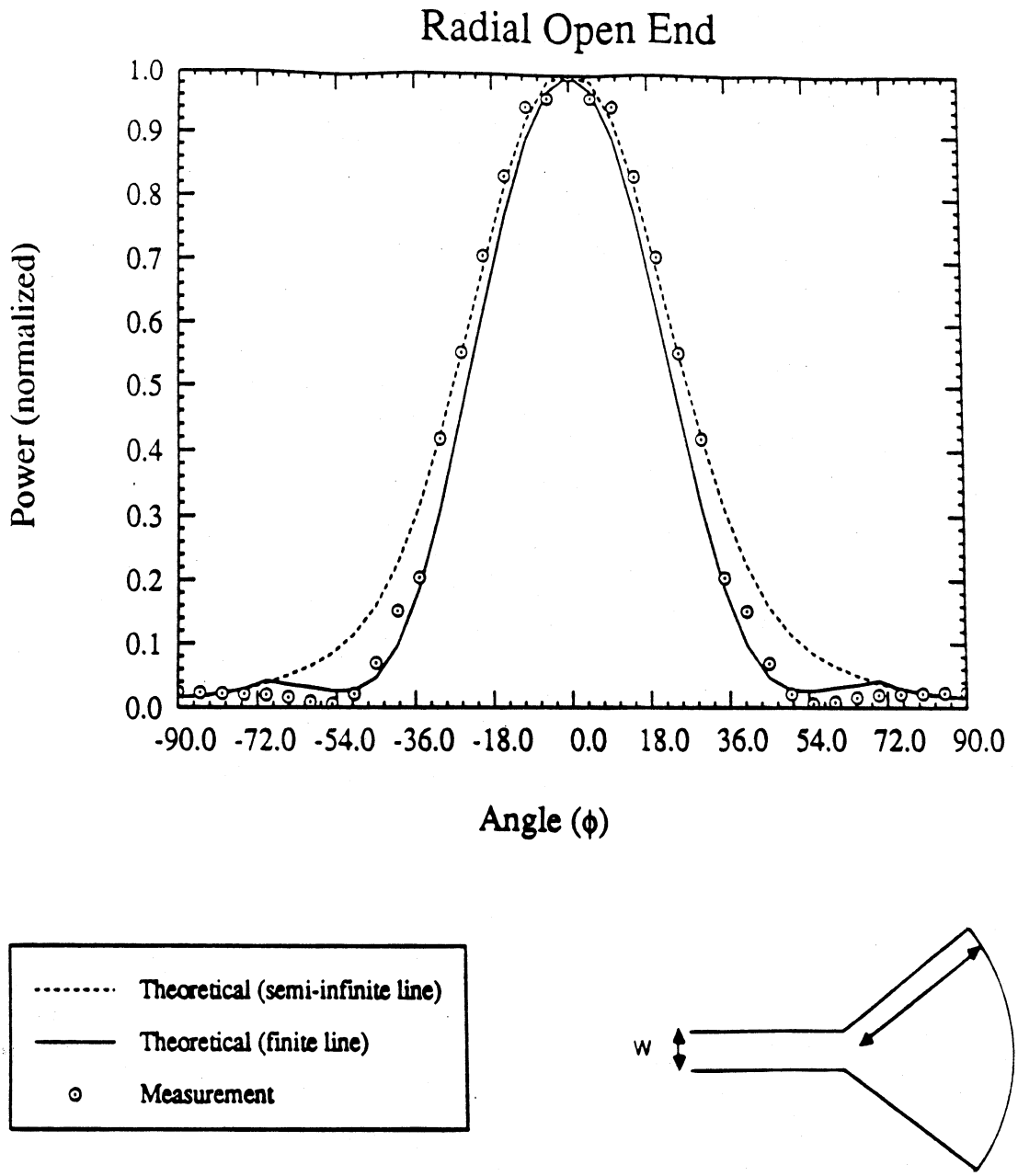

Figure 14: Surface Wave Pattern of Radial Stub ($\epsilon_r = 2.3, h = 95mil, W = 100mil, r = 300mil$)

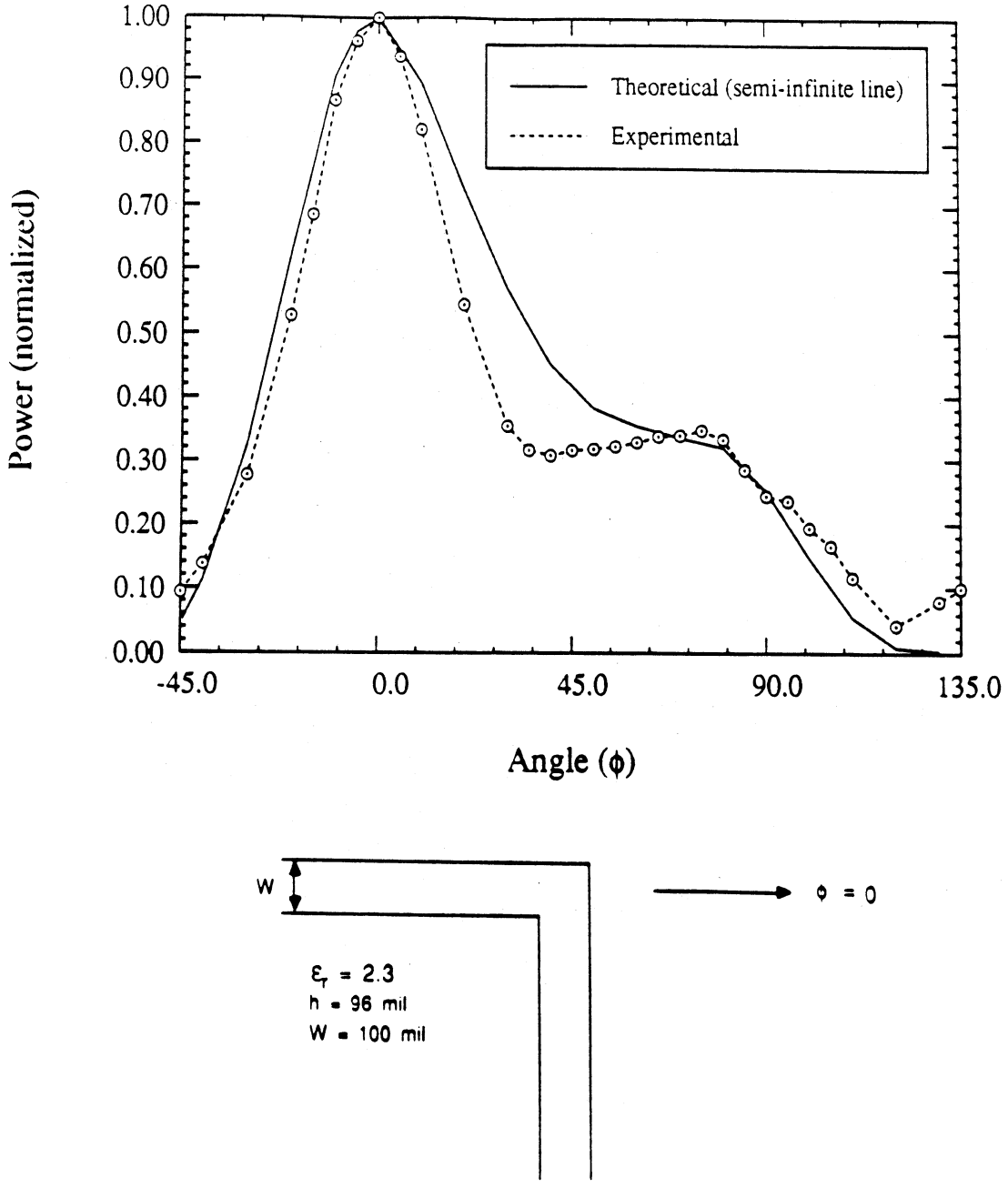

Figure 15: Surface Wave Pattern of Right-Angle Bend ($\epsilon_r = 2.3, h = 95mil, W = 100mil$)

APPENDIX D

Radiation Losses in Microstrip Antenna Feed Networks Printed on Multilayer Substrates

W.P. Harokopus and P.B. Katehi

Radiation Losses in Microstrip Antenna Feed Networks Printed on Multi-Layer Substrates

W. P. Harokopus, Jr. and P. B. Katehi

The Radiation Laboratory

Electrical Engineering and Computer Science Department

1301 Beal Ave.

University of Michigan, Ann Arbor MI., 48109

(313) 747-1796

Abstract-The effect of the substrate structure on the radiation properties of microstrip array feed networks is investigated with a space domain integral equation technique. Results for space and surface wave losses are presented for corner discontinuities printed on substrate/superstrate, and two-layer substrate structures. Comparisons are made to the single layer case.

List of Figures

1 Introduction

Vertical integration of active devices with passive radiating elements offers many advantages such as reduced area and shorter interconnect lines. Unfortunately, such integration schemes suffer for a variety of reasons including the availability of reliable models for passive circuits and radiating elements. In most monolithic array applications, the feeding structure and antenna elements are made of microstrip. Despite the advantages of the microstrip technology, radiation from discontinuities included in microstrip feed structures [1]-[7] reduce the gain of the antenna, and deteriorate the array patterns. As a result, models for these loss mechanisms on the array performance should become an important part of the array design procedure.

Microstrip arrays often have, for their protection, a cover or superstrate layer, which has also been reported to improve the gain of microstrip dipoles. This gain-enhancement technique, based on the elimination of surface waves, has been discussed extensively in the literature [8]-[9]. As mentioned in this work, total elimination of the surface waves is not practical with commercially available substrates, however, a moderate improvement in gain is realizable. Nonetheless, the presence of the superstrate, whether it is used in a planar array for improved performance or protection, must be considered carefully. In this planar configuration, the superstrate increases the substrate thickness, which, in turn, may trigger higher radiation in the feed network. These higher losses can offset the increase in array gain and further complicate the design. Furthermore, superstrates reduce the operating frequency range by lowering the cut-off frequencies of the higher order

microstrip and surface wave modes.

In this paper a fullwave method of moments technique [7] is employed to analyze the radiation properties of microstrip discontinuities often encountered in feeding networks printed on multilayer substrates. In addition, the space and surface wave contributions [10]-[13] are evaluated and it is demonstrated that the utilization of a superstrate may result in higher radiation losses and lower overall array gain.

2 Theory

Consider the open microstrip structure having a superstrate as shown in Figure 1(a) or a multi-layer substrate as shown in Figure 1(b). The conductors are lossless and their thickness (t) is much smaller than a wavelength. The substrate is of thickness h, and is also assumed lossless. The electric field may be written in terms of the current as shown below

$$\bar{E}(x,y,z) = \int\int_{S'} [k_i^2 \bar{\bar{I}} + \bar{\nabla}\bar{\nabla}] \cdot \bar{\bar{G}}_i(x,y,z/x',y',z') \cdot \bar{J}(x',y')|_{z'=0} ds' \quad (i=0,1,2) \quad (1)$$

where k_i and $\bar{\bar{G}}_i(x,y,z/x',y',z')$ are the wavenumber and dyadic Green's function in region (i), and

$$\bar{J}(x',y') = J_x(x',y')\hat{x} + J_y(x',y')\hat{y} \quad (2)$$

is the planar current on the conducting strips. The components of the dyadic Green's function used in equation (1) are expressed in terms of Sommerfeld integrals [7],[14],[15] as shown below

$$G_{\xi\xi}(x,y,z/x',y',0) = \left(\frac{\omega\mu_0}{2\pi k_0^2}\right) \int_0^\infty J_0(\lambda\rho) \mathcal{Z}_{\xi\xi}(z) \frac{\mathcal{N}_{\xi\xi}(\lambda)}{f_1(\lambda)} d\lambda \quad (3)$$

$$G_{z\xi}(x,y,z/x',y',0) = \left(\frac{\omega\mu_0}{2\pi k_0^2}\right) \Phi(\phi) \int_0^\infty J_1(\lambda\rho) \mathcal{Z}_{z\xi}(z) \frac{\mathcal{N}_{z\xi}(\lambda)}{f_1(\lambda) f_2(\lambda)} d\lambda \quad (4)$$

$$\xi = x, y$$

where

$$\rho = \sqrt{(x-x')^2 + (y-y')^2} \tag{5}$$

$$\Phi(\phi) = \begin{cases} \cos(\phi) & \xi = x \\ \sin(\phi) & \xi = y \end{cases} \tag{6}$$

and with $\mathcal{N}_{\xi\xi}(\lambda)$, $\mathcal{N}_{z\xi}(\lambda)$, $f_1(\lambda)$, and $f_2(\lambda)$ given in appendix A. In equations (3) and (4), $f_1(\lambda)$, and $f_2(\lambda)$ are analytic functions with discrete zeroes. The contributions from these zeroes give the power propogating in the substrate in the form of transverse electric (TE) and transverse magnetic (TM) surface waves, respectively.

To obtain the electric current density over the conducting strips, the method of moments is applied [16]. A rectangular region containing the microstrip discontinuity is subdivided into rectangles (see figure 2) and the current is expressed as a superposition of known basis functions multiplied by unknown coefficients.

$$J_x(x', y') = \sum_{n_x=1}^{N_x+1} \sum_{m_x=1}^{M_x+1} I^x_{nm} [f_{n_x}(x') g_{m_x}(y')] \tag{7}$$

$$J_y(x', y') = \sum_{n_y=1}^{N_y+1} \sum_{m_y=1}^{M_y+1} I^y_{nm} [f_{n_y}(y') g_{m_y}(x')] \tag{8}$$

where the pairs (n_x, m_x) and (n_y, m_y) indicate the nodes in the mesh for the X-current and Y-current, respectively. In addition, the function $f_{n_\xi}(\xi')$ gives the

longitudinal dependence of each component

$$f_{n_\xi}(\xi') = \begin{cases} \frac{\sin k_s(\xi_{n+1}-\xi')}{\sin k_s l_\xi} & \xi_{n_\xi} \le \xi' \le \xi_{n_\xi+1} \\ \frac{\sin k_s(\xi'-\xi_{n-1})}{\sin k_s l_\xi} & \xi_{n-1} \le \xi' \le \xi_{n_\xi} \\ 0 & Else \\ & (\xi,\zeta) = (x,y),(y,x) \end{cases} \tag{9}$$

while $g_{m_\xi}(\zeta')$ gives the transverse dependence

$$g_{m_\xi}(\zeta') = \begin{cases} 1 & \zeta_{m_\xi} \le \zeta' \le \zeta_{m_\xi+1} \\ 0 & Else \\ & (\xi,\zeta) = (x,y),(y,x) \end{cases} \tag{10}$$

In the above, $l_\xi = \xi_{n_\xi+1} - \xi_{n_\xi}$, and k_s is a scaling parameter chosen to vary between k_0 (free space wavenumber) and k_i (wavenumber in the highest permitivity dielectric region).

With the substitution of equations (7)-(10) into equation (1), the original integral equation can be written in the form

$$\begin{aligned} E_x + \Delta E_x &= \sum_{n_x=1}^{N_x+1}\sum_{m_x=1}^{M_x+1} I^x_{nm} \int\int_{S'} \mathcal{K}_{xx}(x,y/x',y') f_{n_x}(x') g_{m_x}(y')\, dx'dy' \\ &+ \sum_{n_y=1}^{N_y+1}\sum_{m_y=1}^{M_y+1} I^y_{nm} \int\int_{S'} \mathcal{K}_{xy}(x,y/x',y') f_{n_y}(y') g_{m_y}(x')\, dx'dy' \end{aligned} \tag{11}$$

$$\begin{aligned} E_y + \Delta E_y &= \sum_{n_x=1}^{N_x+1}\sum_{m_x=1}^{M_x+1} I^x_{nm} \int\int_{S'} \mathcal{K}_{yx}(x,y/x',y') f_{n_x}(x') g_{m_x}(y')\, dx'dy' \\ &+ \sum_{n_y=1}^{N_y+1}\sum_{m_y=1}^{M_y+1} I^y_{nm} \int\int_{S'} \mathcal{K}_{yy}(x,y/x',y') f_{n_y}(y') g_{m_y}(x')\, dx'dy' \end{aligned} \tag{12}$$

where $\mathcal{K}_{\xi\zeta}(x,y/x',y')(\xi,\zeta = x,y)$ are integro-differential operators given by

$$\mathcal{K}_{\xi\zeta}(x,y/x',y') = \int_0^\infty \left[(k_i^2 \delta_{\xi\zeta} + \frac{\partial^2}{\partial\xi\partial\zeta}) F_{\zeta\zeta} + \frac{\partial^2}{\partial z \partial \xi} F_{z\zeta} \right] d\lambda \tag{13}$$

and where $F_{\zeta\zeta}$ and $F_{z\zeta}$ are functions of λ of the following form

$$F_{\zeta\zeta} = \left(\frac{\omega\mu_0}{2\pi k_0^2}\right) J_0(\lambda\rho)\mathcal{Z}_{\zeta\zeta}(z)\frac{\mathcal{N}_{\zeta\zeta}(\lambda)}{f_1(\lambda)} \tag{14}$$

$$F_{z\zeta} = \left(\frac{\omega\mu_0}{2\pi k_0^2}\right) \Phi(\phi)J_1(\lambda\rho)\mathcal{Z}_{z\zeta}(z)\frac{\mathcal{N}_{z\zeta}(\lambda)}{f_1(\lambda)f_2(\lambda)} \tag{15}$$

In equations (11) and (12) the errors ΔE_x and ΔE_y are introduced under the approximations made for the unknown current distributions in equations (7)-(10). The z derivative in equation (13) may be replaced by an ζ derivative resulting in the modified form for the operator $\mathcal{K}_{\xi\zeta}$:

$$\mathcal{K}_{\xi\zeta}(x,y/x',y') = \int_0^\infty \left[\left(k_i^2\delta_{\xi\zeta} + \frac{\partial^2}{\partial\xi\partial\zeta}\right) f_{\zeta\zeta} + \frac{\partial^2}{\partial\xi\partial\zeta} f_{z\zeta}\right] J_0(\lambda\rho)d\lambda \tag{16}$$

$$f_{\zeta\zeta} = F_{\zeta\zeta} \tag{17}$$

$$f_{z\zeta} = -\left(\frac{\omega\mu_0}{2\pi k_0^2}\right) \mathcal{Z}'_{z\zeta}(z)\frac{\mathcal{N}_{z\zeta}(\lambda)}{\lambda f_1(\lambda)f_2(\lambda)} \tag{18}$$

where $\delta_{\xi\zeta}$ is the kronekker delta and $\mathcal{Z}'_{z\zeta}(z)$ is the first derivative of $\mathcal{Z}_{z\zeta}(z)$ with respect to z. In this manner, the first order Bessel function in equation (15) is eliminated and the ρ dependence in all Sommerfeld integrals is in the argument of a zero'th order Bessel function of the first kind.

The application of Galerkin's method for error minimization reduces equations (11) and (12) to a matrix equation

$$\left[\, Z \,\right]\left[\, I \,\right] = \left[\, V \,\right] \tag{19}$$

where Z is the impedance matrix, I is the vector of unknown x and y current amplitudes, and V is the excitation vector. The impedance matrix is a square

matrix containing four sub-matrices as shown below

$$\left[Z \right] = \begin{bmatrix} \left[Z_{xx} \right] & \left[Z_{xy} \right] \\ \left[Z_{yx} \right] & \left[Z_{yy} \right] \end{bmatrix} \tag{20}$$

The elements of each submatrix are given by

$$Z_{xx}(n,m,\nu,\mu) = \langle f_{n_x}(x')g_{m_x}(y'),\ \mathcal{K}_{xx},\ f_{\nu_x}(x)g_{\mu_x}(y)\rangle \tag{21}$$

$$Z_{xy}(n,m,\nu,\mu) = \langle f_{n_x}(x')g_{m_x}(y'),\ \mathcal{K}_{xy},\ f_{\nu_y}(y)g_{\mu_y}(x)\rangle \tag{22}$$

$$Z_{yx}(n,m,\nu,\mu) = \langle f_{n_y}(y')g_{m_y}(x'),\ \mathcal{K}_{yx},\ f_{\nu_x}(x)g_{\mu_x}(y)\rangle \tag{23}$$

$$Z_{yy}(n,m,\nu,\mu) = \langle f_{n_y}(y')g_{m_y}(x'),\ \mathcal{K}_{yy},\ f_{\nu_y}(y)g_{\mu_y}(x)\rangle \tag{24}$$

where the pair $(\nu_\xi, \mu_\xi)(\xi = x, y)$ indicates the testing points. The terms Z_{xx} and Z_{yy} are called the direct-coupled terms because the direction of the testing field and the current component are the same, while the terms Z_{xy} and Z_{yx} are the cross-coupled terms.

The double inner product in equations (21)-(24) is of the form

$$\langle f_{n_\xi} g_{m_\xi},\ \mathcal{K}_{\xi\zeta},\ f_{\nu_\zeta} g_{\mu_\zeta}\rangle = \int\int_{S'} dx'dy' \int\int_{S} dxdy\ \left(f_{n_\xi} g_{m_\xi}\ \mathcal{K}_{\xi\zeta}\ f_{\nu_\zeta} g_{\mu_\zeta} \right) \tag{25}$$

where S, and S' represent the surface of the microstrip conducting strips.

2.1 Evaluation of the Impedance Matrix

The computation of the elements in the impedance matrix requires the evaluation of quadruple spatial integrals present in equation (25), as well as the semi-infinite Sommerfeld integrals in the Green's function. The Sommerfeld integrals are computed by a real-axis integration in the complex λ-plane[17] using an extraction of the singularities technique which effectively takes into account the contribution

from the simple pole singularities of the integrand (see Figure 3). For a lossless substrate these poles lie on the real axis between the free space wavenumber (k_0) and the highest wavenumber of the other layers ($MAX(k_1, k_2)$). The residues of the poles correspond to radiated power in the form of TM and TE modes propagating within the substrate layer. For the grounded substrate configuration, the TM_0 surface wave mode has no cutoff frequency. For monolithic arrays and (M)MICS it is desirable to operate at a frequency where only this mode is excited so that radiation losses remain low.

For simplicity, the semi-infinite Sommerfeld integrals are divided into two regions. A combination of numerical and analytical techniques is employed to evaluate the integrals in each region separately. The first region extends from 0 to the parameter A and the second from [A-∞]. The parameter A is chosen to satisfy the condition

$$A_t = \tanh\left(\sqrt{A^2 - k_i^2}\, h_i\right) \doteq 1 \tag{26}$$

where the index (i) refers to the electrically thinest dielectric layer which is adjacent to the microstrip structure. When λ is greater than A, simplifications made in the integrand result in improved accuracy and reduced numerical and computational effort.

In view of the above, the elements of the impedance matrix may be written as

$$Z_{\xi\zeta} = Z_{\xi\zeta}^{A} + Z_{\xi\zeta}^{\infty} \qquad \xi, \zeta = x, y. \tag{27}$$

2.1.1 Evaluation of $Z^A_{\xi\zeta}$

Considering equations (16),(25), and (26), $Z^A_{\xi\zeta}(n,m,\nu,\mu)$ is given by the following expression:

$$\begin{aligned} Z^A_{\xi\zeta}(n,m,\nu,\mu) &= \delta_{\xi\zeta}\,\mathcal{L}_{\xi\xi}(A)\,\langle f_{n_\xi} g_{m_\xi},\, J_0(\lambda\rho),\, f_{\nu_\zeta} g_{\mu_\zeta}\rangle \\ &+ \mathcal{R}_{\xi\zeta}(A)\,\langle f_{n_\xi} g_{m_\xi},\, \frac{\partial^2}{\partial\xi\partial\zeta} J_0(\lambda\rho),\, f_{\nu_\zeta} g_{\mu_\zeta}\rangle \end{aligned} \tag{28}$$

where $\mathcal{L}_{\xi\xi}(A)$ and $\mathcal{R}_{\xi\zeta}(A)$ are integral operators given by

$$\mathcal{L}_{\xi\xi}(A) = k_i^2 \int_0^A d\lambda f_{\xi\xi} \tag{29}$$

$$\mathcal{R}_{\xi\zeta}(A) = \int_0^A d\lambda (f_{\zeta\zeta} + f_{z\zeta}). \tag{30}$$

The real-axis evaluation of the Sommerfeld integrals with simple pole singularities is given in [17]. As mentioned, the double inner products contain quadruple integrals which would result in unacceptable numerical error and excessive CPU time, if the integrations were performed numerically. This difficulty has been overcome by reducing the integrals to convergent series. Along these lines, the Bessel function and its derivatives may be written in integral form as

$$J_0(\lambda\rho) = \frac{1}{2\pi}\int_{-\pi}^{\pi} e^{j\lambda(x-x')\cos\phi} e^{j\lambda(y-y')\sin\phi} d\phi \tag{31}$$

$$\frac{\partial^{\sigma+\tau}}{\partial x^\sigma \partial y^\tau} J_0(\lambda\rho) = \frac{1}{2\pi}\int_{-\pi}^{\pi} (j\lambda\cos\phi)^\sigma (j\lambda\sin\phi)^\tau e^{j\lambda(x-x')\cos\phi} e^{j\lambda(y-y')\sin\phi} d\phi \tag{32}$$

Employing these relations the quadruple integrals can be reduced to quickly con-

Employing these relations the quadruple integrals can be reduced to quickly con-

Employing these relations the quadruple integrals can be reduced to quickly converging series as shown in Appendix A. The series are of the form

$$\begin{aligned} &\langle f_{n_\xi} g_{m_\xi},\, J_0(\lambda\rho),\, f_{\nu_\xi} g_{\mu_\xi}\rangle \\ &= \sum_{k=0}^{\infty}\sum_{k'=0}^{\infty}\sum_{l=0}^{\infty}\sum_{l'=0}^{\infty} A_{2k} A_{2k'} B_l B_{l'} (-1)^{k+k'} (-j)^{l+l'} \frac{\partial^{2(k+k')+(l+l')} J_0(\lambda\rho)}{(\partial|\xi-\xi'|)^{2(k+k')} (\partial|\zeta-\zeta'|)^{(l+l')}} \end{aligned} \tag{33}$$

$$\langle f_{n_\xi} g_{m_\xi}, \frac{\partial^2}{\partial \xi^2} J_0(\lambda\rho), f_{\nu_\xi} g_{\mu_\xi} \rangle \tag{34}$$

$$= \sum_{k=0}^{\infty}\sum_{k'=0}^{\infty}\sum_{l=0}^{\infty}\sum_{l'=0}^{\infty} A_{2k}A_{2k'}B_lB_{l'}(-1)^{k+k'}(-j)^{l+l'}\frac{\partial^{2(k+k'+1)+(l+l')}J_0(\lambda\rho)}{(\partial|\xi-\xi'|)^{2(k+k'+1)}(\partial|\zeta-\zeta'|)^{(l+l')}}$$

$$\langle f_{n_\xi} g_{m_\xi}, \frac{\partial^2}{\partial \xi \partial \zeta} J_0(\lambda\rho), f_{\nu_\zeta} g_{\mu_\zeta} \rangle \tag{35}$$

$$= \sum_{k=0}^{\infty}\sum_{k'=0}^{\infty}\sum_{l=0}^{\infty}\sum_{l'=0}^{\infty} A_{2k}A_{2k'}B_lB_{l'}(-1)^{k+k'}(-j)^{l+l'}\frac{\partial^{2(k+k'+1)+(l+l')}J_0(\lambda\rho)}{(\partial|\xi-\xi'|)^{(2k+l'+1)}(\partial|\zeta-\zeta'|)^{(2k'+l+1)}}.$$

where $\xi, \zeta = x, y (\xi \neq \zeta)$, and $\rho = \sqrt{(\xi_{\nu_\xi} - \xi_{n_\xi})^2 + (\zeta_{\mu_\zeta} - \zeta_{m_\zeta})^2}$. Although these summations result in a considerable reduction of computations, they still require the vast majority of CPU time.

2.1.2 Evaluation of $Z^{\infty}_{\xi\zeta}$

The contribution for the interval from (A ,∞) can be written

$$Z^{(\infty)}_{xx} = \langle f_{n_x} g_{m_x}, \mathcal{K}^{(\infty)}_{xx}, f_{\nu_x} g_{\mu_x} \rangle \tag{36}$$

$$Z^{(\infty)}_{xy} = \langle f_{n_x} g_{m_x}, \mathcal{K}^{(\infty)}_{xy}, f_{\nu_y} g_{\mu_y} \rangle \tag{37}$$

$$Z^{(\infty)}_{yx} = \langle f_{n_y} g_{m_y}, \mathcal{K}^{(\infty)}_{yx}, f_{\nu_x} g_{\mu_x} \rangle \tag{38}$$

$$Z^{(\infty)}_{yy} = \langle f_{n_y} g_{m_y}, \mathcal{K}^{(\infty)}_{yy}, f_{\nu_y} g_{\mu_y} \rangle \tag{39}$$

where

$$\mathcal{K}^{(\infty)}_{\xi\zeta} = \int_A^{\infty} \left[(k_i^2 \delta_{\xi\zeta} + \frac{\partial^2}{\partial\xi\partial\zeta}) f_{\zeta\zeta} + \frac{\partial^2}{\partial\xi\partial\zeta} f_{z\zeta} \right] J_0(\lambda\rho) d\lambda. \tag{40}$$

When A is chosen according to equation (26), simplifications may be made in the integrand of the Green's function resulting in the expressions

$$\mathcal{K}^{(\infty)}_{\xi\zeta} = \mathcal{H}^{(\infty)}_{\xi\zeta} - \mathcal{H}^{(A)}_{\xi\zeta} \tag{41}$$

where

$$\mathcal{H}_{\xi\zeta}^{(\infty)} = \left\{ h_{\zeta\zeta} \left[\delta_{\xi\zeta} + \frac{\partial^2}{\partial\xi\partial\zeta} \right] + h_{z\zeta} \frac{\partial^2}{\partial\xi\partial\zeta} \right\} \frac{1}{\sqrt{\rho^2 + \left(\frac{t}{f(A)}\right)^2}} \tag{42}$$

and

$$\mathcal{H}_{\xi\zeta}^{(A)} = \int_0^A d\lambda \left[h_{\zeta\zeta}(\delta_{\xi\zeta} + \frac{\partial^2}{\partial\xi\partial\zeta}) + h_{z\zeta}\frac{\partial^2}{\partial\xi\partial\zeta} \right] J_0(\lambda\rho)\frac{e^{-\lambda t f(A)}}{f(A)}. \tag{43}$$

In equations (42) and (43), $f(A)$, $h_{\zeta\zeta}$, and $h_{z\zeta}$ are constants given by

$$h_{\zeta\zeta} = \frac{1}{2\left[1-\epsilon_2(A)\right] f(A)} \tag{44}$$

$$h_{z\zeta} = \frac{1}{2f(A)} \left(\frac{1}{\left[1-\epsilon_2(A)\right]} - \frac{2}{\left[(\epsilon_{rA}+\epsilon_{r1})(1-\epsilon_3(A))\right]} \right) \tag{45}$$

with

$$f(A) = \sqrt{1 + \frac{k_1^2}{A^2 - k_1^2}} \tag{46}$$

$$\epsilon_2 = \frac{k_2^2 - k_1^2}{4(A^2 - k_1^2)} \tag{47}$$

$$\epsilon_3 = \frac{\epsilon_{r1}}{2(\epsilon_{r1}+\epsilon_{r2})} \frac{k_2^2 - k_1^2}{4(A^2 - k_1^2)} \tag{48}$$

for the case of a superstrate/substrate configuration. When the superstrate is not present ϵ_{r1}, and ϵ_{r2} are replaced by the quantities ϵ_{r0}, and ϵ_{r1}, respectively.

Substitution of (41) into (36)-(39) gives

$$Z_{\xi\zeta}^{(\infty)} = \langle f_{n_\xi} g_{m_\xi}, \mathcal{H}_{\xi\zeta}^{(\infty)}, f_{\nu_\zeta} g_{\mu_\zeta} \rangle - \langle f_{n_\xi} g_{m_\xi}, \mathcal{H}_{\xi\zeta}^{(A)}, f_{\nu_\zeta} g_{\mu_\zeta} \rangle. \tag{49}$$

The quantity containing $\mathcal{H}_{\xi\zeta}^{(A)}$ can be handled in exactly the same manner as $Z_{\xi\zeta}^{A}$. The derivatives present in the double inner product involving $\mathcal{H}_{\xi\zeta}^{(\infty)}$ can be eliminated through integration by parts, resulting in the expressions

$$\langle f_{n_\xi} g_{m_\xi}, \frac{\partial^2}{\partial\xi^2} \frac{1}{\sqrt{\rho^2 + \frac{t}{f(A)}^2}}, f_{\nu_\xi} g_{\mu_\xi} \rangle$$

$$= \int_{\zeta_{m_\xi}}^{\zeta_{m_\xi+1}} d\zeta' \int_{\zeta_{\mu_\xi}}^{\zeta_{\mu_\xi+1}} d\zeta \int_{-l_\xi}^{l_\xi} d\xi \sin\left(k_s(l_\xi - |\xi|)\right)$$

$$+ \left(\frac{1}{\sqrt{\rho_A^2 + \left(\frac{t}{f(A)}\right)^2}} + \frac{1}{\sqrt{\rho_B^2 + \left(\frac{t}{f(A)}\right)^2}} - \frac{2\cos\left(k_s l_\xi\right)}{\sqrt{\rho_C^2 + \left(\frac{t}{f(A)}\right)^2}} \right) \tag{50}$$

and

$$\langle f_{n_\xi} g_{m_\xi}, \frac{\partial^2}{\partial\xi\partial\zeta} \frac{1}{\sqrt{\rho^2 + \left(\frac{t}{f(A)}\right)^2}}, f_{\nu_\zeta} g_{\mu_\zeta} \rangle$$

$$= \int_{-l_\xi}^{l_\xi} d\xi \int_{-l_\zeta}^{l_\zeta} d\zeta' \sin\left(k_s(l_\xi - |\xi|)\right) \sin\left(k_s(l_\zeta - |\zeta'|)\right)$$

$$\left(\frac{1}{\sqrt{\rho_D^2 + \left(\frac{t}{f(A)}\right)^2}} + \frac{1}{\sqrt{\rho_E^2 + \left(\frac{t}{f(A)}\right)^2}} - \frac{1}{\sqrt{\rho_F^2 + \left(\frac{t}{f(A)}\right)^2}} - \frac{1}{\sqrt{\rho_G^2 + \left(\frac{t}{f(A)}\right)^2}} \right) \tag{51}$$

In equations (50) and (51), ρ_{A-G} are functions of ξ and ζ given by

$$\begin{aligned}
\rho_A^2 &= (\zeta - \zeta')^2 + (\xi + \xi_{\nu_\xi} - \xi_{n_\xi} + l_\xi)^2 \\
\rho_B^2 &= (\zeta - \zeta')^2 + (\xi + \xi_{\nu_\xi} - \xi_{n_\xi} - l_\xi)^2 \\
\rho_C^2 &= (\zeta - \zeta')^2 + (\xi + \xi_{\nu_\xi} - \xi_{n_\xi})^2 \\
\rho_D^2 &= (l_\zeta - \zeta' + \zeta_{\mu_\xi} - \zeta_{m_\zeta})^2 + (\xi + \xi_{\nu_\xi} - \xi_{n_\zeta})^2 \\
\rho_E^2 &= (-\zeta' + \zeta_{\mu_\xi} - \zeta_{m_\zeta})^2 + (\xi + \xi_{\nu_\xi} - \xi_{n_\zeta} + l_\xi)^2 \\
\rho_F^2 &= (-\zeta' + \zeta_{\mu_\xi} - \zeta_{m_\zeta})^2 + (\xi + \xi_{\nu_\xi} - \xi_{n_\zeta})^2 \\
\rho_G^2 &= (l_\zeta - \zeta' + \zeta_{\mu_\xi} - \zeta_{m_\zeta})^2 + (\xi + \xi_{\nu_\xi} - \xi_{n_\zeta} + l_\xi)^2
\end{aligned} \tag{52}$$

2.2 Numerical Considerations

2.2.1 Formation of the Impedance Matrix

As mentioned in the previous section, the discretization of the entire (M)MIC surface enclosing the microstrip discontinuity (Figure 2) has been performed. The

reason for this approach is two-fold. On one hand, it allows the maximum utilization of symmetry inherently present in the open microstrip problem as will be discussed shortly. Secondly, this type of discretization is not discontinuity dependent, and other elements having the same substrate may be analyzed without the re-evaluation of the impedance matrix elements. For the desired microstrip element, a simple routine correctly fills the impedance matrix from these pre-existing elements according to the discontinuity shape and the known boundary conditions. Therefore, if a design is to be made on a specific substrate (such as GaAs or Alumina), impedance matrix elements can be pre-computed and stored in libraries, and re-used indefinitely for the synthesis of the desired performance. However, it must be noted that for very large problems, solving the matrix can be as time-consuming as generating the matrix elements.

The mesh of Figure 2 shows a total of $(N_i M_i), (i = x, y)$ node points resulting in a total of $(N_x M_x)^2 + (N_y M_y)^2$ interactions for the direct terms (Z_{xx}, Z_{yy}) and $(N_x M_x N_y M_y)$ interactions for the cross-coupled terms (Z_{yx}, Z_{xy}). Fortunately, this number can be reduced significantly by symmetry and reciprocity. From equations (21)-(25) it can be shown that the spatial dependence in the direct terms is an even function of the quantities $(x - x')$ and $(y - y')$. Furthermore, the cross-coupled interactions are odd functions of these quantities. Therefore, elements may be catalogued according to these properties, resulting in large reductions in computational effort. The number of elements computed for the particular submatrix Z_{ij} is reduced to $N_i M_j, (i, j = x, y)$ which is the square root of the previously given numbers. This is not true for shielded microstrip where the proximity of a

subsection to a cavity or waveguide wall is reflected in the spatial dependence of the Green's function.

A three-dimensional view of the impedance matrix is shown in Figure 4. The matrix is toplitz and diagonally dominant with the diagonal elements being the largest contribution by an order of magnitude. The large values of elements off the diagonal results from interactions of adjacent cells and their location in the impedance matrix depends on the ordering of the nodes.

2.2.2 Convergence With Respect to the Parameter A

The computational effort required for this problem is greatly influenced by the choice of the parameter A in equation (26). The CPU time needed in the calculation of $Z_{\xi\zeta}^{\infty}$ does not depend on A and is significantly less than the computer time required for the computation of $Z_{\xi\zeta}^{A}$. On the other hand the CPU time for the computation of $Z_{\xi\zeta}^{A}$ increases linearly with increasing A. Therefore, the value of A must be chosen as small as possible, while still achieving numerical convergence. Figures (5) and (6) show the convergence of the phase of S_{12} and the radiated power as a function of A. Table 1 shows the correspondence between the parameters A and A_t. It can be seen that the network parameters show no change for values of A_t above .95. Below $A_t = .9$ the phase S_{12} and the radiation loss gradually deteriorate until the estimated values become completely unacceptable at $A_t = .7$.

Table 1: Choice of A for microstrip Corner Discontinuity of Figs. 5 and 6.

$\frac{A}{\lambda_0}$ (10 GHz)	$\sqrt{A^2 - k^2} \cdot H$	$A_t = \tanh(\sqrt{A^2 - k^2} \cdot H)$
20	0.867	.7
24.8	1.098	.8
32.3	1.472	.9
39.6	1.832	.95
56.5	2.647	.99
80.6	3.800	.999

2.3 Computation of Network Parameters and Radiated Fields

The solution of the matrix equation yields the current on the microstrip conducting strips as shown in Figure 7 for a T-junction discontinuity. This current clearly shows the formation of standing waves and the edge effect. From the current distribution the network parameters may be computed as shown in [7]. The radiated fields may be obtained from the integral equation. This is done by applying a saddle point integration technique as given in [13].

3 Numerical Results

As discussed extensively in the literature [8], the efficiency of a printed antenna depends on the shape and size of the antenna and on the electric size and consistency of the dielectric substrate. An extensive study performed by [8],[9] has shown that the use of an appropriate combination of substrate and superstrate layers can improve the radiation performance by eliminating the surface waves. In

monolithic array applications, where the individual antennas are fed by extensive feeding networks, an improvement in the radiation efficiency of the antennas by this technique will increase the parasitic radiation. As a result, the techniques for surface wave suppression have to be re-evaluated.

In this paper, substrate/superstrate and two-layer substrate combinations made of duroid ($\epsilon_r = 2.2$) and GaAs ($\epsilon_r = 13$), materials widely used in circuits, are considered and the effect of parasitic radiation is computed. Specifically, total radiation losses, and the percentages of surface wave and space wave power are evaluated as functions of the frequency and are compared to the single-layer substrate case.

- *Substrate-Superstrate Configuration*

  Figure 8 shows the total radiated power as a function of frequency for a right-angle bend printed on a 40 mil duroid substrate with and without a 16 mil GaAs cover. The comparison shows clearly the effects of the superstrate from 10 GHz to 20 GHz. In the lower half of the frequency band, the superstrate tends to reduce losses slightly. However, at higher frequencies, the total radiated power has increased by 90% due to the presence of the cover. As Figures 9 and 10 indicate, this excess radiated power comes from the enhancement of space wave radiation which is very desirable in antennas. In monolithic arrays printed on single layer dielectric substrate a careful design of the feeding network could provide parasitic radiation many dBs lower than the primary radiation from the array. The replacement of the single layer by a substrate/superstrate configuration for array efficiency improvement could

increase the power radiated by all the discontinuities included in the feeding structure by 90%. As a result, the level of the total parasitic radiation could become unacceptably high and could deteriorate the array pattern substantially.

- *Two-Layer Substrate*

  In this case, two different comparisons are performed. At first the total power radiated by a right-angle bend printed on a 56 mil duroid is compared to the same bend printed on 40mil-duroid/16mil-GaAs substrate and shows a 20% increase at the upper end of the frequency band mainly coming from the enhancement of the space wave radiation (see Figures 11 and 12). Much higher radiated power is observed when the geometry of the single layer bend is modified to preserve the $100\Omega m$ input/output-port characteristic impedance observed in the two-layer case. The excess loss observed in this case is due to the effects of electrically thick substrates which have been reported in [1].

In both of the above reported cases, the frequency range was chosen so that only one mode is excited in the substrate. Furthermore, the presence of the superstrate or of a second layer with a higher dielectric constant tends to reduce the power of the excited surface wave and increase the power radiated into space waves. These effects have to be taken into account when techniques for enhancement of the radiation efficiency are applied in arrays fed by extensive feeding networks.

4 Conclusion

Radiation losses for microstrip corner discontinuities printed on substrates with one and two dielectric layers, and/or a superstrate are presented. The losses were evaluated with a space domain integral equation approach and were separated into space and surface wave components. It was found that a superstrate, often used for protection or gain enhancement of antenna elements, may increase the loss of the microstrip feed network considerably. This would result in lower overall gain. Therefore, a tradeoff exists between the enhancement of radiation from the antennas and the undesirable radiation in the feed network.

Another comparison between a corner discontinuity on a single layer of duroid, and on a two layer structure (GaAs/duroid) having the same total thickness, showed that the radiation losses were comparable when the conducting strips had the same width. However, it was found that the loss was influenced by the strip width. Specifically, when the width in the single layer case was widened to create the same characteristic impedance as the two layer case, the loss was substantially higher.

Appendix A

This appendix contains the functions included in the expression of the Green's function in equations (3)-(4) The functions are given below for three different substrate configurations.

- *Substrate-Superstrate Configuration*

The functions for the substrate-superstrate geometry of Figure 1(a) in the region $(0 < Z < h_1)$ are given by

$$\mathcal{N}_{\xi\xi}(\lambda) = \lambda \tag{53}$$

$$\mathcal{N}_{z\xi}(\lambda) = u_0 \tag{54}$$

$$\mathcal{Z}_{\xi\xi} = u_1 \cosh\left[ju_1(z-h_1)\right] - u_0 \sinh\left[ju_1(z-h_1)\right] \tag{55}$$

$$\begin{aligned}\mathcal{Z}_{z\xi} &= \left[u_1^2 f_1(\lambda) - u_0^2 f_2(\lambda)\right] \sinh\left[ju_1(z-h_1)\right] \\ &+ u_1 u_0 \left[f_2(\lambda) - \epsilon_{r1} f_1(\lambda)\right] \cosh\left([ju_1(z-h_1)\right]\end{aligned} \tag{56}$$

with $u_i = \sqrt{k_i^2 - \lambda^2}$. The expressions $f_1(\lambda)$ and $f_2(\lambda)$ are the characterisic equations for surface wave modes given by

$$\begin{aligned}f_1(\lambda) &= u_0 \left[u_1 \cosh(ju_1h_1) + u_2 \coth(u_2h_2) \sinh(ju_1h_1)\right] \\ &+ u_1 \left[u_1 \sinh(ju_1h_1) + u_2 \coth(ju_2h_2) \cosh(ju_1h_1)\right]\end{aligned} \tag{57}$$

$$\begin{aligned}f_2(\lambda) &= u_1 \left[\epsilon_{r2}u_1 \sinh(ju_1h_1) \coth(ju_2h_2) + \epsilon_{r1}u_2 \cosh(ju_1h_1)\right] \\ &+ \epsilon_{r1}u_0 \left[\epsilon_{r2}u_1 \coth(ju_2h_2) \cosh(ju_2h_2) + \epsilon_{r1}u_2 \sinh(ju_1h_1)\right].\end{aligned} \tag{58}$$

- *Two-Layer Substrate*

The functions for the two-layer case in Figure 1(b) for the region ($Z > 0$) are given by

$$\mathcal{N}_{\xi\xi}(\lambda) = [u_1 \cosh(ju_1h_1) + u_2 \sinh(ju_1h_1) \coth(ju_2h_2)]\,\lambda \tag{59}$$

$$\begin{aligned}\mathcal{N}_{z\xi}(\lambda) &= j\epsilon_r u_0^2 [\epsilon_{r2}u_1 \cosh(ju_1h_1) \coth(ju_2h_2) + \epsilon_{r1}u_2 \sinh(ju_1h_1)] \\ &\quad [u_1 \cosh(ju_1h_1) + u_2 \coth(u_2h_2) \sinh(ju_1h_1)] \\ &\quad - ju_1^2 [u_1 \sinh(ju_1h_1) + u_2 \coth(ju_2h_2) \cosh(ju_1h_1)] \qquad (60)\end{aligned}$$

$$[\epsilon_{r2}u_1 \coth(ju_2h_2) \cosh(ju_2h_2) + \epsilon_{r1}u_2 \sinh(ju_1h_1)] \tag{61}$$

$$\mathcal{Z}_{\xi\xi} = \mathcal{Z}_{z\xi} = e^{-ju_0z} \tag{62}$$

- *Single-Layer Substrate*

The expressions for the single layer case may be obtained from equations (57)-(60). After some simplification they can be written as

$$\mathcal{N}_{\xi\xi}(\lambda) = \sinh(ju_1h_1)\lambda \tag{63}$$

$$\mathcal{N}_{z\xi}(\lambda) = [(1-\epsilon_r)\sinh ju_1h \cosh ju_1h]\,\lambda^2 \tag{64}$$

$$f_1(\lambda) = u_0 \sinh ju_1h + u_1 \cosh ju_1h \tag{65}$$

$$f_2(\lambda) = \epsilon_r u_0 \cosh ju_1h + u_1 \sinh ju_1h \tag{66}$$

Appendix B

The quadruple integrals (25) for direct coupled x-x interactions can be written

$$\langle f_{n_x}(x')g_{m_x}(y'),\ J_0(\lambda\rho),\ f_{\nu_x}(x)g_{\mu_x}(y)\rangle \tag{67}$$
$$= \int\int_{S'} dx'dy' \int\int_{S} dxdy\,[f_{n_x}(x')g_{m_x}(y')\,J_0(\lambda\rho)\,f_{\nu_x}(x)g_{\mu_x}(y)]$$

$$\langle f_{n_x}(x')g_{m_x}(y'),\ \frac{\partial^2}{\partial x^2}J_0(\lambda\rho),\ f_{\nu_x}(x)g_{\mu_x}(y)\rangle \tag{68}$$
$$= \int\int_{S'} dx'dy' \int\int_{S} dxdy\left[f_{n_x}(x')g_{m_x}(y')\,\frac{\partial^2}{\partial x^2}J_0(\lambda\rho)\,f_{\nu_x}(x)g_{\mu_x}(y)\right]$$

and for cross coupled x-y terms

$$\langle f_{n_x}(x')g_{m_x}(y'),\ \frac{\partial^2}{\partial x\partial y}J_0(\lambda\rho),\ f_{\nu_y}(x)g_{\mu_y}(y)\rangle \tag{69}$$
$$= \int\int_{S'} dx'dy' \int\int_{S} dxdy\left[f_{n_x}(x')g_{m_x}(y')\,\frac{\partial^2}{\partial x\partial y}J_0(\lambda\rho)\,f_{\nu_y}(y)g_{\mu_y}(x)\right]$$

Employing the integral representation for the first order bessel function in equations (31)-(32), the above may be simplified to the expressions

$$\langle f_{n_x}(x')g_{m_x}(y'),\ J_0(\lambda\rho),\ f_{\nu_x}(x)g_{\mu_x}(y)\rangle$$
$$= \frac{1}{2\pi}\int_{-\pi}^{\pi} e^{j\lambda(x_{\nu_x}-x'_{n_x})\cos(\phi)}e^{j\lambda(y_{\mu_x}-y'_{m_x})\sin(\phi)}$$
$$(\mathcal{R}(\lambda\cos(\phi)))^2\mathcal{U}(\lambda\cos(\phi))\mathcal{U}(-\lambda\cos(\phi))d\phi \tag{70}$$

$$\langle f_{n_x}(x')g_{m_x}(y'),\ \frac{\partial^2}{\partial x^2}J_0(\lambda\rho),\ f_{\nu_x}(x)g_{\mu_x}(y)\rangle$$
$$= \frac{1}{2\pi}\int_{-\pi}^{\pi}(j\lambda\cos\phi)^2 e^{j\lambda(x_{\mu_x}-x'_{n_x})\cos(\phi)}e^{j\lambda(y_{\nu_x}-y'_{m_x})\sin(\phi)}$$
$$\mathcal{R}(\lambda\cos(\phi))^2\mathcal{U}(\lambda\cos(\phi))\mathcal{U}(-\lambda\cos(\phi))d\phi \tag{71}$$

$$\langle f_{n_x}(x')g_{m_x}(y'),\ \frac{\partial^2}{\partial x\partial y}J_0(\lambda\rho),\ f_{\nu_y}(y)g_{\mu_y}(x)\rangle$$
$$= \frac{1}{2\pi}\int_{-\pi}^{\pi}(j\lambda\sin\phi)(j\lambda\cos\phi)e^{j\lambda(x_{\nu_y}-x'_{n_x})\cos(\phi)}e^{j\lambda(y_{\mu_y}-y'_{m_x})\sin(\phi)}$$

$$\mathcal{R}(\lambda\cos(\phi))\mathcal{R}(\lambda\sin(\phi))\mathcal{U}(\lambda\cos(\phi))\mathcal{U}(-\lambda\sin(\phi))d\phi \tag{72}$$

The quantaties $\mathcal{R}$ and $\mathcal{B}$ are convergent series having the form

$$\mathcal{R}(\lambda\cos(\phi)) = \sum_{k=0}^{\infty} A_{2k}(\lambda\cos(\phi))^{2k} \tag{73}$$

$$\mathcal{U}(\lambda\cos(\phi)) = \sum_{l=0}^{\infty} B_l(\lambda\cos(\phi))^l \tag{74}$$

where

$$A_{2k} = \frac{2}{k^{2k+1}}\left([1-\cos(kl_x)] + \sum_{\mu=1}^{k}(-1)^{\mu}\frac{(kl_x)^{2\mu}}{(2\mu)^2}\right) \tag{75}$$

$$B_{2n} = (-1)^n(l_x)^{2n} \tag{76}$$

$$B_{2n+1} = j(-1)^n(l_x)^{2n+1}$$

considering the integral representation for the zero'th order Bessel function these expressions can be re-written as a summation of derivatives of the zero'th order Bessel function appearing in the main text (equations 33-35).

References

[1] N. G. Alexopoulos, P.B. Katehi, and D. Rutledge, "Substrate Optimization for Integrated Circuit Applications," *IEEE Trans. Microwave Theory Tech.*, Vol. MTT-31, pp. 550-557, July, 1983.

[2] P.B. Katehi and N. G. Alexopoulos, "Frequency-Dependent Characteristics of Microstrip Discontinuities in Millimeter-Wave Integrated Circuits",*IEEE Trans. Microwave Theory Tech.*, Vol. MTT-33, Oct. 85, pp. 1029-1035.

[3] J. R. Mosig, "Arbitrarily shaped microstrip structures and their analysis with a mixed potential integral equation, *IEEE Trans. Microwave Theory Tech.*, Vol. MTT-36, pp. 314-323, Feb. 1988.

[4] R. W. Jackson, and D. M. Pozar, "Full-Wave Analysis of Microstrip Open-End and Gap Discontinuities",*IEEE Trans. Microwave Theory Tech.*, Vol. MTT-33,Oct. 85, pp. 1036-1042.

[5] R. Jackson, "Full-Wave Finite Element Analysis of Irregular Microstrip Discontinuities," *IEEE Trans. Microwave Theory Tech.*, Vol. MTT-37, pp. 81-89, Jan. 89.

[6] W. P. Harokopus, Jr. and P. B. Katehi, "An Accurate Characterization of Open Microstrip Discontinuities Including Radiation Losses", *IEEE Microwave Symposium Digest*, pp. 231-234, June 1989.

[7] W. P. Harokopus, Jr. and P. B. Katehi, "Characterization of Open Microstrip Discontinuities on Multilayer Substrates Including Radiation

Losses", *IEEE Trans. Microwave Theory Tech.*, Vol. MTT-37, Dec. 89, pp. 1964-1972.

[8] N.G. Alexopoulos, and D. R. Jackson, "Fundamental Superstrate (Cover) Effects on Printed Circuit Antennas," *IEEE Transactions on Antennas and Propagation*, Vol AP-32, No. 8, pp. 807-814, August 1984.

[9] N.G. Alexopoulos, D. R. Jackson, and P. B. Katehi, "Criteria for Nearly Omnidirectional Patterns for Printed Antennas," *IEEE Transactions on Antennas and Propagation*, Vol AP-33, No. 2, pp. 195-205, February,1985.

[10] W. P. Harokopus, Jr. and P. B. Katehi, "Radiation properties of microstrip discontinuities," *IEEE Ap Digest*, June 1989.

[11] W. P. Harokopus, Jr. and P. B. Katehi, "Radiation properties of microstrip discontinuities," *1990 Radio Science Meeting Program and Abstracts*, page 337, May 1990.

[12] T. S. Horng, S. C. Wu, H. Y. Yang and N. G. Alexopoulos, "A Generalized Method for the Distinction of Radiation and Surface Wave Losses in Microstrip Discontinuities," *IEEE Microwave Symposium Digest*, pp. 1055-1058, May 1990.

[13] W. P. Harokopus, Jr. and P. B. Katehi, "Surface Wave Excitation from Open Microstrip Discontinuities," Submitted for publication to *IEEE Trans. Microwave Theory Tech.*

[14] A. Sommerfeld, Partial Differential Equations in Physics, New York, N.Y., Academic Press, 1949.

[15] R.S. Elliott, "The Green's Function For Electric Dipoles Parallel To and Above or Within a Grounded Dielectric Slab", Hughes Technical Correspondence, 1978.

[16] R. F. Harrington, Field Computation By Moment Methods, Macmillan,N.Y. ,1968.

[17] P.B. Katehi and N. G. Alexopoulos, "Real Axis Integration of sommerfeld Integrals With Applications To Printed Circuit Antennas," *J. Math. Phys.*, vol. 24(3), Mar. 1983.

[18] L.B. Felsen and N. Marcuvitz, Radiation and Scattering of Waves,Prentice Hall, Englewood Cliffs, N.J. 1973.

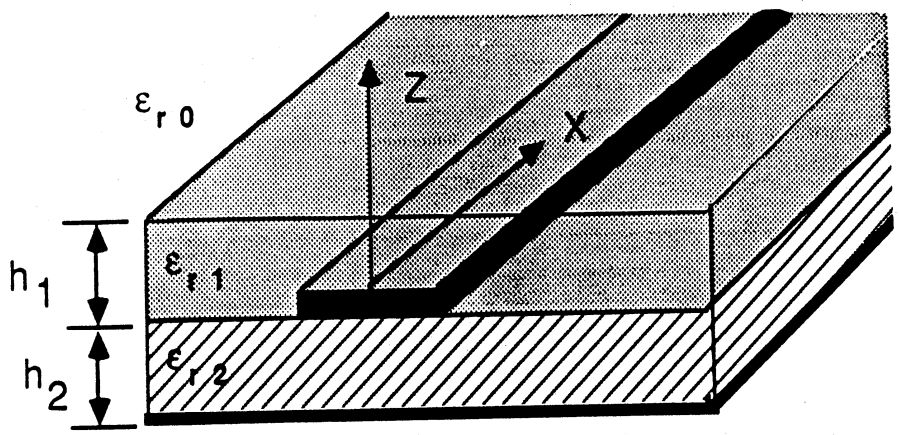

a. Substrate-Superstrate

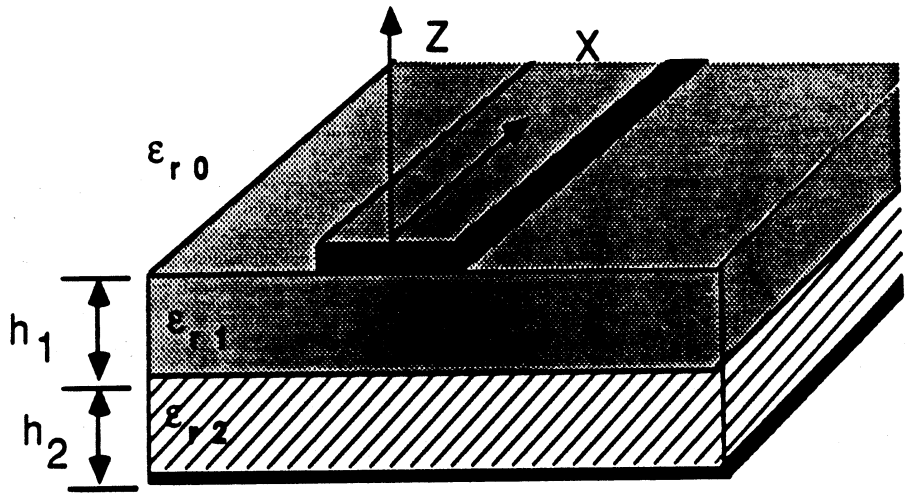

b. Two-layer Substrate

Figure 1: Multilayer Open Microstrip Geometry

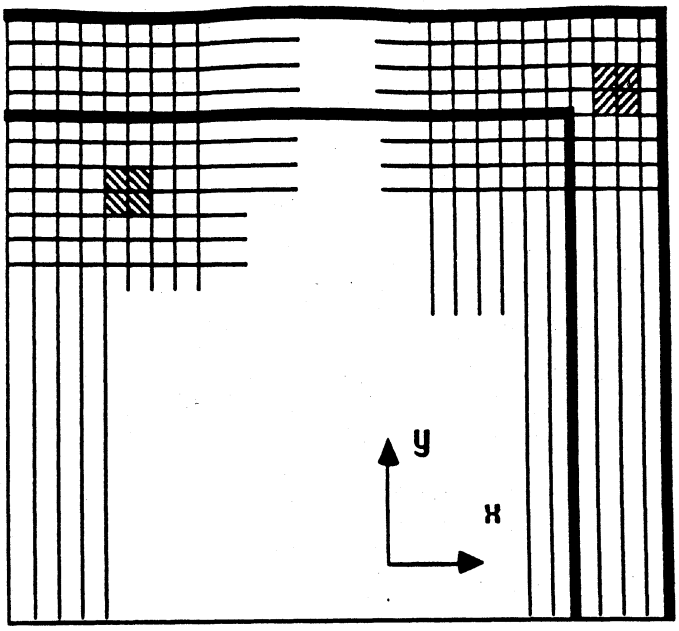

a. Typical Discretization

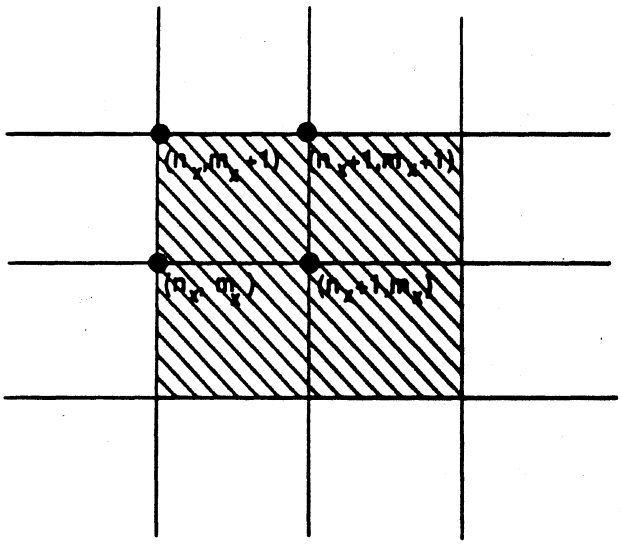

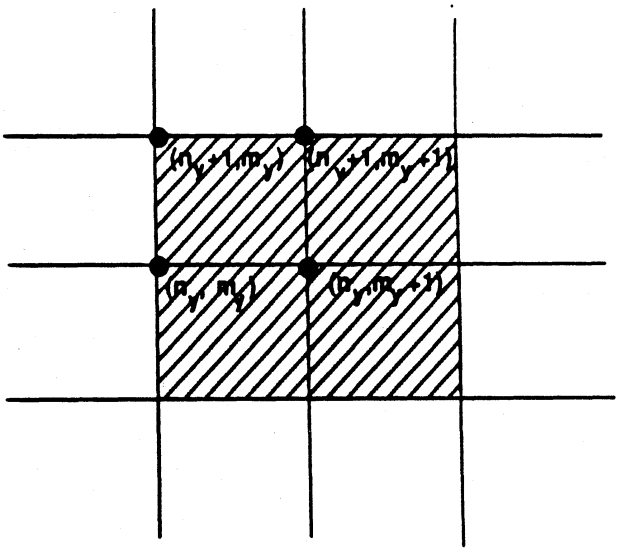

b. X-directed Mesh

Y-directed Mesh

Figure 2: Sub-division of (M)MIC area around Corner Discontinuity

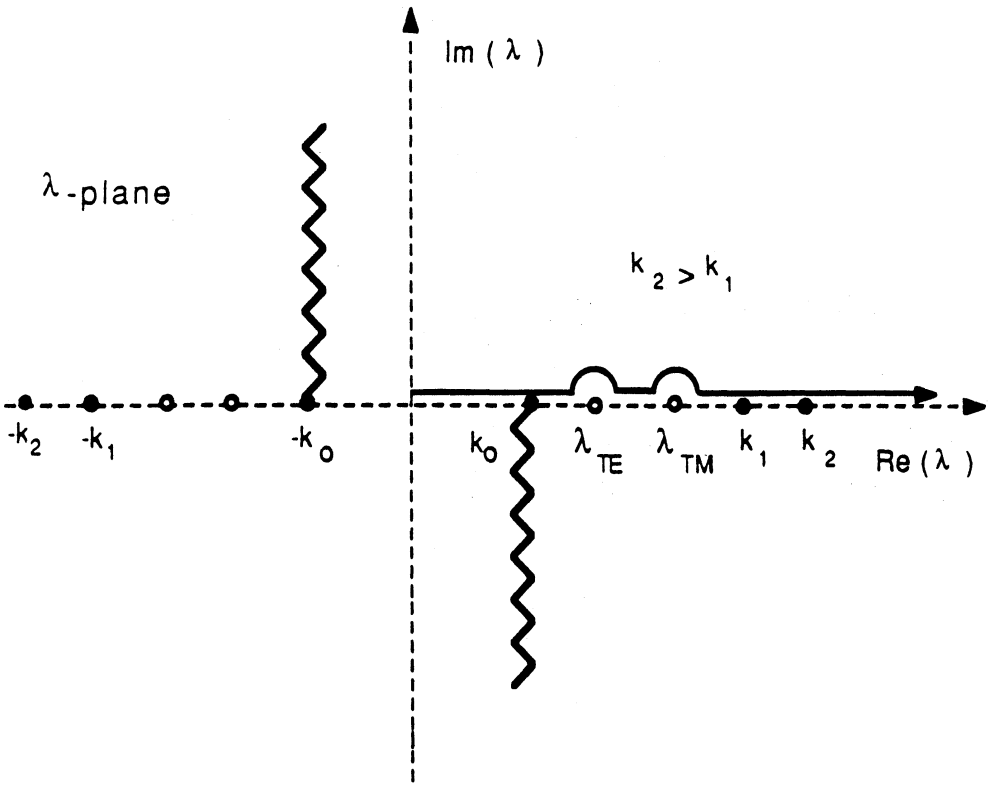

Figure 3: Real Axis Integration of Sommerfeld Integral

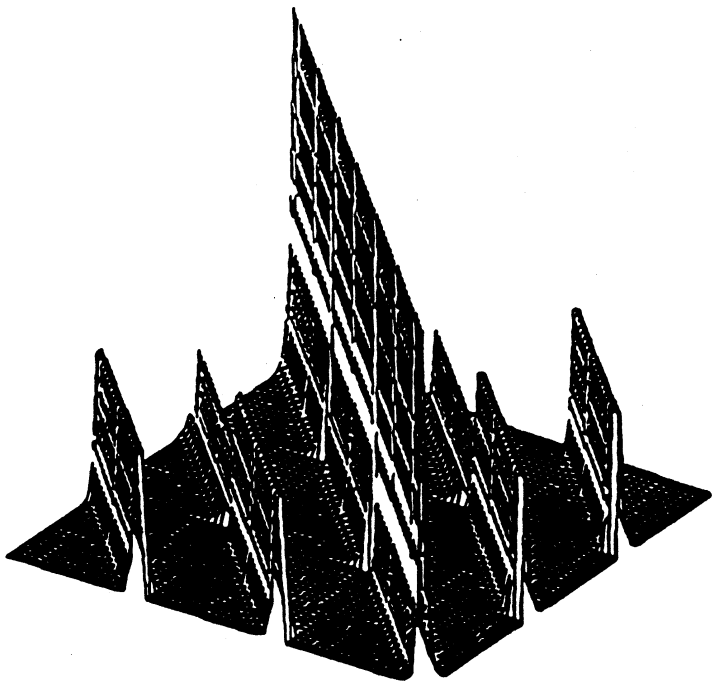

Figure 4: Impedance Matrix

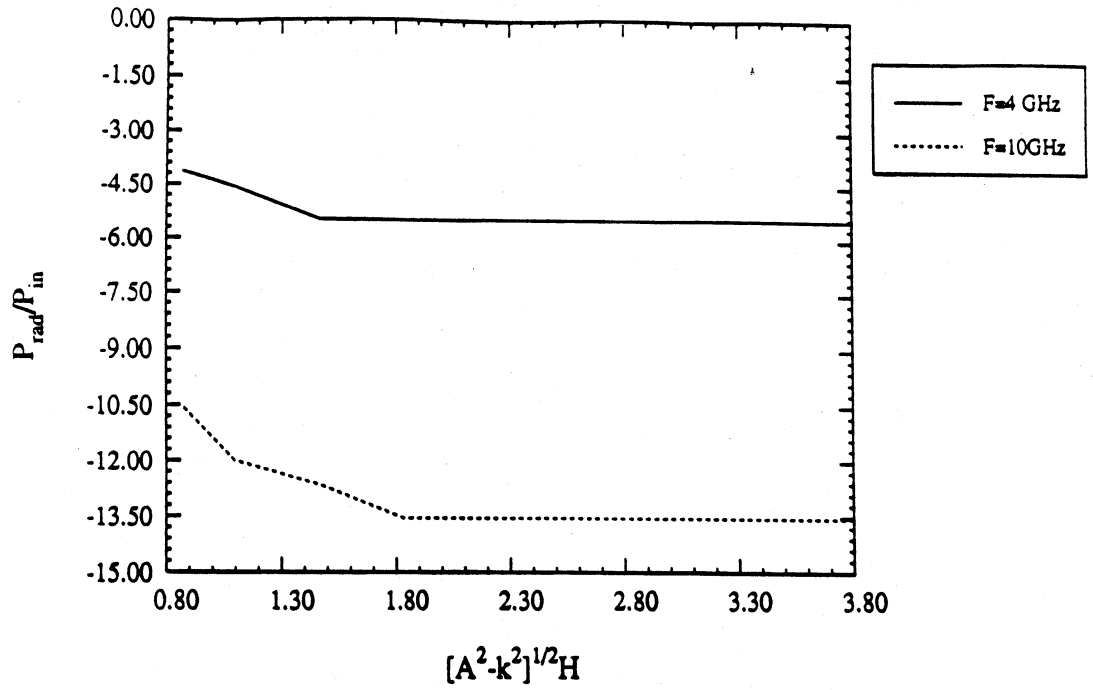

Figure 5: Convergence of the Phase of S_{12} as a function of the parameter A for a microstrip corner discontinuity ($w = 56mil, h_1 = 56mil, \epsilon_{r1} = 2$)

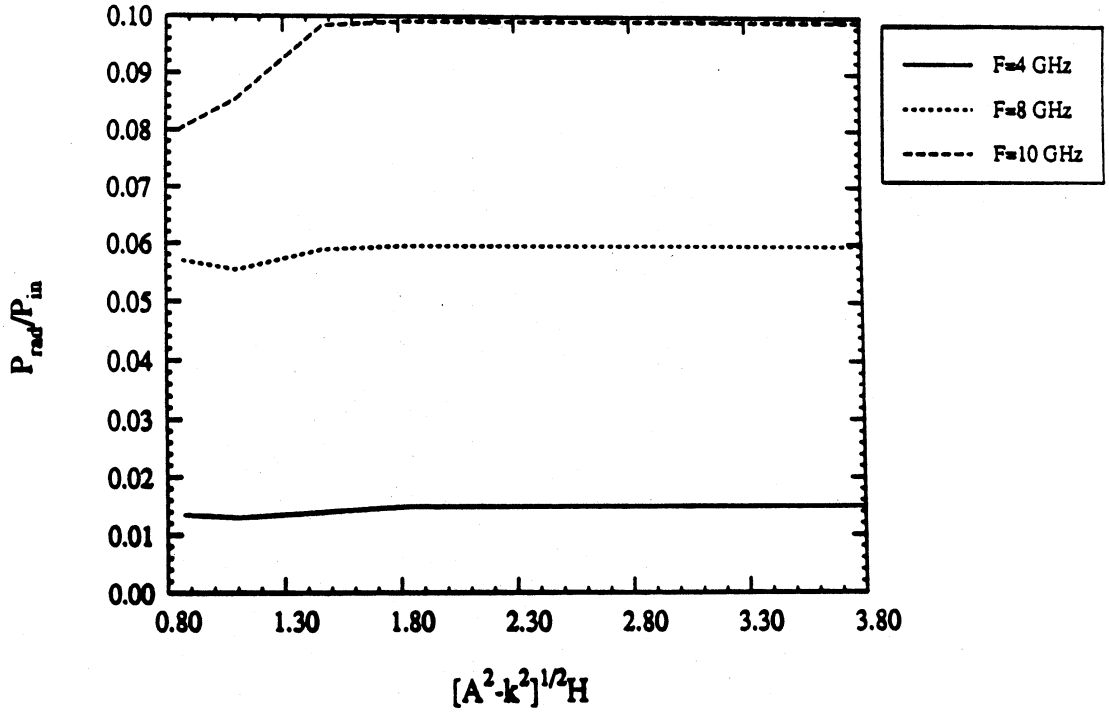

Figure 6: Convergence of the radiation loss as a function of the parameter A for a microstrip corner discontinuity ($w = 56mil, h_1 = 56mil, \epsilon_{r1} = 2$)

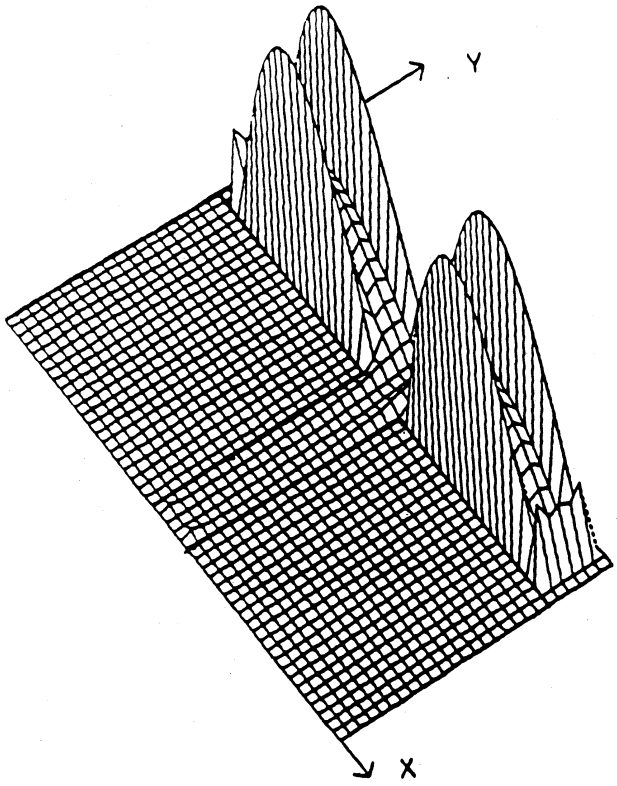

a. X-directed Current on Tee

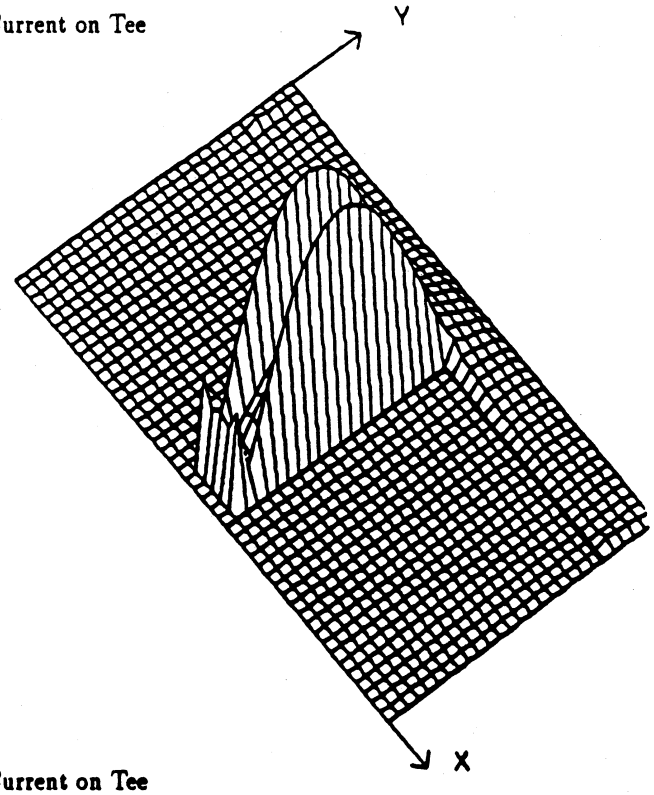

b. Y-directed Current on Tee

Figure 7: Current On T-Junction Excited by Gap Generators ($\epsilon_{r1} = 4, h_1 = .4mm, w = .2mm$)

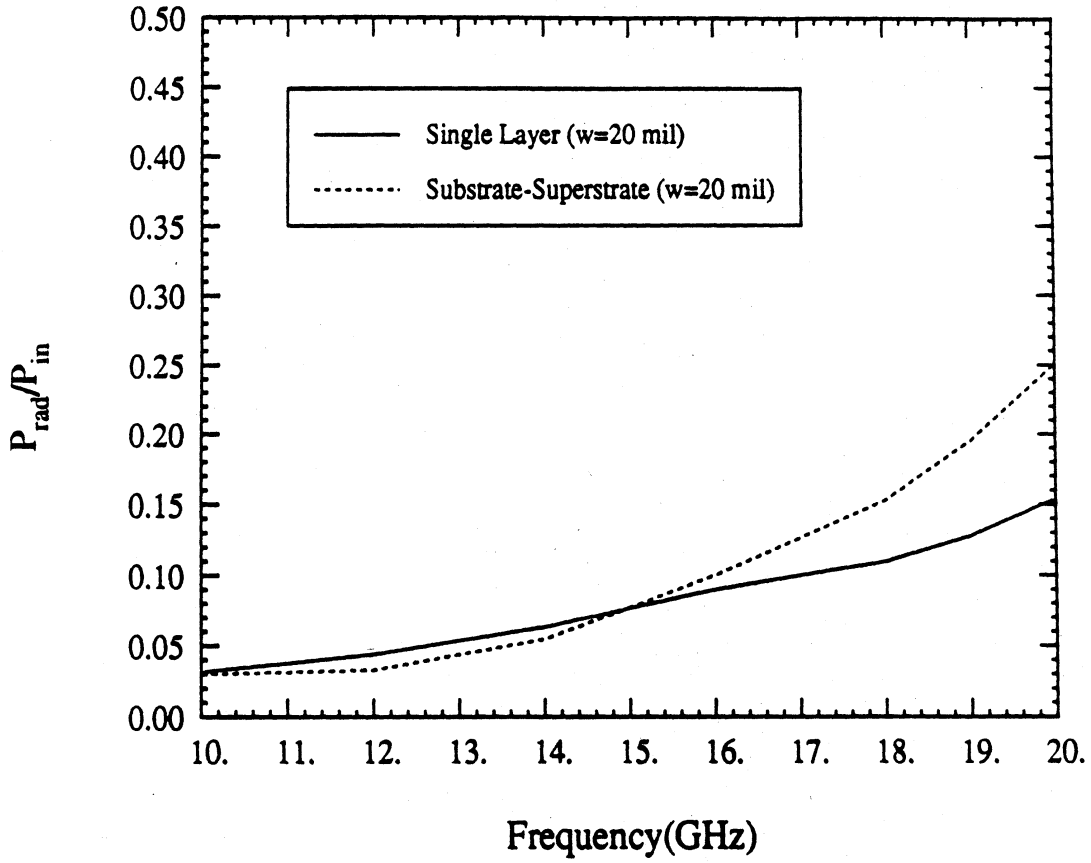

Figure 8: Total Radiation Loss for a microstrip corner discontinuity with a superstrate ($h_1 = 16mil, h_2 = 40mil, \epsilon_{r1} = 13, \epsilon_{r2} = 2$) and without a superstarte($h_1 = 40mil, \epsilon_{r1} = 2$)

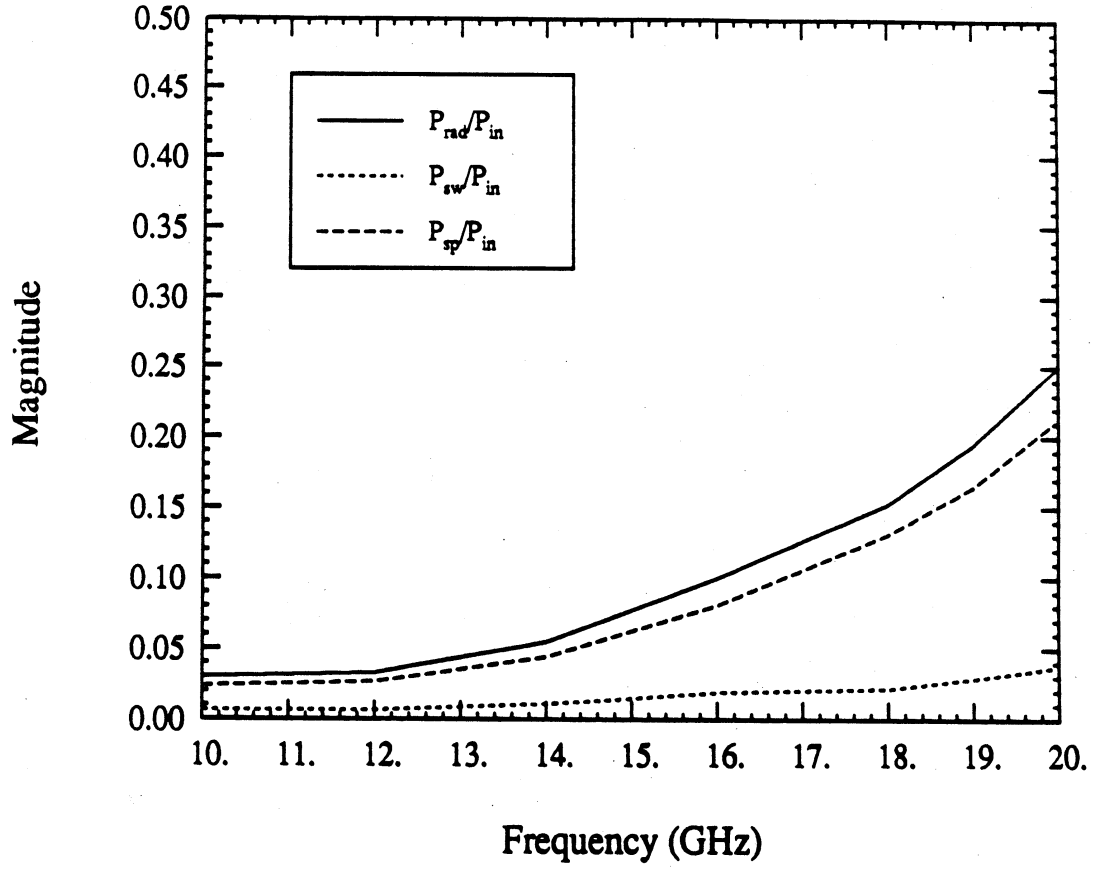

Figure 9: Radiation Loss for a microstrip corner discontinuity with a superstrate ($h_1 = 16mil, h_2 = 40mil, \epsilon_{r1} = 13, \epsilon_{r2} = 2$)

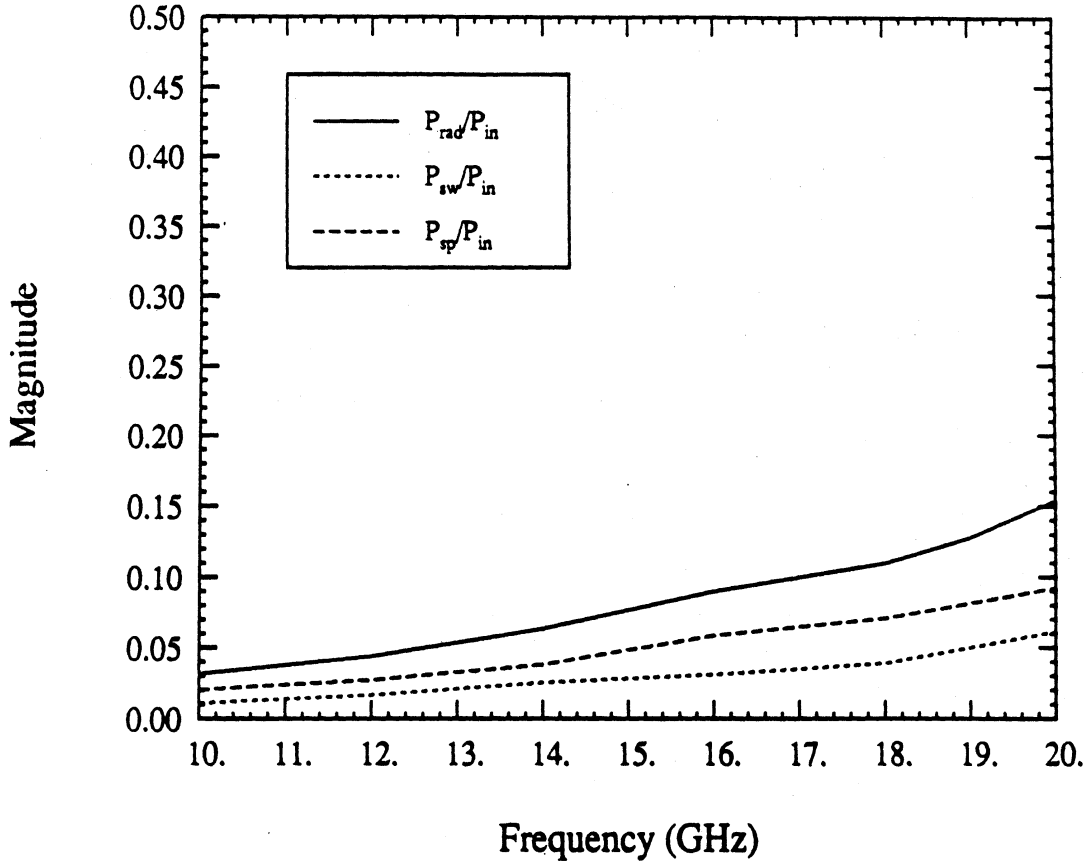

Figure 10: Radiation Loss for a microstrip corner discontinuity on a single layer($h_1 = 40mil, \epsilon_{r1} = 2$)

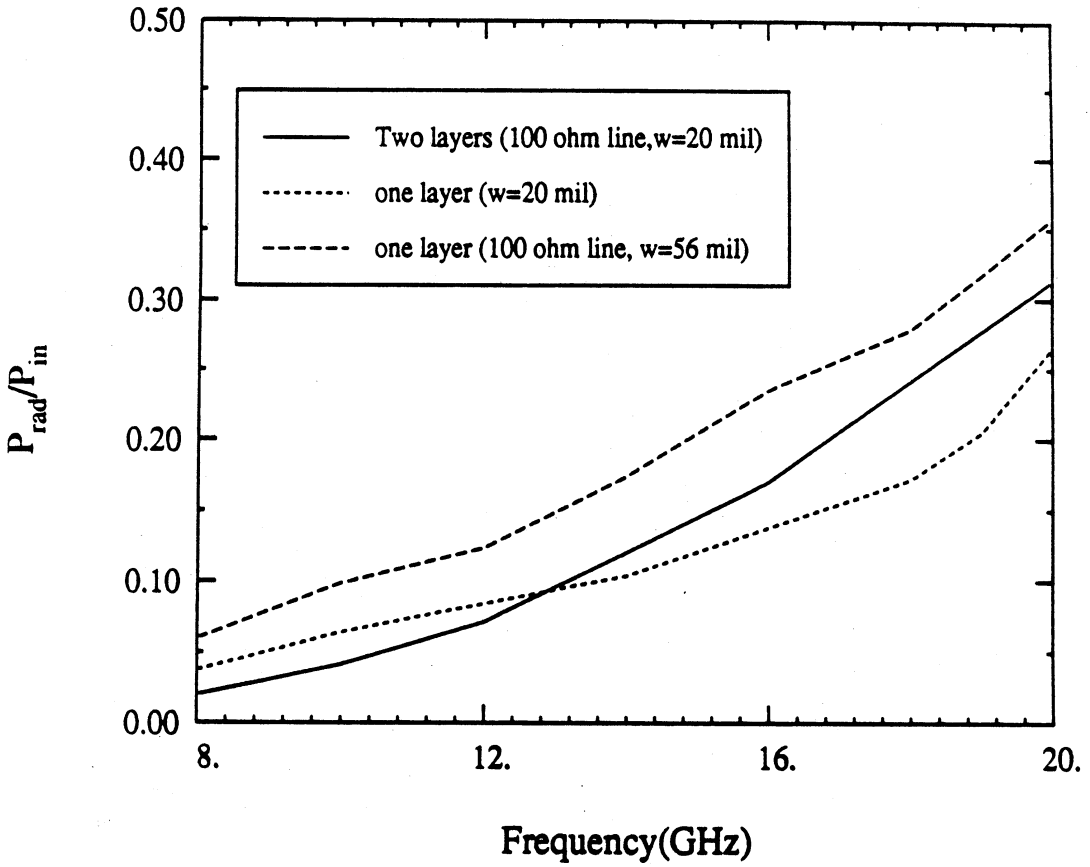

Figure 11: Total Radiation Loss for a microstrip corner discontinuity with a two-layer substrate ($h_1 = 16mil, h_2 = 40mil, \epsilon_{r1} = 13, \epsilon_{r2} = 2$) and with a single layer substrate($h_1 = 56mil, \epsilon_{r1} = 2$)

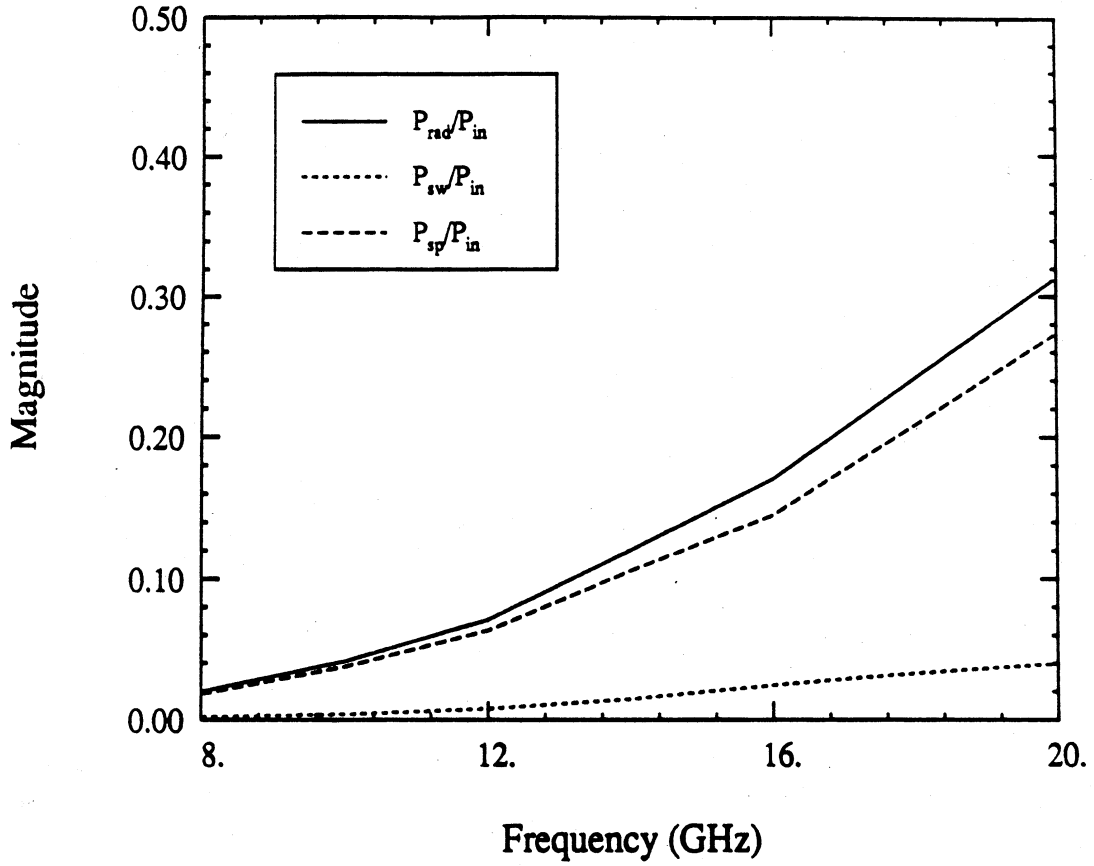

Figure 12: Radiation Loss for a microstrip corner discontinuity with a two-layer substrate ($h_1 = 16mil, h_2 = 40mil, \epsilon_{r1} = 13, \epsilon_{r2} = 2$)

APPENDIX E

Characteristic Impedance and EM Field Distribution in MIS Microstrip

T.G. Livernois and P.B. Katehi

CHARACTERISTIC IMPEDANCE AND EM FIELD DISTRIBUTION IN MIS MICROSTRIP

by

Thomas G. Livernois and Pisti B. Katehi
Radiation Laboratory
Department of Electrical Engineering
and Computer Science
The University of Michigan
Ann Arbor, MI 48109-2122

:teristic impedance for the MIS microstrip is calculated using a space domain representation of EM fields; obtained numerical results are compared to published experimental data. Transverse field distributions for various structural parameters are presented and used to illustrate the three distinct modes of operation for MIS transmission lines.

INTRODUCTION

Slow-wave transmission lines have been extensively studied both experimentally and theoretically, [1-4]. Depending on its structural and material parameters, a typical guide can support three distinct modes: i) quasi-TEM, ii) skin-effect, iii) slow-wave. The operation mechanism for each mode will be briefly discussed in this paper. The simplest slow-wave transmission line is the MIS (metal-insulator-semiconductor) microstrip. When the conductivity of the semiconducting layer is small the substrate may be treated as a low-loss dielectric; electric and magnetic fields penetrate through the substrate to the ground plane and this is called the quasi-TEM mode. When the conductivity is quite large the lossy layer behaves like an imperfect ground plane; electric and magnetic fields are virtually shielded from it and both are concentrated primarily in the thin insulating layer. This case is termed the skin-effect mode. When the conductivity is such that the magnetic field penetrates into the semiconducting layer but the electric field does not, the slow-wave mode exists. Under these conditions, the electric and magnetic energies are spatially separated. This causes a large relative increase in the line capacitance, while the line inductance changes little.

The result is an extremely low phase velocity and relatively smaller propagation losses (as compared to the quasi-TEM and skin-effect modes). The slowing effect can be used to fabricate phase shifters, delay lines and related devices.

Until recently, [3], rigorous calculation of MIS line parameters were done using either spectral analysis or finite elements. In [3], a space domain analysis of several slow-wave transmission lines was given. The present work uses the space domain representation of the electromagnetic fields supported by an MIS microstrip line to calculate characteristic impedance; numerical results are compared to published experimental data. Transverse EM field distributions are also given and they illustrate clearly the existence of the three modes of operation discussed.

THEORY

Figure 1 illustrates a shielded MIS microstrip transmission line. The electromagnetic fields maintained by the impressed currents on the conducting strip may be expressed in the space domain via the method given in [3]. Once the expressions for the fields are found, it is easy to calculate the characteristic impedance. The complex Poynting vector is integrated across the waveguide aperture to find the total complex power flow. The power-current definition for characteristic impedance is then used.

NUMERICAL RESULTS

A. Characteristic Impedance

The characteristic impedance of the MIS line shown in Figure 1 was calculated versus frequency for $\sigma = 0.05\ (\Omega.cm)^{-1}$, $w = 160\mu m$, and $d = 1\mu m$. Waveguide dimensions and layer permittivities are also given there. The real part of Z_0 is plotted in Figure 2 and experimental results, [4], are also shown. The imaginary part of Z_0 for this structure is compared with experimental results in Figure 3. Clearly, excellent agreement is found for both cases. When $f > 2$ GHz, Re $[Z_0]$ increases rapidly. This is due to the transition from the slow-wave to the quasi-TEM mode, as shown by the frequency-resistivity chart given in [5]. Since the relative line capacitance decreases during this transition, we would expect an increase in Re $[Z_0]$. The imaginary part of Z_0 reaches a maximum of about 18 Ω at $f = 5$ GHz and then decreases for increasing f. Im $[Z_0]$ essentially results from reactive power flow. Since the line capacitance decreases during this transition, so too does the reactive energy flow. Hence, the decrease in Im $[Z_0]$ is expected.

Changes between operation modes as a function of frequency in the MIS line are gradual processes, [4]. Consequently, line parameters ought to change similarly. Both our results and the experimental data show this tendency.

B. Transverse Field Distribution

Electromagnetic field distributions maintained in the shielded MIS transmission line, spatially oriented as shown in Figure 4, may be used to illustrate the three distinct modes of operation. The space-domain analysis lends itself to easily obtainable plots of the magnitude of the transverse EM fields versus the 2-d aperture. Figures 5 through 10 show such graphs, with each case being clearly identified. For all field plots, w = 500 μm and d = 1 μm. The quasi-TEM situation, Figures 5 and 6, shows that both electric and magnetic fields penetrate completely through the substrate. At the other extreme, however, we see in Figures 7 and 8 for the skin-effect mode that neither field penetrates; both are essentially concentrated beneath the microstrip conductor. Between these limiting cases lies the slow-wave mode distributions, shown in Figures 9 and 10. The electric field in this case is shielded from the semiconducting layer while the magnetic field is not. The result is the expected spatial separation of electric and magnetic energies. The transverse field edge singularity is seen in all field plots. To clearly determine the mode of operation, the frequency-resistivity chart developed by Hasegawa et al was utilized.

CONCLUSION

A rigorous study of MIS microstrip transmission lines has been presented. Characteristic impedance values obtained in the analysis were compared to published experimental results and excellent agreement was found. Also, spatial EM field distributions were presented and they clearly illustrate the three distinct modes of operation for MIS transmission lines.

ACKNOWLEDGEMENTS

This research was supported by grant ECS-8602530 from the National Science Foundation.

REFERENCES

1. Planar Transmission Structures, ed. T. Itoh, IEEE Press, New York, 1987.

2. M. Aubourg, J. Villotte, F. Godon, and Y. Garault, "Finite Element Analysis of Lossy Waveguides - Application to Microstrip Lines on Semiconductor Substrate," IEEE Trans. Microwave Theory Tech., Vol. MTT-31, pp. 326-331, April 1983.

3. T. Livernois and P. Katehi, "A Generalized Method for Deriving the Space-Domain Green's Function in a Shielded, Multilayer Substrate Structure with Applications to MIS Slow-Wave Transmission Lines," IEEE Trans. Microwave Theory Tech., Vol. MTT-37, Nov. 1989.

4. H. Hasegawa, M. Furukawa, and H. Yanai, "Properties of Microstriplines in Si-SiO_2 System," IEEE Trans. Microwave Theory Tech., Vol. MTT-19, pp. 869-881, Nov. 1971.

5. H. Hasegawa and S. Seki, "Analysis on Interconnection Delay on very High-Speed LSI/VLSI Chips Using an MIS Microstrip Line Model," IEEE Trans. Microwave Theory Tech., Vol. MTT-32, pp. 1721-1727, Dec. 1984.

LIST OF FIGURES

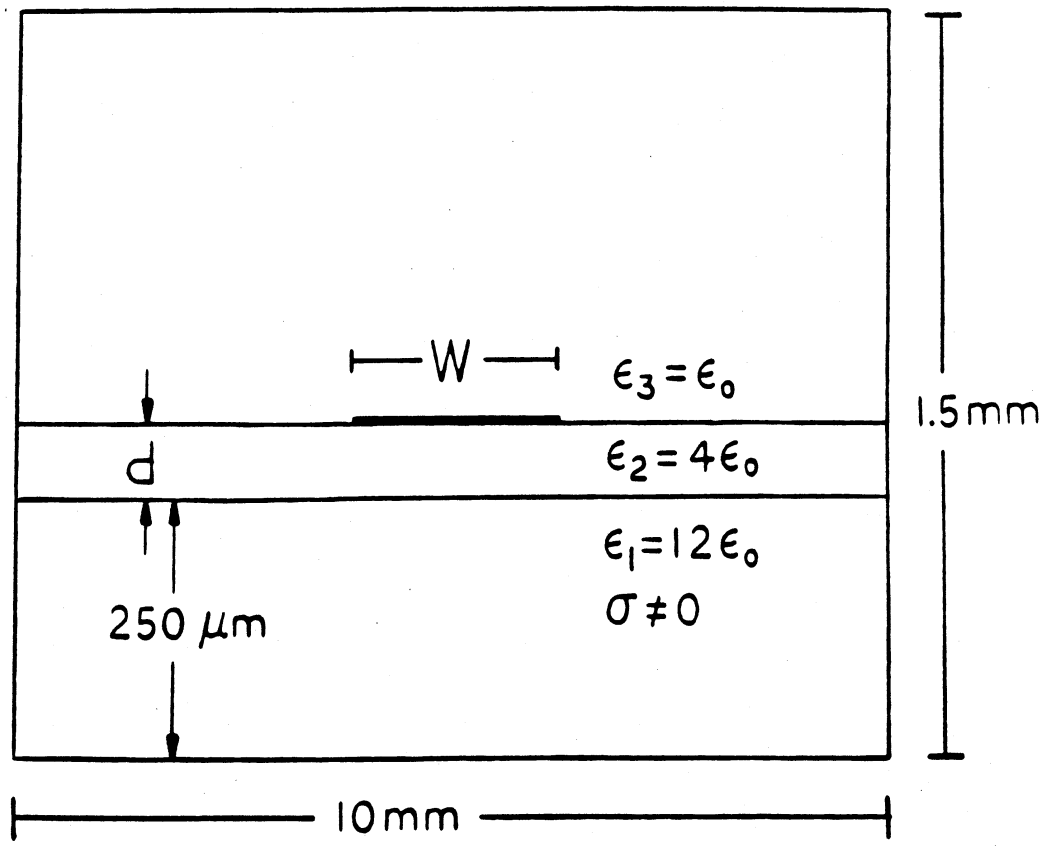
W
$\epsilon_3 = \epsilon_0$
d
$\epsilon_2 = 4\epsilon_0$
$\epsilon_1 = 12\epsilon_0$
$\sigma \neq 0$
250 μm
1.5mm
10mm

Figure 1

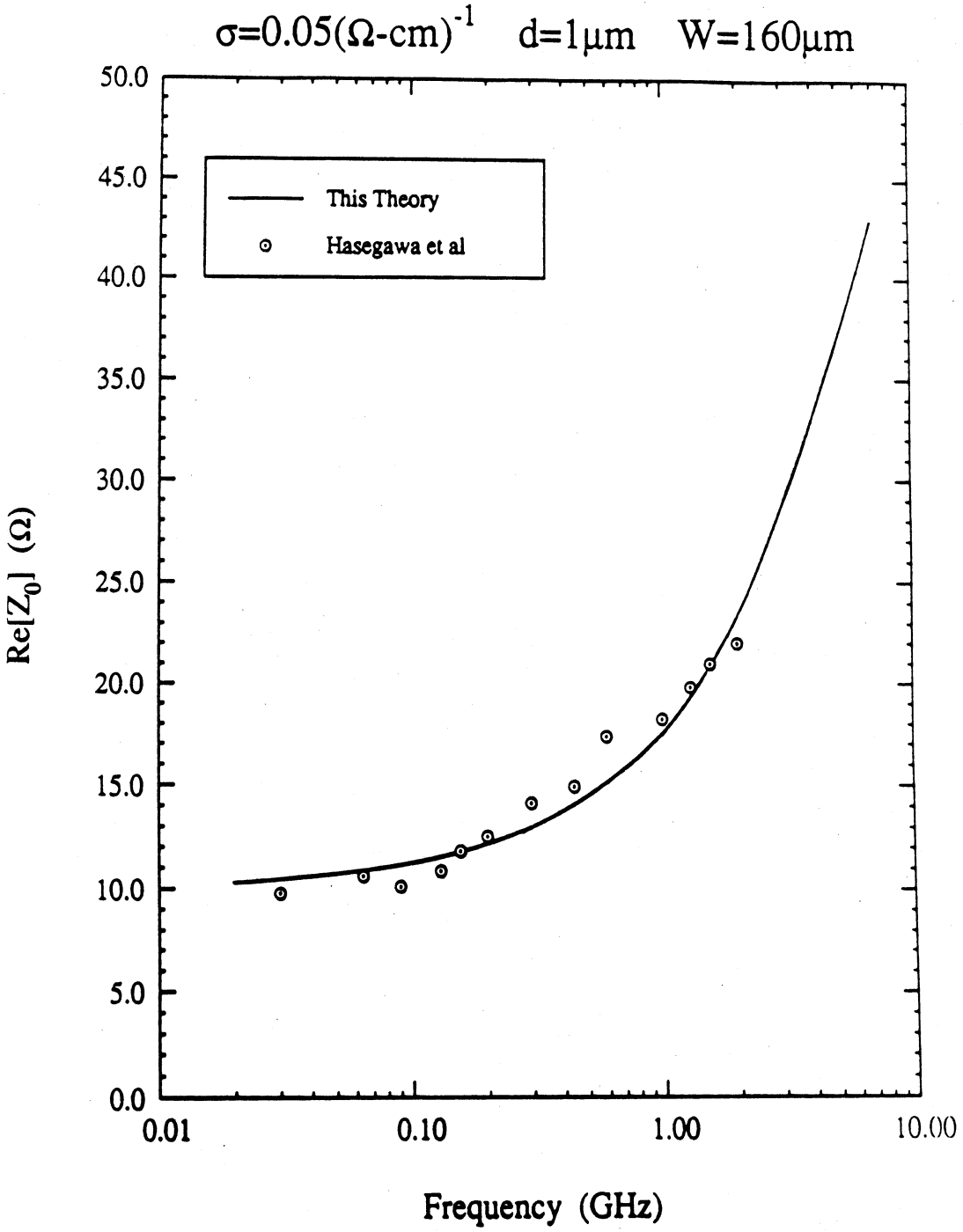
σ=0.05(Ω-cm)^-1 d=1μm W=160μm
This Theory
Hasegawa et al
Re[Z0] (Ω)
Frequency (GHz)
50.0
45.0
40.0
35.0
30.0
25.0
20.0
15.0
10.0
5.0
0.0
0.01
0.10
1.00
10.00

Figure 2

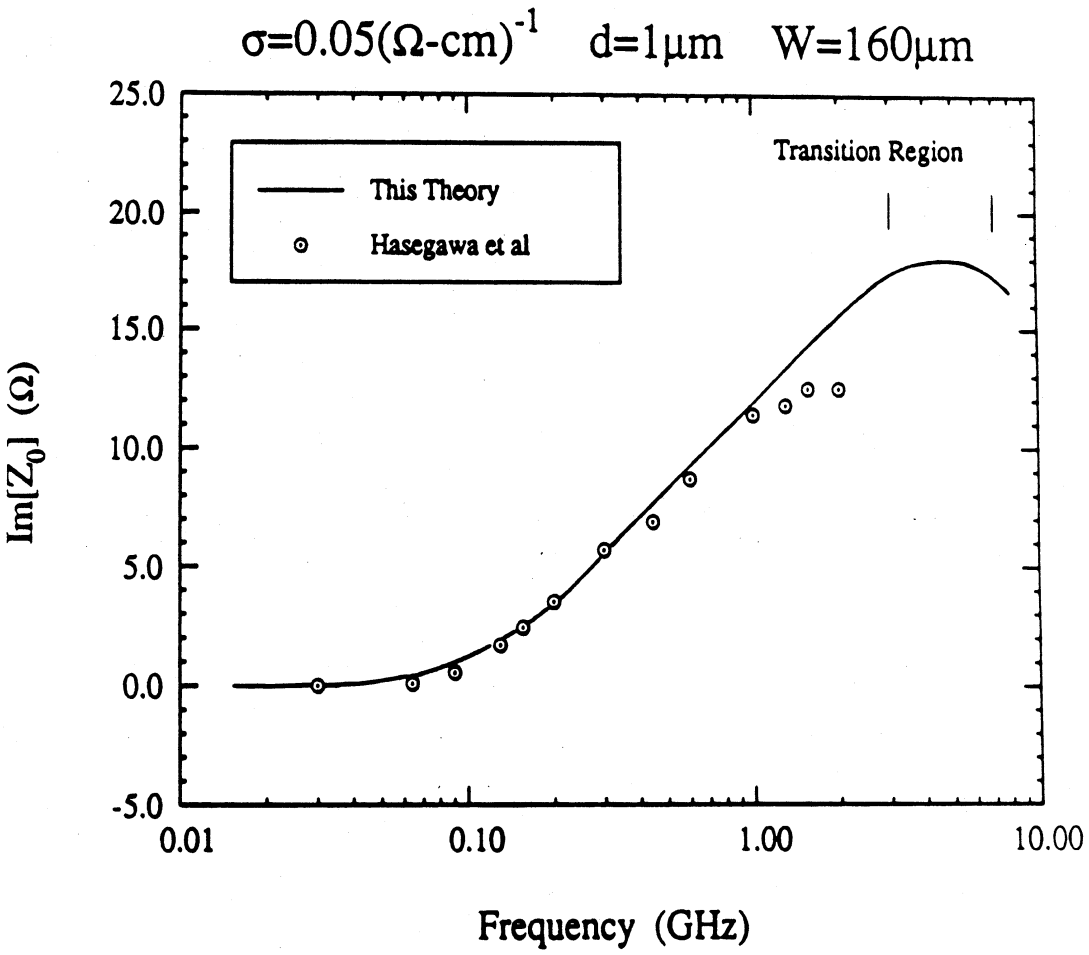
σ=0.05(Ω-cm)^-1 d=1μm W=160μm
Transition Region
This Theory
Hasegawa et al
Im[Z0] (Ω)
25.0
20.0
15.0
10.0
5.0
0.0
-5.0
0.01
0.10
1.00
10.00
Frequency (GHz)

Figure 3

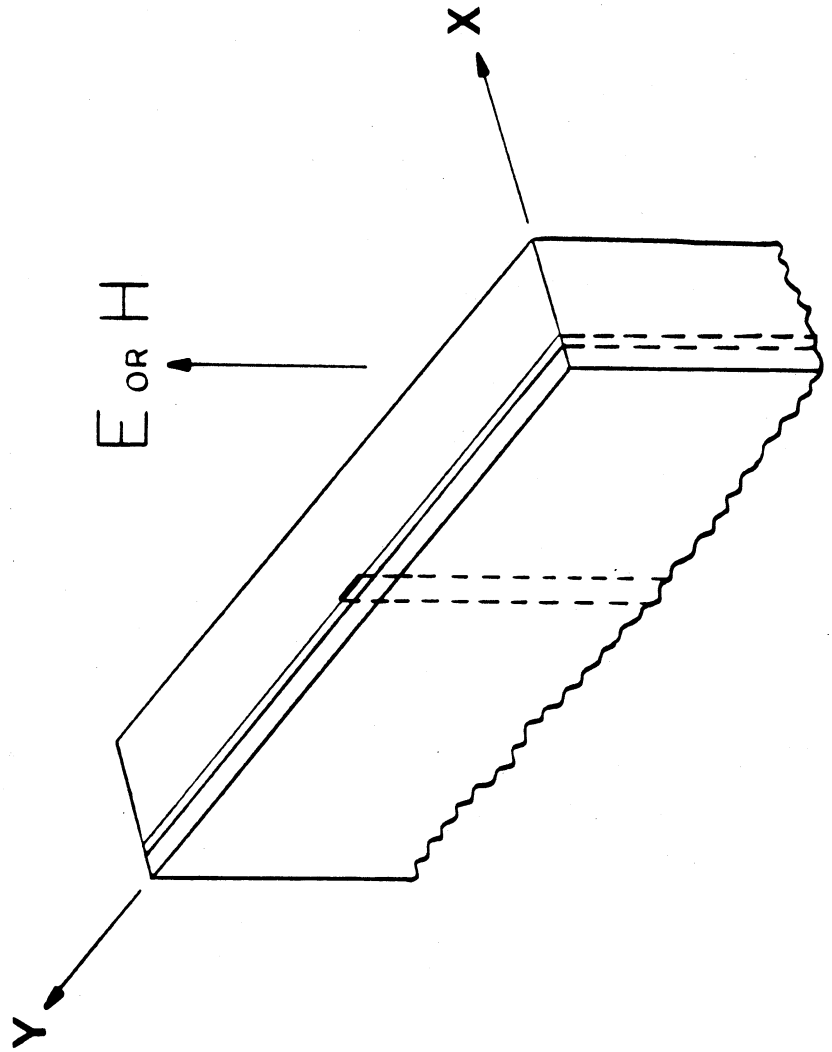

Figure 4

Figure 5

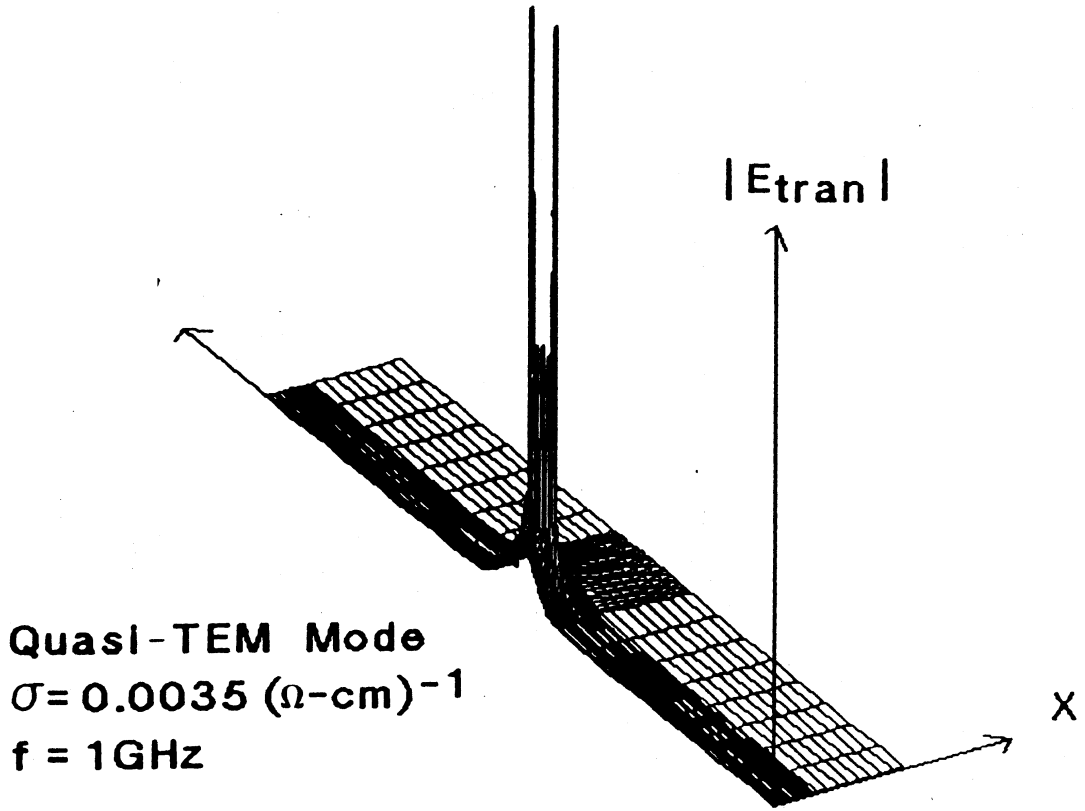

Figure 6

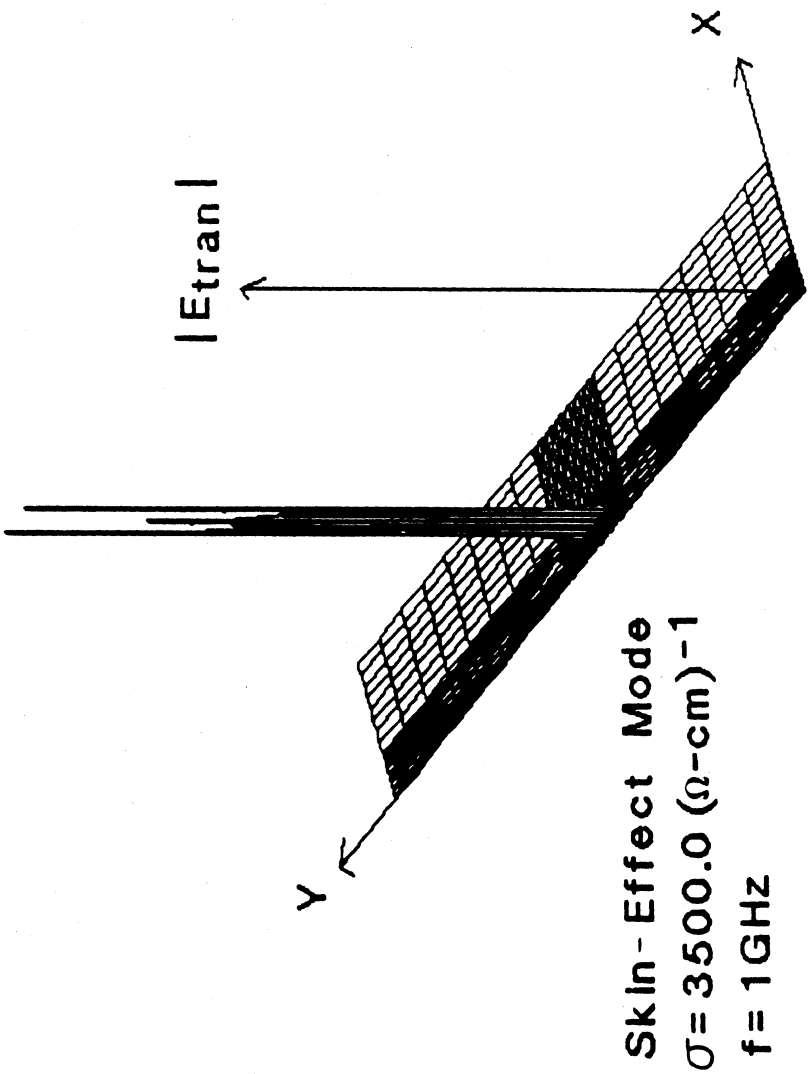

Figure 7

Figure 8.

Figure 9

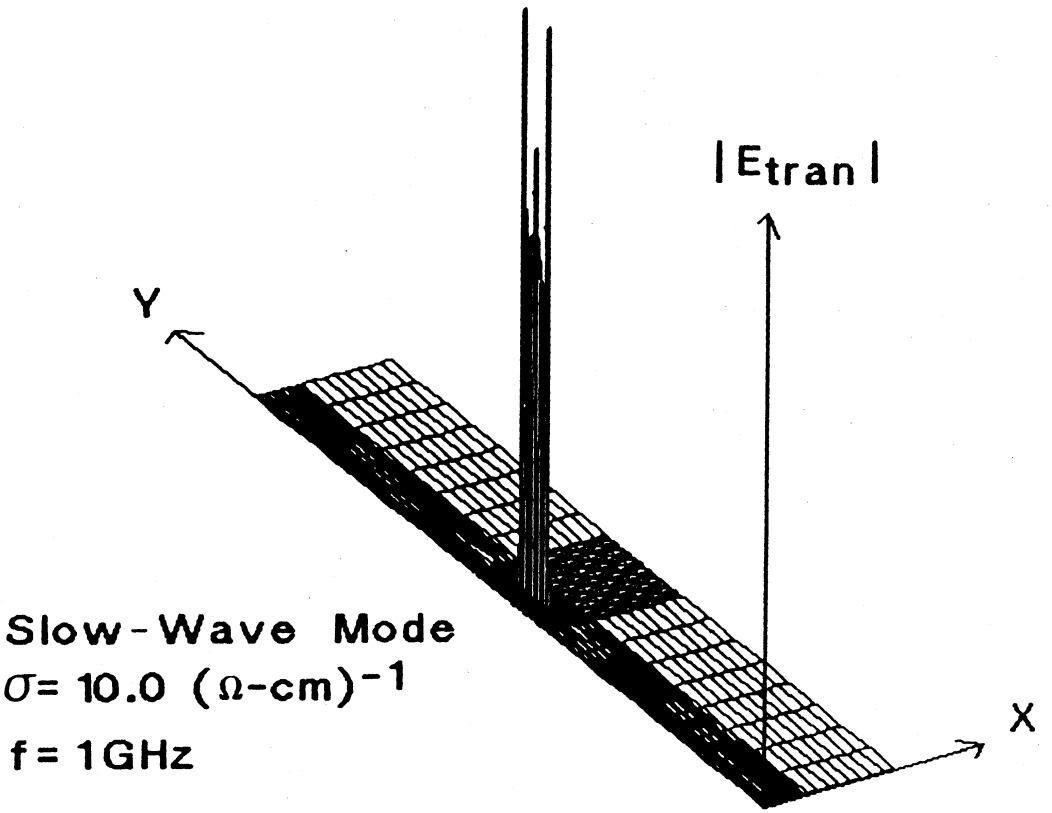

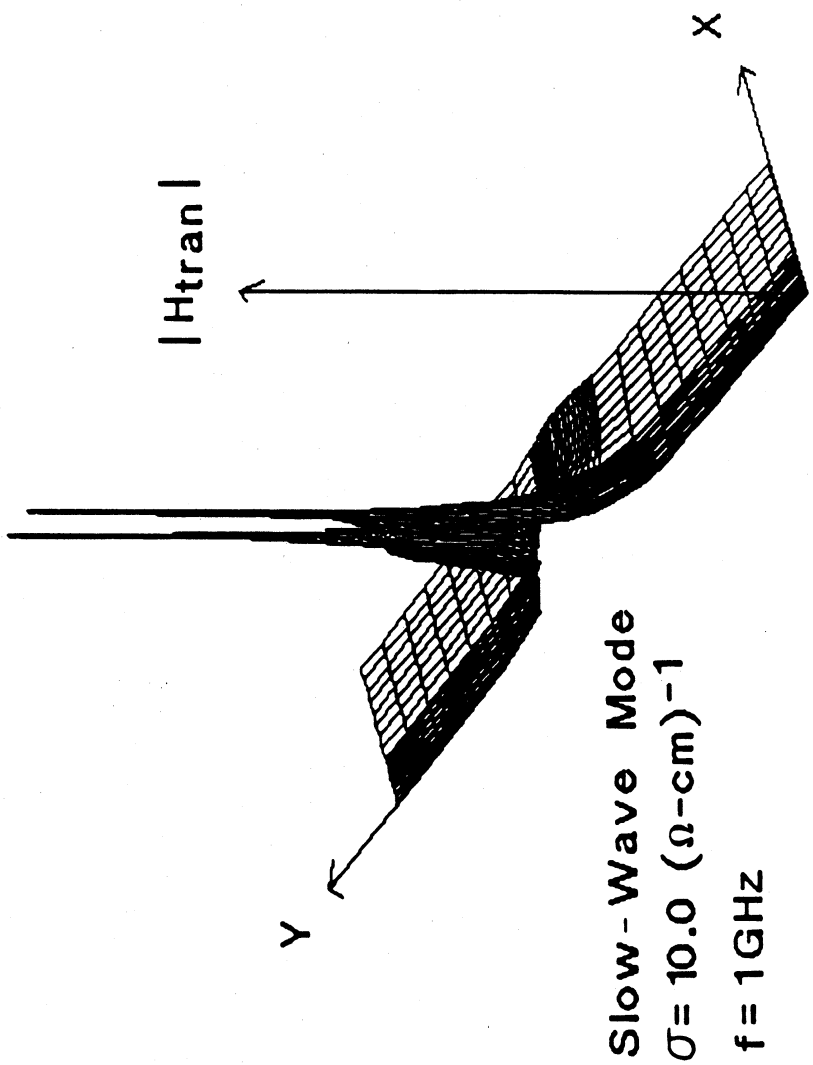

Figure 10

APPENDIX F

A Simple Method for Characterizing Planar Transmission Line Discontinuities on Dissipative Substrates

T.G. Livernois and P.B. Katehi

A SIMPLE METHOD FOR CHARACTERIZING PLANAR TRANSMISSION LINE DISCONTINUITIES ON DISSIPATIVE SUBSTRATES

Thomas G. Livernois and Pisti B. Katehi

Radiation Laboratory
Department of Electrical Engineering
and Computer Science
University of Michigan
1301 Beal Avenue
Ann Arbor, MI 48109-2122

ABSTRACT

A simple, least squares sum curve fitting technique is presented which accurately models surface currents on planar transmission lines. This approach is useful for characterizing discontinuities occurring in MIC's fabricated on dissipative substrates. Numerical results for the microstrip open-end on a lossy GaAs substrate are given.

INTRODUCTION

Costly design cycles which occur during the fabrication of microwave MIC's serve to illustrate the need for accurate characterization of passive planar transmission structures. In particular, microstrip discontinuities occurring in shielded substrate geometries have received a great deal of recent attention and several different full-wave methods have been proposed, [1,2,3,4,5]. In these works, the microstrip circuitry is located on either an assumed lossless or a low-loss substrate. Multi-function MIC's built on GaAs substrates, in general, contain regions with different conductivities, [6]. These regions cannot be considered low-loss in many cases. Consequently, the scattering behavior of microstrip discontinuities on dissipative substrates is of practical interest.

In this paper, a simple technique for characterizing microstrip discontinuities on lossy substrates is given. Numerical results (S_{11}) for the microstrip open-end on a GaAs substrate are given versus substrate thickness for various values of substrate conductivity and operating frequency.

THEORY

The geometry of a shielded microstrip open-end is shown in figure 1(a). The method presented here to characterize the microstrip open-end may be used in conjunction with any full wave method which yields the surface current distribution on the metallized region [1,4]. The space domain integral equation approach has been experimentally verified, [7], and is utilized in this paper. The present formulation is virtually identical to that in [1] except the Green's function is derived using the technique given in [8]. Other details pertaining to the method may be found in [1]. The current distribution on the microstrip line is obtained from the well-known relation:

$$[I] = [Z]^{-1} [V] \tag{1}$$

In the region on the strip between the discontinuity reference plane and the excitation point (say, a distance of $\lambda g/4$ from each) an ideal transmission line current exists as long as the operating frequency is below the cutoff frequency of the shielding structure. This is illustrated in figure 1(b). Note that this criteria is satisfied for all results given in this paper. When the dielectric substrate is considered lossless, the scattering parameters are obtained in a straight-forward manner using the constant SWR on the input line and lossless transmission line theory, [1]. However, when substrate losses are appreciable the SWR on the line is not a constant and the surface current is a complex quantity, no longer completely imaginary or completely real. In addition, the location of minima and maxima is difficult to determine, as is deciphering the propagation constant on the line. Therefore, the technique used on assumed lossless structures is impractical.

The uses of MIC's continue to extend to higher and higher frequencies where substrate losses cannot, in general, be neglected for passive structures. As a result, a new method for finding device scattering characteristics under these conditions is necessary.

Consider the region on the input line for the microstrip open-end shown in figure 1(b); higher order evanescent modes excited by the source and the discontinuity are negligible. In this vicinity, only the dominant microstrip mode propagates. The associated surface current may be written as that of an ideal transmission line:

$$J_z = J_z^+ e^{-jk_z\xi} + J_z^- e^{jk_z\xi}, \qquad (2)$$

where $\xi = z - \lambda_g/4$. Using a vector optimization method, the expression for current given by (2) may be curve fitted to the actual current distribution obtained from (1). This is accomplished by minimizing the square of the modulus of the sum of the differences between the actual current from (1) and the model current from (2) at several points along the ξ axis. In general, J_z^+, J_z^-, and k_z are complex quantities. Once these variables are determined, the input reflection coefficient of the port

can be computed. The normalized input impedance and generalized scattering parameters are then obtained in a straightforward manner, [1]. Although in this paper we give computed results for the microstrip open-end, a one-port structure, the method is applicable to multiport structures.

NUMERICAL RESULTS

The accuracy of the method described here was verified by comparison with results in [1,7] for the microstrip open-end on an assumed lossless alumina substrate. Excellent agreement was observed.

For the results given in this paper, a=b=2mm and W=100μm, and the discontinuity reference plane is at the physical end of the strip. The non-zero conductivity of the substrate is incorporated into a complex permittivity.

Computed values of the magnitude and phase of S_{11} for the microstrip open-end on a GaAs substrate are plotted versus substrate thickness, for various operating frequencies and conductivities, in Figures 2 and 3, respectively. The commercially available microwave CAD package, Touchstone [9], was used to generate results for S_{11} for comparison purposes. Regardless of substrate parameters σ and h or operating frequency, Touchstone predicts that $|S_{11}|=1$. Consequently, this result is not illustrated in Figure 2. Also, Touchstone yields results for the phase of S_{11} which depend only on the operating frequency and substrate height. Therefore, only one set of data is plotted for each frequency in Figure 3.

These results show that the magnitude of S_{11} is changed appreciably by changes in conductivity with substrate height and operating frequency held constant. On the other hand, the phase of S_{11} is virtually unaffected. The CAD package Touchstone does not account for the variation of $|S_{11}|$ but reasonably good agreement with this theory is observed for the phase of S_{11}.

The slight difference in the phase computations between this theory and Touchstone could be due to the fact that Touchstone does not include the effect of shielding structure side-walls.

CONCLUSION

A simple technique for characterizing planar transmission line discontinuities on dissipative substrates has been presented. Numerical results show that for the microstrip open-end with a fixed substrate thickness and operating frequency, the magnitude of S_{11} decreases while the phase of S_{11} changes very little with increasing substrate conductivity. These tendencies are not surprising, since under the above conditions the phase constant of J_z changes little and the attenuation constant increases.

ACKNOWLEDGEMENTS

The authors would like to thank Dr. John H. Bryant for his helpful suggestions during the preparation of this manuscript. This research was supported in part by the National Science Foundation under Grant ECS-8602530.

REFERENCES

[1] L.P. Dunleavy and P.B. Katehi, "A Generalized Method for Analyzing Shielded Thin Microstrip Discontinuities," IEEE Trans. Microwave Theory Tech., Vol. MTT-36, pp. 1758-1766, Dec. 1988.

[2] N.K. Uzunoglu, C.N. Capsalis, and C.P. Chronopoulos, "Frequency-Dependent Analysis of a Shielded Microstrip Step Discontinuity Using an Efficient Mode-Matching Technique," IEEE Trans. Microwave Theory Tech., Vol. MTT-36, pp. 976-984, June 1988.

[3] X. Zhang and K.K. Mei, "Time-Domain Finite Difference Approach to the Calculation of the Frequency-Dependent Characteristics of Microstrip Discontinuities," IEEE Trans. Microwave Theory Tech., Vol. MTT-36, pp. 1775-1787, Dec. 1988.

[4] J.J. Burke and R.W. Jackson, "Reduction of Parasitic Coupling in Packaged MMIC's," IEEE MTT-S Int. Microwave Symp. Dig., pp. 255-258, May 1990.

[5] R.H. Jansen and L. Weimer, "Full-Wave Theory Based Development of MM-Wave Circuit Models for Microstrip Open End, Gap, Step, Bend, and Tee," IEEE MTT-S Int. Microwave Symp. Dig., pp. 779-782, June 1989.

[6] GaAs Integrated Circuits: Design and Technology, Ed. Joseph Mun, Macmillan, New York, 1988.

[7] L.P. Dunleavy and P.B. Katehi, "Shielding Effects in Microstrip Discontinuities," IEEE Trans. Microwave Theory Tech., Vol. MTT-36, pp. 1767-1774, Dec. 1988.

[8] T.G. Livernois and P.B. Katehi, "A Generalized Method for Deriving the Space-Domain Green's Function in a Shielded, Multilayer Substrate Structure with Applications to MIS Slow-Wave Transmission Lines," IEEE Trans. Microwave Theory Tech., Vol. MTT-37, pp. 1761-1767, Nov. 1989.

[9] EEsof, Westlake Village, CA 91362-9904.

LIST OF FIGURES

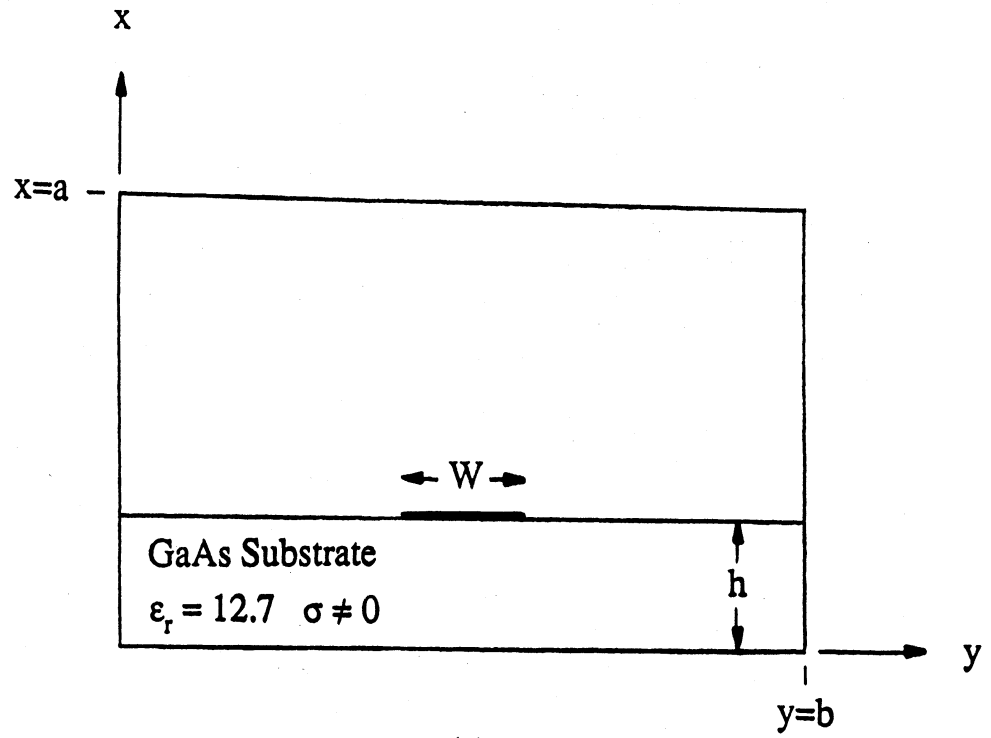
x
x=a
W
GaAs Substrate
$\varepsilon_r = 12.7 \quad \sigma \neq 0$
h
y
y=b

(a)

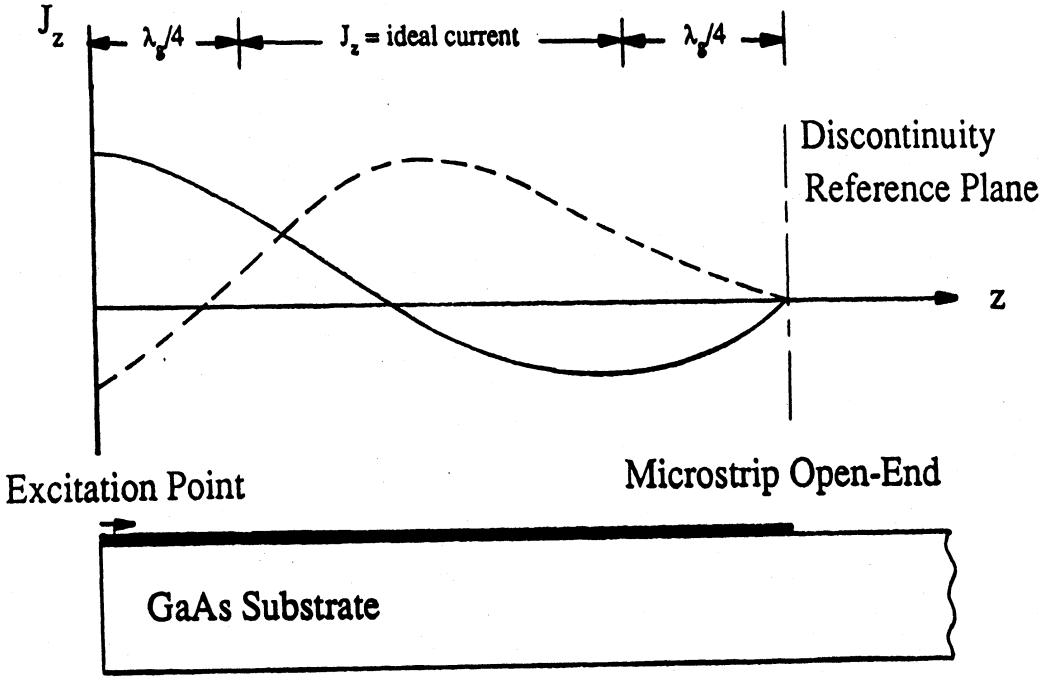
J_z
$\lambda_g/4$
J_z = ideal current
$\lambda_g/4$
Discontinuity
Reference Plane
z
Excitation Point
Microstrip Open-End
GaAs Substrate

(b)

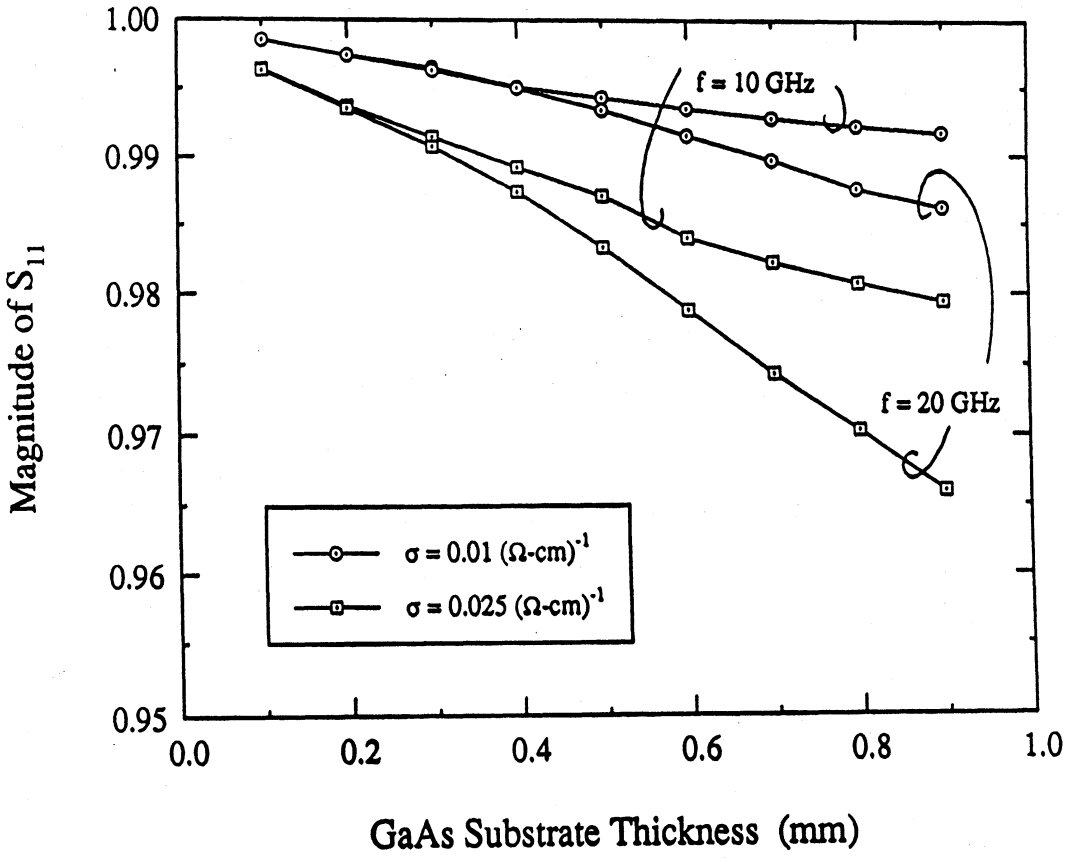
1.00
0.99
0.98
0.97
0.96
0.95
0.0
0.2
0.4
0.6
0.8
1.0
Magnitude of S_{11}
GaAs Substrate Thickness (mm)
f = 10 GHz
f = 20 GHz
σ = 0.01 (Ω-cm)$^{-1}$
σ = 0.025 (Ω-cm)$^{-1}$

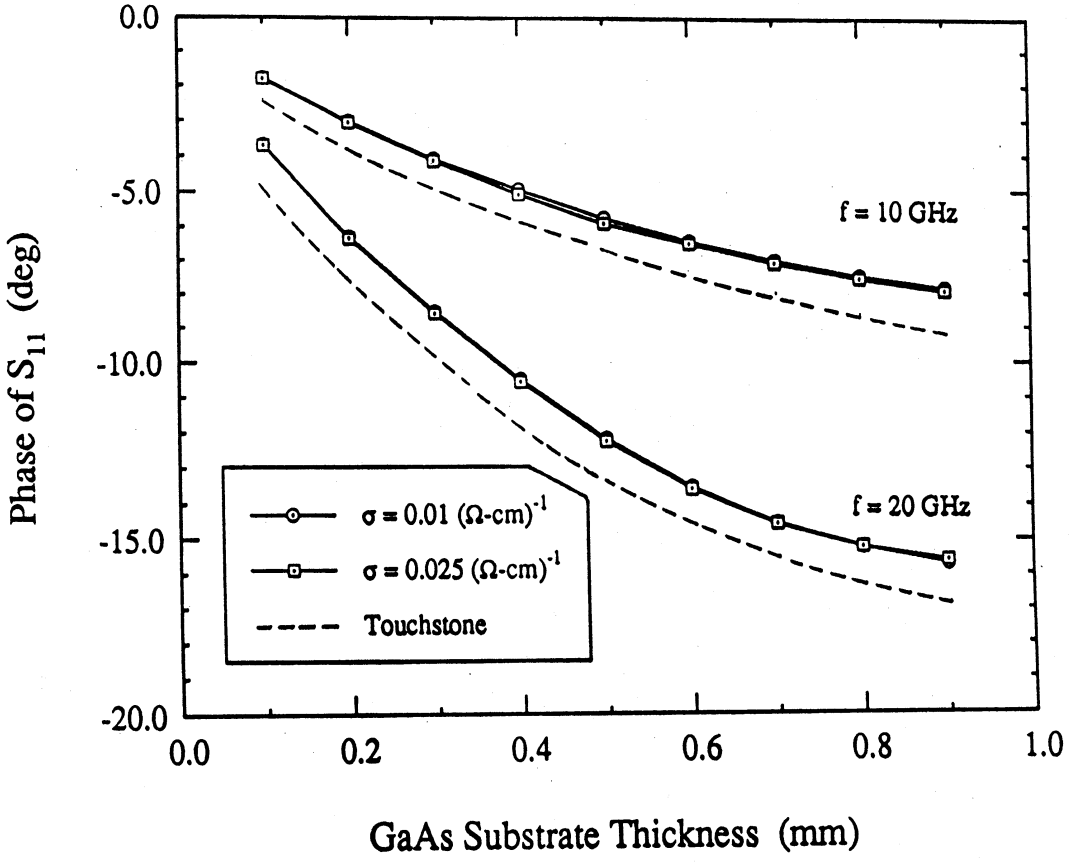
0.0
-5.0
-10.0
-15.0
-20.0
0.0
0.2
0.4
0.6
0.8
1.0
Phase of S_{11} (deg)
GaAs Substrate Thickness (mm)
f = 10 GHz
f = 20 GHz
σ = 0.01 (Ω-cm)$^{-1}$
σ = 0.025 (Ω-cm)$^{-1}$
Touchstone

APPENDIX G

An Accurate Characterization of Open Microstrip Discontinuities Including Radiation Losses

W. P. Harokopus and P. B. Katehi

AN ACCURATE CHARACTERIZATION OF OPEN MICROSTRIP DISCONTINUITIES INCLUDING RADIATION LOSSES

William P. Harokopus, Jr. and Pisti B. Katehi

The Radiation Laboratory
University of Michigan, Ann Arbor MI.

Abstract-An accurate full-wave analysis of a variety of open microstrip discontinuities and circuit elements has been performed. The technique has been employed to characterize microstrip corners, steps, and matching sections. A two-dimensional application of Method of Moments is utilized to solve Pocklington's Integral equation in the space domain. The analysis accurately accounts for dispersion, space wave, and surface wave radiation. Scattering parameters are obtained for the circuit element or discontinuity by using transmission line theory.

INTRODUCTION

The accurate characterization of passive microstrip elements and discontinuities is critical to the development of increasingly higher frequency MIC and MMIC circuits. Additionally, when microstrip circuits are combined with monolithic antenna elements, as in a phased array, the understanding of the electromagnetic interactions between circuit and antenna elements is crucial.

Previously, open microstrip discontinuities have been analyzed primarily by quasi-static methods [1], [2] or by equivalent waveguide models [3], [4]. Quasi-static techniques yield models with no frequency dependence, while equivalent waveguide models contain limited information on dispersion. Neither technique accounts for space and surface wave radiation, and they are therefore restricted to lower frequencies where these effects are not significant.

Consequently, the study of microstrip elements at higher frequencies requires a rigorous full electromagnetic analysis which accounts for radiation and all substrate effects. The full-wave analysis of open microstrip structures printed on a single layer has been performed by Katehi [5], and Jackson and Pozar [6]. However, the work performed assumed electrically thin elements, and was restricted to simple structures such as open-ends or gaps. The full-wave analysis presented here is a rigorous extension of [5] to more complex elements which form the building blocks to many multi-port microstrip networks. The following approach requires a solution to the integral equation relating the electromagnetic fields to the current on the microstrip. On the plane of the microstrip discontinuity, both current components are expanded into finite series.

Two dimensional Method of Moments and Galerkin's procedure are then utilized. This technique allows the characterization of a wide range of planar microstrip elements. In addition, the method is applicable to the study of antenna elements.

This formulation has been shown to accurately characterize microstrip corners, steps, stubs, and simple impedance matching sections. Numerical results are shown in this paper for typical two-port discontinuities, and a comparison is made to *Touchstone* [1].

ANALYSIS

The open microstrip geometry is shown in figure 1. Pocklington's integral equation relates the electric field to the current on the microstrip. Both directions of current (J_x, J_y) on the plane of the microstrip conductor are considered allowing the analysis of a wide range of planar microstrip elements. The electric field on the plane of the microstrip conductor $(z = 0)$ is

$$\begin{aligned} E_x(x,y,0) = \int_{s'}[\ & G_{xx}(x,y;x',y')\ \ j^x(x',y') \\ + \ & G_{xy}(x,y;x',y')\ \ j^y(x',y')]dx'dy' \end{aligned} \quad (1)$$

$$\begin{aligned} E_y(x,y,0) = \int_{s'}[\ & G_{yx}(x,y;x',y')\ \ j^x(x',y') \\ + \ & G_{yy}(x,y;x',y')\ \ j^y(x',y')]dx'dy' \end{aligned}$$

where the expressions $G_{ij}(x,y;x',y')$ are components of the dyadic green's function for a Hertzian dipole above a grounded dielectric substrate [7],[8].

Two-dimensional Method of Moments is utilized. The two unknown current components are expanded into finite series of unknown amplitudes multiplied by known basis functions. The basis functions chosen are rooftop functions which allow for sinusoidal variation in the longitudinal direction and for constant variation in the transverse direction according to

$$J_x = \sum_{n=1}^{N+1}\sum_{m=1}^{M+1} I^x_{nm} j^x_{nm}(x',y') \quad (2)$$

$$J_y = \sum_{n=1}^{N+1}\sum_{m=1}^{M+1} I^y_{nm} j^y_{nm}(x',y') \quad (3)$$

[1] *Touchstone* is a microwave CAD software package available from EESOF

$$j^x_{n,m}(x',y') = [f_n(x')g_m(y')] \quad (4)$$

$$j^y_{n,m}(x',y') = [g_n(x')f_m(y')] \quad (5)$$

with

$$f_n(x') = \begin{cases} \frac{\sin k(x_{n+1}-x')}{\sin kl_x} & x_n \le x' \le x_{n+1} \\ \frac{\sin k(x'-x_{n-1})}{\sin kl_x} & x_{n-1} \le x' \le x_n \end{cases} \quad (6)$$

and

$$g_m(y') = \begin{cases} 1 & y_{m-1} \le y' \le y_{m+1} \end{cases} \quad (7)$$

In equations (6) and (7) $l_x = x_{n+1} - x_n$, and k is a parameter which is equal to the wavenumber in the dielectric.

These series are substituted into Pocklington's Integral equation (1), and Galerkin's method is applied to enforce the boundary condition on the microstrip conducting strip. The inner products

$$\langle E_x, j^x(x,y) \rangle \quad (8)$$

$$\langle E_y, j^y(x,y) \rangle \quad (9)$$

which represent the weighted average of the electric field on the surface of the conducting strip are set to zero. The resulting system of linear equations can be written in matrix form as

$$\begin{bmatrix} Z_{XX} & Z_{XY} \\ Z_{YX} & Z_{YY} \end{bmatrix} \begin{bmatrix} I_x \\ I_y \end{bmatrix} = \begin{bmatrix} V_x \\ V_y \end{bmatrix} \quad (10)$$

where $Z_{ij}(i = x,y : j = x,y)$ represent blocks of the impedance matrix, I_i is the vector of unknown x and y current amplitudes, and V_j is the excitation vector which is identically zero everywhere except at the position of the source. After the matrix inversion is performed, the current amplitudes on the feeding lines are known. If only the fundamental microstrip mode is present, the current forms a uniform standing wave. For the case of a two-port discontinuity, the even and odd excitation technique is employed to determine the 2-port scattering parameters through transmission line theory.

RESULTS AND DISCUSSION

To accurately calculate scattering parameters, the current must form a uniform standing wave pattern away from the discontinuity being measured. At and near the discontinuity, power is launched into space and surface waves, and higher order microstrip modes are present. Additionally, at high frequencies (or more specifically electrically thick substrates) higher order modes have been observed on the microstrip line away from the discontinuity. The presence of these higher order modes complicates the analysis. Nevertheless, for practical applications it is desirable to choose dimensions and dielectric permittivity so that only the fundamental microstrip mode propagates away from the discontinuity. In this case, the scattering parameters are easily computed from the current standing wave patterns.

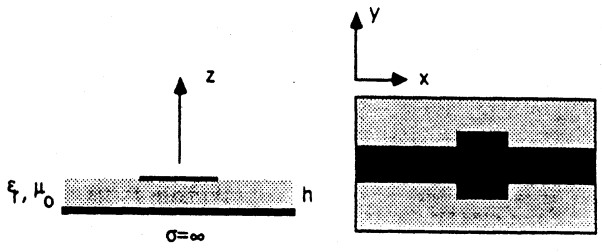

Figure 1: Open Microstrip Geometry

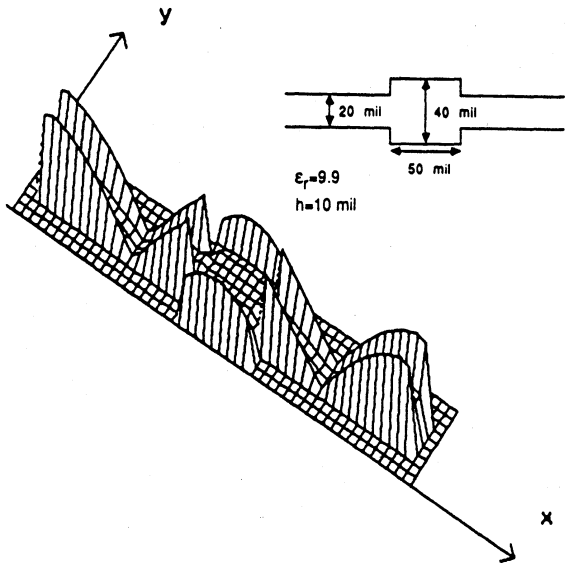

Figure 2: Longitudinal Current On Matching Section

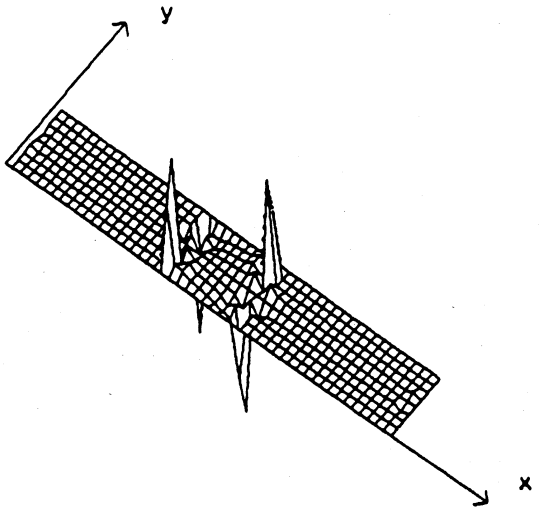

Figure 3: Transverse Current On Matching Section

For an impedance matching section on a 10 mil substrate of permittivity 9.9, the longitudinal and transverse current components are shown in Figures 2, and 3 for the even excitation case. As illustrated, the current forms a uniform standing wave pattern on the feeding lines of the discontinuity. The scattering parameters are easily determined and are compared to *Touchstone* with good agreement (Figure 4).

In Figure 5 the scattering parameters for a microstrip corner on a 20 mil substrate with a dielectric permittivity of 9.9 are shown to be in excellent agreement with *Touchstone* from 6-14 GHz (*Touchstone* model is valid to 14 GHz).

The final numerical example clearly shows the effect of space and surface wave losses on circuit performance. The two-port scattering parameters for an open ended tuning stub are examined. The stub has a quarter wave resonance at 41 GHz. The phase of the scattering parameters for the microstrip tuning stub are in good agreement with *Touchstone* (Figure 6). Nonetheless, the radiation and surface wave losses are quite large and become a dominate effect over this frequency range. Figure 7 shows the radiated power as a function of frequency.

Beyond 30 GHz, the radiated power increases sharply. The radiation losses can also be seen in the failure of our S_{11} to reach 1 (0 DB) as the *Touchstone* simulation does at the stubs resonance. The loss is due to space waves and the TM_0 surface wave. The TM_0 surface wave has a zero cutoff frequency in open microstrip.

Such an example shows that the accurate characterization of space and surface wave radiation losses is critical to MMIC design. In addition, other microstrip elements will be presented [9] which demonstrate radiation and substrate effects.

CONCLUSIONS

An accurate fullwave analysis of a variety of open microstrip discontinuities has been presented. Numerical results for the technique have demonstrated good agreement with the commercially available microwave software package *Touchstone* at lower frequencies. The presented technique accounts fully for radiation losses and all substrate effects, thus facilitating the development of more accurate high frequency circuit models.

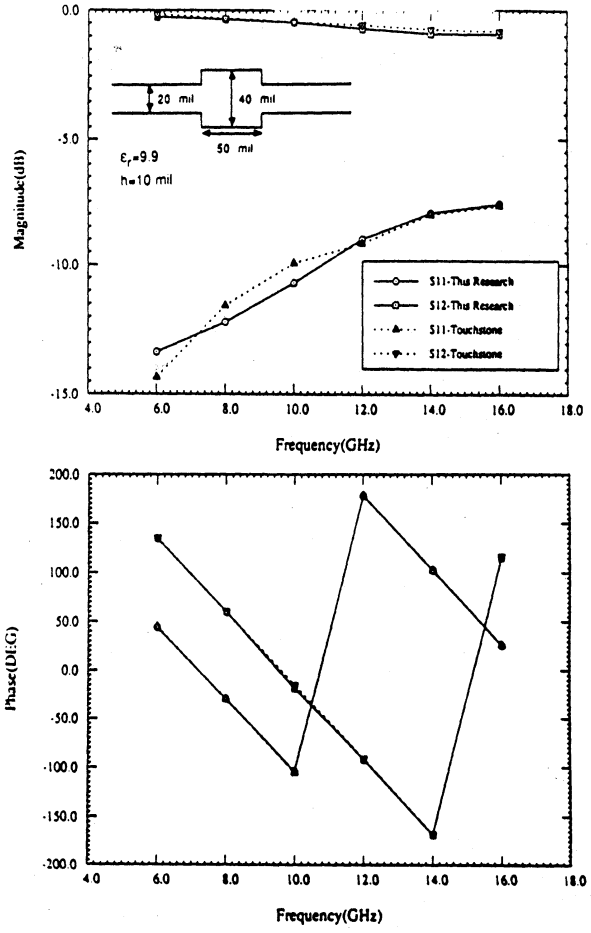

Figure 4: Scattering Parameters of Matching Section

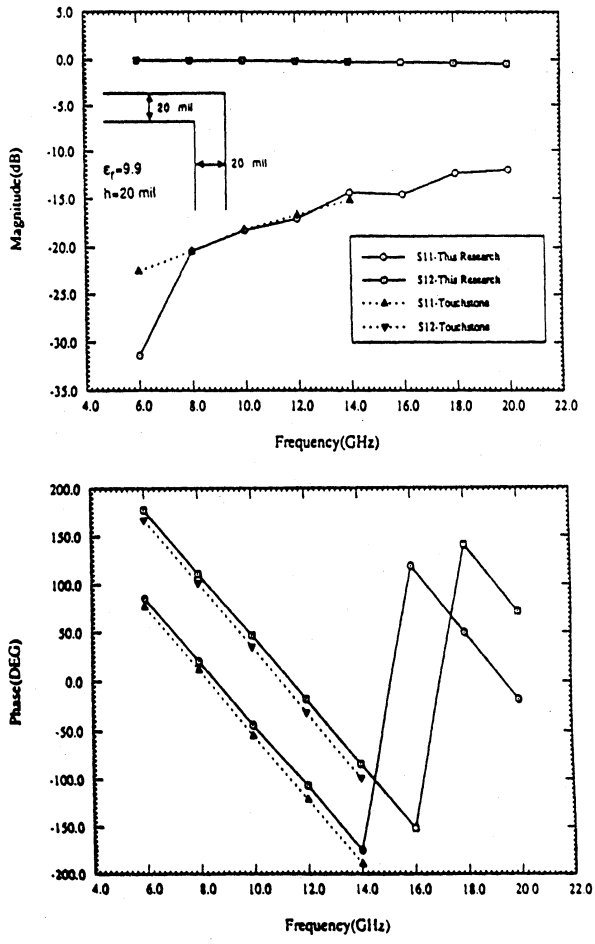

Figure 5: Scattering Parameters of Microstrip Corner

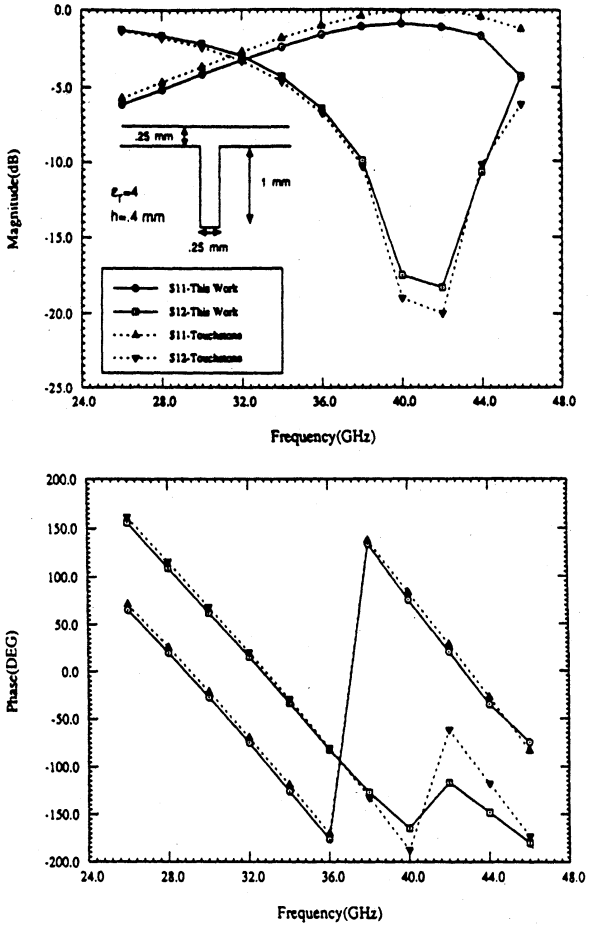

Figure 6: Scattering Parameters of Microstrip Stub

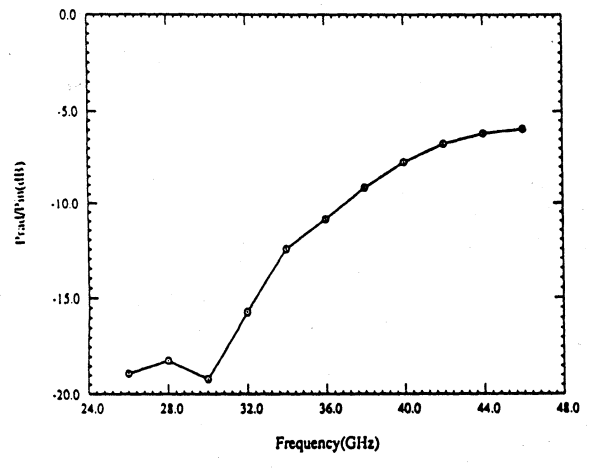

Figure 7: Power Radiated by Microstrip Stub

Acknowledgements

The authors wish to thank Mr. S. R. Nelson and Mr. Alan Crane of Texas Instruments for their contributions to this work. The research was sponsored by the National Science Foundation (Contract No. ECS-8602536).

References

[1] M. Maeda, "Analysis of Gap in Microstrip Transmission Lines", *IEEE Trans. Microwave Theory Tech.*, Vol. MTT-20, 1972.

[2] P. Benedek and P. Silvester, "Equivalent Capacitance of Microstrip Gaps and Steps", *IEEE Trans. Microwave Theory Tech.*, Vol. MTT-20, 1972.

[3] T. Itoh, "Analysis of Microstrip resonators", *IEEE Trans. Microwave Theory Tech.*, Vol. MTT-22, 1974.

[4] I. Wolf, G. Kompa, and R. Mehran, "Calculation Method For Microstrip Discontinuities and T-Junctions," *Electron. Lett.*, Vol. 8, 1972.

[5] P.B. Katehi and N. G. Alexopoulos, "Frequency-Dependent Characteristics of Microstrip Discontinuities in Millimeter-Wave Integrated Circuits",*IEEE Trans. Microwave Theory Tech.*, Vol. MTT-33, No. 10, pp. 1029-1035.

[6] R. W. Jackson, and D. M. Pozar, "Full-Wave Analysis of Microstrip Open-End and Gap Discontinuities",*IEEE Trans. Microwave Theory Tech.*, Vol. MTT-33, No. 10, pp. 1036-1042.

[7] A. Sommerfeld, Partial Differential Equations in Physics, New York, N.Y., Academic Press,1949.

[8] R.S. Elliott, "The Green's Function For Electric Dipoles Parallel To and Above or Within a Grounded Dielectric Slab", Hughes Technical Correspondence, 1978.

[9] W.P. Harokopus, Jr. and P. B. Katehi, "High Frequency Characterization of Open Microstrip Discontinuities on Multilayer Substrates," Submitted for publication to *IEEE Trans. Microwave Theory Tech.*.

[10] R.F. Harrington, Field Computation By Moment Methods, Macmillan,N.Y. ,1968.

APPENDIX H

Radiation Properties of Open Microstrip Discontinuities

W. P. Harokopus and P. B. Katehi

RADIATION PROPERTIES OF OPEN MICROSTRIP DISCONTINUITIES

William P. Harokopus, Jr.*
Pisti B. Katehi
Center for Space Terahertz Technology
University of Michigan
Ann Arbor MI 48109

Abstract

The radiation properties of a variety of open microstrip discontinuities have been studied. The full electromagnetic analysis performed has been shown to accurately characterize microstrip corners, steps and matching sections. The technique employed solves Pocklington's integral equation for the unknown current distribution of the conducting sections by an application of method of moments in the space domain. The radiated field is evaluated using a steepest descent method. The analysis accurately accounts for all substrate effects.

Introduction

The accurate characterization of passive microstrip elements is critical for the application of these elements in monolithic antenna arrays. Of particular importance is the radiation properties of these elements. Previously, open microstrip discontinuities have been analyzed primarily by quasi-static methods [1], [2] or by equivalent waveguide models [3], [4]. Quasi-static techniques yield models based on low frequency characteristics, while equivalent waveguide models contain limited information on dispersion. Neither technique accounts for space and surface wave radiation, and are therefore restricted to lower frequencies where these effects are not significant.

In addition, rigorous full electromagnetic solutions which include radiation and all substrate effects have been performed by P. B. Katehi [5], and Jackson [6]. Also, Yang [7] performed a full wave analysis for a substrate-superstrate configuration. However, the work performed assumed electrically thin elements, and was restricted to simple structures such as open-ends or gaps. The approach presented in this paper, based on the previous analysis of the author, allows the modeling of more complex planar elements such as steps, corners, and T-junctions [8].

The presented technique employs method of moments to generate a system of linear equations from Pocklington's integral equation. The system is inverted to find the current on the microstrip section. On the plane of the microstrip.

1989 IEEE AP-S International Symposium, Vol. III, pp. 1703-1704.

both current components are included. From the current, the far-fields may be obtained both in and above the substrate.

Analysis

The open microstrip geometry is shown in figure 1. Maxwell's equations combined with Green's vector identities result in Pocklington's integral equation which relates the electric field to the current on the microstrip. Both directions of current $(j^x(x',y'), j^y(x',y'))$ on the plane of the microstrip conductor are considered to allow for the analysis of a wide range of planar elements. The electric field on the plane of the microstrip conductor $(z = 0)$ is

$$E_x(x,y,0) = \int_{s'}[G_{xx}(x,y;x',y')j^x(x',y') + G_{xy}(x,y;x',y')j^y(x',y')]dx'dy'$$
$$E_y(x,y,0) = \int_{s'}[G_{yx}(x,y;x',y')j^x(x',y') + G_{yy}(x,y;x',y')j^y(x',y')]dx'dy' \quad (1)$$

Where $G_{xx}(x,y;x',y'), G_{xy}(x,y;x',y'), G_{yx}(x,y;x',y'), G_{yy}(x,y;x',y')$ are components of the dyadic green's function for a Hertzian dipole above a grounded dielectric substrate [9],[10].

The two components of the unknown current are expanded into finite series of unknown current amplitudes multiplied by known basis functions.

$$J_x = \sum_{n=1}^{N+1}\sum_{n=1}^{M+1} I^x_{nm} j^x_{nm}(x',y') \quad (2)$$

$$J_y = \sum_{n=1}^{N+1}\sum_{n=1}^{M+1} I^y_{nm} j^y_{nm}(x',y') \quad (3)$$

In the above, the sub-domain basis functions $(j^x_{nm}(x',y')\ j^y_{nm}(x',y'))$ are chosen to have sinusoidal variation in the longitudinal direction and constant variation in the transverse direction.

These series are substituted into Pocklington's Integral equation (1), and Galerkin's method is applied to enforce the boundary condition on the microstrip conducting strip. The resulting system of linear equations can be written in matrix form as

$$\begin{bmatrix} Z_{XX} & Z_{XY} \\ Z_{YX} & Z_{YY} \end{bmatrix} \begin{bmatrix} I_x \\ I_y \end{bmatrix} = \begin{bmatrix} V_x \\ V_y \end{bmatrix} \quad (4)$$

where $Z_{ij}(i = x,y : j = x,y)$ represent blocks of the impedance matrix, I_i is the vector of unknown x and y current amplitudes, and V_j is the excitation vector which is identically zero everywhere except at the position of the source. The matrix inversion is performed to determine the current on the structure.

The scattering parameters are obtained by transmission line theory, and the total power radiated into space and surface waves is given by

$$1 - |S11|^2 - |S12|^2 \quad (5)$$

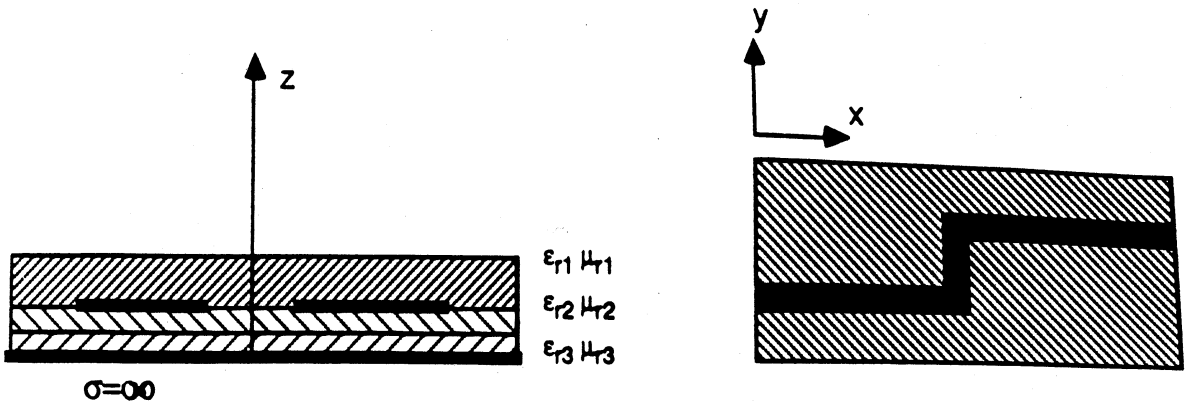

Figure 1: Open Microstrip Geometry

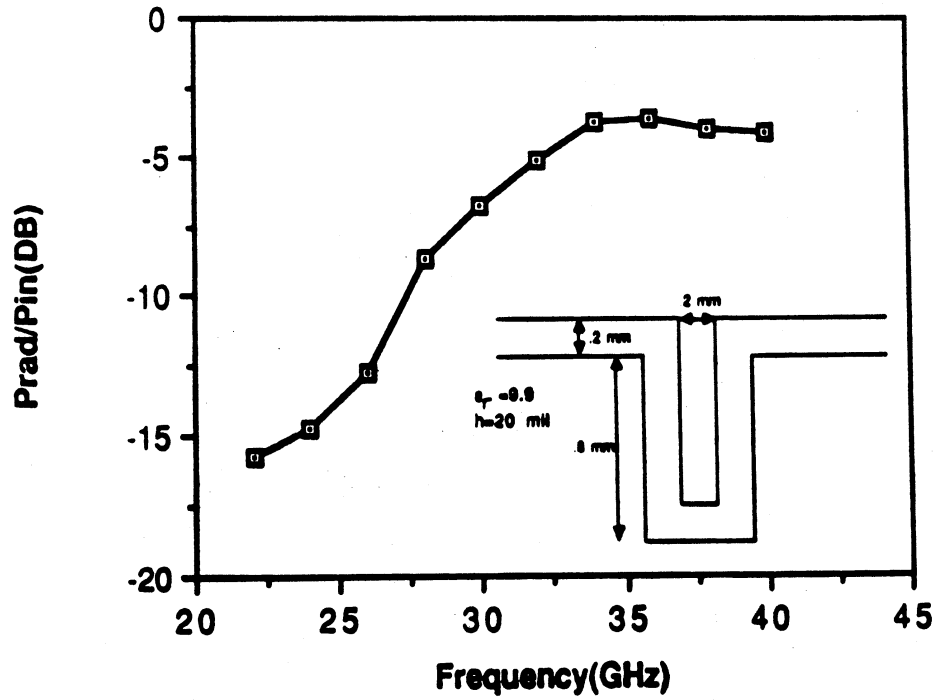

Figure 2: Power Radiated by Meander Inductor

Once the microstrip current is known, the radiated far-fields may be obtained through an asymptotic evaluation of the integrals in the equation for the electric field [11]. The Green's function is mapped to the steepest descent plane and the contour is deformed along the steepest descent path. The Green's function contains analytic functions in its denominator whose zeroes correspond to surface wave modes. During the contour deformation, these poles are captured and contribute to the far-field in the dielectric.

The presented technique was used to characterize a single loop meander inductor. The radiated power over a wide frequency range is shown in figure 2. As shown, the radiated power above 30 GHz is quite significant. This example illustrates the need to account for radiation in the design of microstrip networks.

Acknowledgement

This research was sponsored by the National Science Foundation (Contract No. ECS-8602536).

References

[1] M. Maeda, "Analysis of Gap in Microstrip Transmission Lines", *IEEE Trans. Microwave Theory Tech.*, Vol. MTT-20, 1972.

[2] P. Benedek and P. Silvester, "Equivalent Capacitance of Microstrip Gaps and Steps", *IEEE Trans. Microwave Theory Tech.*, Vol. MTT-20, 1972.

[3] T. Itoh, "Analysis of Microstrip resonators", *IEEE Trans. Microwave Theory Tech.*, Vol. MTT-22, 1974.

[4] I. Wolf, G. Kompa, and R. Mehran, "Calculation Method For Microstrip Discontinuities and T-Junctions," *Electron. Lett.*, Vol. 8, 1972.

[5] P.B. Katehi and N. G. Alexopoulos, "Frequency-Dependent Characteristics of Microstrip Discontinuities in Millimeter-Wave Integrated Circuits",*IEEE Trans. Microwave Theory Tech.*, Vol. MTT-33, Oct. 1985.

[6] R. W. Jackson, and D. M. Pozar, "Full-Wave Analysis of Microstrip Open-End and Gap Discontinuities",*IEEE Trans. Microwave Theory Tech.*, Vol. MTT-33, Oct. 1985.

[7] H. Yang, N. G. Alexopoulos, and D. R. Jackson, "Analysis of Microstrip Open-End and Gap Discontinuities in a Substrate-Superstrate Configuration," *IEEE MTT-S Microwave Symposium Digest*, 1988.

[8] W. P. Harokopus, Jr. and P. B. Katehi, "An Accurate Characterization of Open Microstrip Discontinuities Including Radiation Losses", Submitted for publication to *IEEE Trans. Microwave Theory Tech.*.

[9] A. Sommerfeld, Partial Differential Equations in Physics, New York, N.Y., Academic Press,1949.

[10] R.S. Elliott, "The Green's Function For Electric Dipoles Parallel To and Above or Within a Grounded Dielectric Slab", Hughes Technical Correspondence, 1978.

[11] L.B. Felsen and N. Marcuvitz, Radiation and Scattering of Waves,Prentice Hall, Englewood Cliffs, N.J. 1973.

APPENDIX I

Analysis and Design of Slow-Wave Structures Using an Integral Equation Approach

T. G. Livernois and P. B. Katehi

ANALYSIS AND DESIGN OF SLOW-WAVE STRUCTURES USING AN INTEGRAL EQUATION APPROACH

Thomas G. Livernois and Pisti B. Katehi

Electrical Engineering and Computer Science Department,
The University of Michigan, Ann Arbor, MI 48109-2122

ABSTRACT

An integral equation formulation which yields dispersion characteristics for planar transmission lines on layered, lossy substrates is presented. Galerkin's procedure in the space domain is used and roots of the resulting characteristic equation provide the desired phase and attenuation constants. Numerical results are compared to those found in the literature for the MIS slow-wave structure.

1. INTRODUCTION

MIS structures have been studied by several researchers and are used widely in related MIC's. The slowing effect can be applied to many devices such as: i) delay lines, ii) phase shifters, iii) tunable filters, and iv) others. The early work of Hasegawa et al [1], provided useful physical insight to the electromagnetic characteristics of the MIS microstrip transmission line, as do several subsequent articles, [2] - [7]. Unfortunately, some of this work is restricted to relatively low frequencies, thus, it is not useful for designing state-of-the-art monolithic MIC's. The remaining methods, namely, Finite-Element Analysis (FEA) and Spectral Domain Analysis (SDA), are somewhat cumbersome to work with. Consequently, accurate design criteria are difficult to obtain. This paper outlines a rigorous method for characterizing shielded, layered, planar transmission lines. The presented approach, even if based on an integral equation method, results in relatively simple design equations which can be programmed very efficiently in a personal computer. Dispersion characteristics found by this technique for the MIS microstrip transmission line are compared to published theoretical and experimental results.

II. THEORY

Every planar structure is characterized by a coupled set of equations which relate the Green's function for the metallic waveguide (Figure 1) to the microstrip currents carried by the perfectly conducting strip. This set can be put into the following form:

$$\begin{bmatrix} G_{yy} & G_{zy} \\ G_{yz} & G_{zz} \end{bmatrix} * \begin{bmatrix} J_y \\ J_z \end{bmatrix} = \begin{bmatrix} E_y \\ E_z \end{bmatrix}$$

In this approach, the four components of the matrix are expressed in terms of LSM and LSE waves generated by the appropriate infinitesimal electric currents, [8]. The expansions for J_y and J_z are chosen to satisfy their respective edge conditions. The primary advantage of this technique

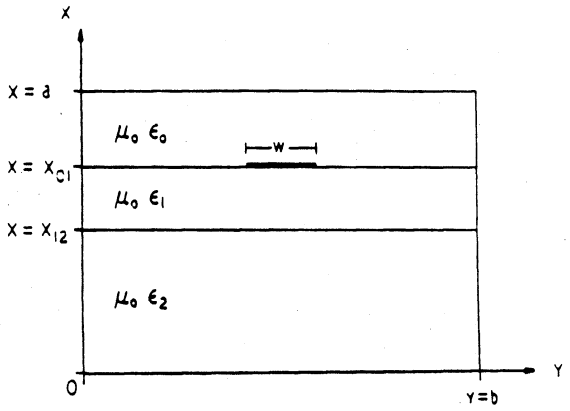

Fig. 1. Geometry of MIS slow-wave structure. (a = 1.5mm, b = 10.0mm, x_{01} = 0.251mm, x_{12} = 0.250mm)

results from the orthogonality of LSM and LSE modes. When solving for amplitude coefficients of the generating vector potentials, the boundary conditions on all tangential fields are invoked. This results in an apparent inhomogeneous 4x4 system of equations. However, this system decouples into two 2x2 sets of equations which relate LSM and LSE amplitude coefficients separately. The convolution integrals resulting from (1) are evaluated in closed form. Using one expansion term for J_y and J_z and applying the Galerkin's procedure to (1) shows:

$$\begin{bmatrix} \sum_{m=1,\,\text{odd}}^{M} P_{1m} & \sum_{m=1,\,\text{odd}}^{M} Q_{1m} \\ \sum_{m=1,\,\text{odd}}^{M} S_{1m} & \sum_{m=1,\,\text{odd}}^{M} U_{1m} \end{bmatrix} \begin{bmatrix} c_1 \\ d_1 \end{bmatrix} = \begin{bmatrix} 0 \\ 0 \end{bmatrix} \tag{2}$$

where c_1 is the unknown amplitude coefficient for the first expansion term of J_y and d_1 similarly results from J_z. In equation (2) the expressions for P_{1m}, Q_{1m}, S_{1m} and U_{1m} are rather simple combinations of Bessel and Trigonometric functions, and are given in [9]. Setting the determinant of the current amplitude matrix to zero and solving for its roots yields the complex microstrip propagation constant $k_z = \beta - j\alpha$.

III. NUMERICAL RESULTS

The dispersion characteristics given in this section are for the MIS structure with dimensions given in figure 1. Two different microstrip widths are considered. Region 2 is the lossy Si substrate with $\varepsilon_{r2} = 12$ and region 1 is the SiO_2 insulating region with $\varepsilon_{r1} = 4$. The effects of the induced conduction current are incorporated into a complex permittivity in region 2. The normalized wavelength and attenuation constant for different cases are plotted in figures 2 - 5. Good convergence was obtained using one expansion term for the microstrip current and M = 501 in the four truncated series in (2). Roots of the matrix were found using Mueller's method with deflation.

Good agreement between this theory, FEA, SDA, and experiment for λ/λ_o and α is found when W = 160μ. This data is shown in figures 2 and 3.

Results for the wider strip, given in figures 4 and 5 with W = 600μm, show discrepancies between this theory and the spectral domain approach for larger substrate conductivities. For the case σ = 1000 and f = 1 GHz the spectral analysis finds a very low normalized wavelength of about 0.04. This value is unacceptable considering that the Si substrate is five skin depths thick. As a result, the electromagnetic fields are virtually shielded from the semiconducting layer. This drives the line into the skin effect and not the slow wave mode. Results derived by the method presented in this paper indicate such a tendency. Curves generated from the parallel plate analysis (applicable to wide microstrip), [1], are also plotted in Figures 4 and 5 and are in agreement with our theoretical data. Figures 4, 5 also show experimental results plotted for various cases. Good quantitative agreement was found for smaller substrate conductivities while qualitative tendencies are observed for larger substrate conductivities.

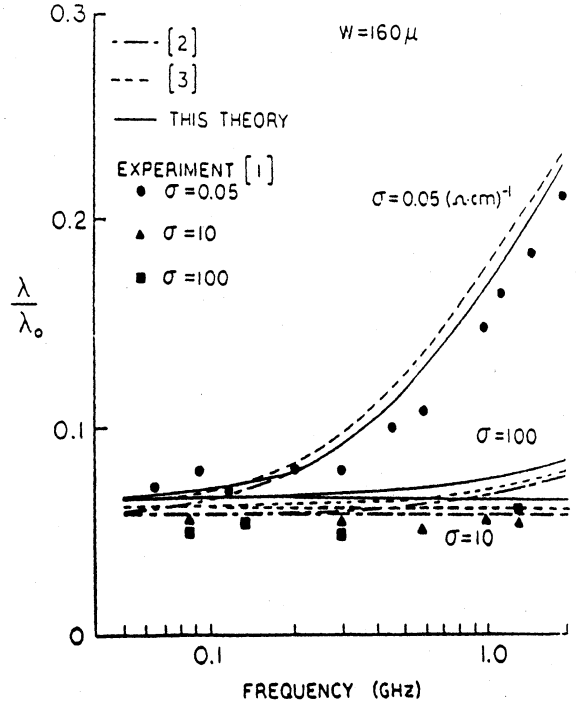

Fig. 2. Comparison of normalized wavelength with SDA [2], finite element [3], and experimental results [1], for W = 160μ

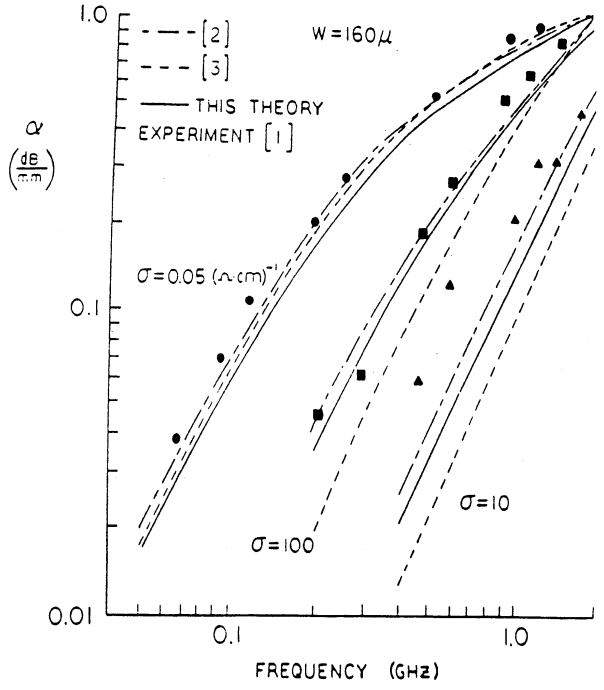

Fig. 3. Comparison of attenuation constant with SDA [2], finite element [3], and experimental results [1], for W = 160μ.

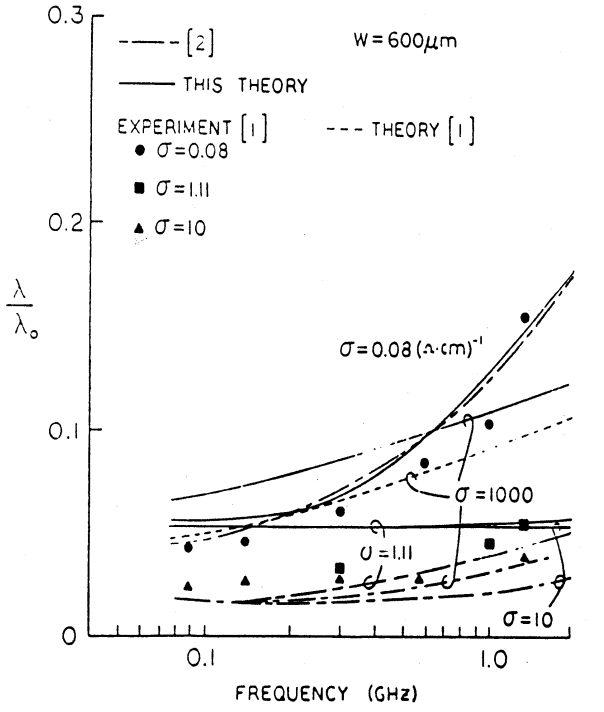

Fig. 4. Comparison of normalized wavelength with SDA [2] and experimental and parallel plate model results [1], for w = 600μ.

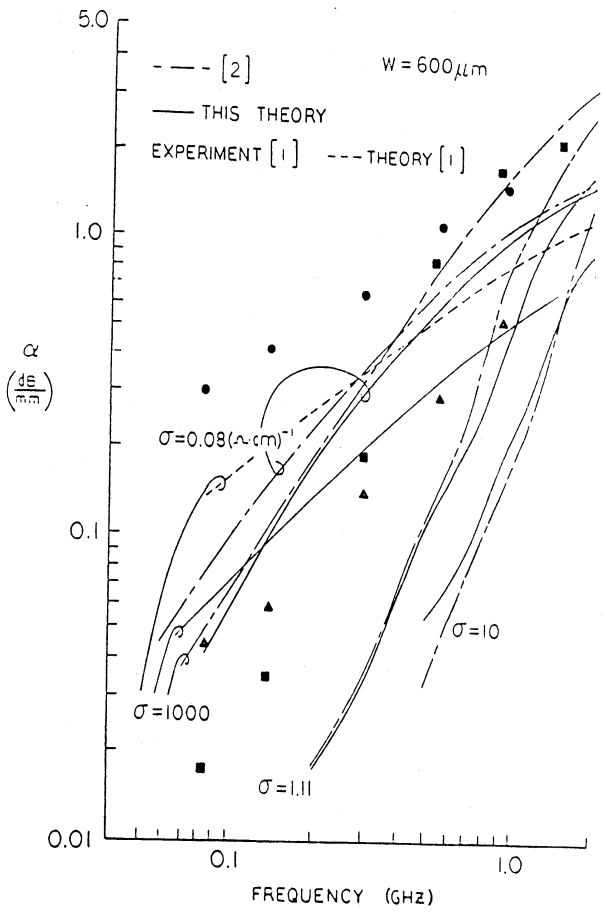

Fig. 5. Comparison of attenuation constant with SDA [2] and experimental and parallel plate model results [1], for w = 600μ.

IV. CONCLUSION

An efficient, accurate method useful for characterizing layered, planar transmission lines has been presented in this paper. Numerical results were compared to other published work.

This method has been proved very accurate and efficient for studying lines on insulator-semiconductor substrates. The technique is based on an integral equation formulation and results in design equations which can be simply programmed on a personal computer. The validity of the numerical results was verified by comparing to available theoretical and experimental data.

V. ACKNOWLEDGEMENTS

This work has been sponsored by the National Science Foundation under the contract ECS-8602530.

REFERENCES

1. H. Hasegawa, M. Furukawa, H. Yanai: "Properties of Microstrip Line on Si-SiO_2 System" IEEE Trans. Microwave Theory and Techniques, vol. MTT-19 No. 11, November 1971, pp. 869-881.

2. P. Kennis and L. Faucon, "Rigorous Analysis of Planar MIS Transmission Lines," *Electron. Lett.*, vol. 17, no. 13, pp. 454-456, June 1981.

3. M. Aubourg, J. Villotte, F. Godon and Y. Garault, "Finite Element Analysis of Lossy Waveguides - Applications to Microstrip Lines on Semiconductor Substrate," IEEE Trans., MTT-31, No. 4, pp.326-330, April 1983.

4. D. Jager, "Slow Wave Propagation Along Variable Schottky Contact Line," IEEE Trans., *Microwave Theory Tech.*, vol. MTT-24, pp. 566-573, Sept. 1976.

5. Y.C. Shih and T. Itoh, "Analysis of Printed Transmission Lines for Monolithic Integrated Circuits," *Electron. Lett.*, vol. 18, No. 14, pp. 585-586, July 1982.

6. C. Tzuang and T. Itoh, "Finite-Element Analysis of Slow-Wave Schottky Contact Printed Lines," IEEE Trans., MTT-34, No. 12, pp. 1483-1489, December 1986.

7. C. Krowne, "Slow-Wave Propagation in Generalized Cylindrical Waveguides Loaded with a Semiconductor," *Int. J. Electronics.*, vol. 58, No. 2, pp. 249-269, 1985.

8. R. Harrington, "Time Harmonic Electromagnetic Fields," New York: McGraw-Hill, 1961.

9. T.G. Livernois and P.B. Katehi, "A Generalized Method for Deriving the Space-Domain Green's Function in a Shielded, Multilayer Substrate Structure with Applications to MIS Slow-Wave Transmission Lines," Submitted to IEEE Trans. on Microwave Theory and Techniques.